Residence Time Investigation of Artificial Silver Ores in Heap Leaching Using Cyanide Lixiviant

By

Borbor A.K.K. Gibson

A thesis submitted at the University of Cape Town in fulfilment of the requirements for the degree of

Master of Science in Engineering

Department of Chemical Engineering

University of Cape Town

January 2020

University of Cape Town

The copyright of this thesis vests in the author. No quotation from it or information derived from it is to be published without full acknowledgement of the source. The thesis is to be used for private study or non-commercial research purposes only.

Published by the University of Cape Town (UCT) in terms of the non-exclusive license granted to UCT by the author.

University of Cape Town

Abstract

Heap Leaching has gained much relevance in the processing of low-grade mineral resources - ores considered uneconomical for beneficiation through conventional concentration and tank leaching. However, it is at the same time characterized by extended leaching periods due to slow mineral conversion and low rates of recovery as a major challenge.

Interactions within the heap bed are not fully understood as chemical leaching and hydrodynamics interact in a complex manner. To study these interactions, a number of investigations have focused on the hydrodynamic interaction using conventional residence time distribution (RTD) studies in laboratory columns. In these RTD studies, the flows of tracer exiting through the effluent stream provide information of its paths, where some flows might relate to fast movement, slow convoluted channels, or micro/macro stagnated regions. This information is usually interpreted through simplified reactor models representing the bed as a combination of plug flow reactors (PFRs), continuous stirred tank reactors (CSTRs) and dead zones.

Using columns as reactors to approximate heap leaching on a laboratory scale, it is anticipated that the RTD flow distribution response should be similar to the distribution of a PFR with associated dead zones. While some literature sources have alluded to the response in columns being similar to a plug flow response, recent sources using a similar hydrodynamic RTD approach reported column reactor distribution resembling flow more typical of a continuous stirred tank, CSTR, system instead of plug flow. Given that packed ore beds are not agitated, this appears paradoxical. It is hypothesised that the CSTR-like response is a result of the distribution of convoluted flow channels through the ore bed, which perform overall like a bundle of PFRs of different lengths. To discern the two patterns the use of a reactive leaching on a well-characterized ore material is proposed.

Therefore, this work aims to study simultaneously the flow and leach performance of a laboratory column reactor, utilizing a novel reactive leaching approach with a lixiviant amendable to a well-characterized homogeneous solid material. The objective of this work is to establish flow distribution performance in packed bed columns and correlate such performance to the ultimate extraction from the packed bed.

The study was performed using a nonreactive solution tracer (potassium nitrate) to characterise flow through a column packed with an artificial silver 'ore' (silver grains embedded in concrete), followed by a reactive leaching study using sodium cyanide which would leach the silver. The artificial silver ore was developed with the aim to exhibit four ideal properties, namely homogeneous porosity, uniform grain size, homogenous dispersion of the grains throughout the ore, and even grade distribution of the different size fractions after crushing.

Leaching and micro-XCT characterization studies were performed in order to determine the leaching properties of the artificial silver ore and validate the ore corresponds to these ideal properties. This validation was indeed achieved; however, the inner-particle pores were not found to be continuous at the scale of resolution of the instrument (4.8 microns). Poor extraction from the coarse particles in both the leaching characterization and reactive column leaching investigations suggested that this network was not well established and may exist only at the sub-micron scale.

Leach tests were performed on individual particle sizes in both shake flask and circulating bed reactor tests. Extraction from the leaching of the coarse synthetic silver ore particles was observed to be very low relative to dissolution from pure silver metal grains. Diagnostic shrinking core and the extended mixed topology models were used to determine the controlling dissolution mechanism. Both models demonstrated that a diffusion-reaction mechanism governed the dissolution extraction from the large particles.

RTD column leaching studies were performed utilizing flow rate and PSD as investigated parameters. The nonreactive tracer produced a step-change flow response that was more similar to a characteristic plug flow type distribution but showed distinct deviations towards CSTR behavior, especially for the beds containing a higher degree of fines.

Reactive column leaching experiments were performed under similar conditions as the nonreactive RTD, introducing a step-change of the cyanide reagent. Rapid silver leaching occurred initially, but equally rapidly declined to very low rates. The leach curves were interpreted by translating the information obtained from the nonreactive RTDs into a distribution of parallel plug flow channels. The extent of reaction for each of these channels is derived from the surface reaction model for the individual size classes, put together for the corresponding PSD in each experiment. RTD specific PSDs tested using this approach assumed that longer residence times correspond to the prevalence of finer material.

The validity of the approach was tested by comparing the extraction determined from the particle leaching kinetics studies to the reactive column data through modelling. The model is based on the weighted average leaching from a population of particles, calibrated against kinetic models formulated for individual size classes. This model is further linked to a distribution of flow channels determined from the RTD studies.

The prediction of the model did not compare too well against the raw silver dissolution data of the columns. This was attributed to the model having been calibrated against kinetic data that did not fully consider the smaller size classes below -4/+2.8 mm – considered to be the key source of rapid surface reaction in the packed bed. Although the concept proposed in this project was not fully proven, further test work is recommended to expand on the approach presented here.

Declaration

I, Borbor Auzzel Kwaku Kudar Gibson, hereby declare that this thesis is my own work. It is being submitted for the degree of Master of Science in Engineering in the University of Cape Town. This thesis has not been submitted before for any degree or examination in any other university.

Signed by candidate

28th day of January 2020

Acknowledgements

"Wait on the LORD: be of good courage, and he shall strengthen thine heart: wait, I say, on the LORD."

Psalms 27:14

I thank the LORD, God Almighty, for His wonderful works and blessings granted me successfully through this journey. It has only been faith and trust in Him couple with work that has made me attain such an achievement. My all is, have been, and will ever be in Him for His love towards me. Thank you LORD.

Sincere thanks and appreciation go to my supervisor, Prof. Jochen Petersen, for his willingness to accept me as his student, patience, guidance, directives, encouragements, and constructive criticisms throughout this project. His expertise is unequivocal and relationship with his students is admirable. I am grateful to have been your student.

I would like to appreciate Dr. Glen Nwaila for his assistance and suggestions during the micro-XCT characterization and leach setup of this project. The Necsa Radiography and Tomography (RADTOM) group (Dr. Frikkie de Beer, Dr. Lunga Bam, and Jakobus Hoffman) are thanked for their invaluable resourceful service afforded during the micro-focus X-ray scanning and analysis segment of this project. Dr. Molahlehi Sonopo is thanked for availing his organic lab during the setup and run of the leaching experiments at Necsa.

I would like to thank A/Prof. Megan Becker for her expertise during the interpretation of the micro-XCT data and for offering an extension to the study with QEMSCAN characterisation. A special thank you goes to Lorraine Nkemba and Keshree Pillay for QEMSCAN sample preparation and data analysis respectively. I express my gratitude to Shireen Govender, Kenneth Maseko, and Monde Bekaphi of the Centre for Mineral Research who provided support for all crushing, screening, and other ore preparation techniques carry out in this project. Heartfelt thanks go to the Concrete and Structural Engineering lab team (Nooredien Hassen, Tahir Mukaddam, Charles May and Chris), Civil Engineering Department, UCT, for their support and assistance during the ore production for the preliminary investigation of this project. I would also like to extend a thank you to Raeesah Gani and Archippe Manzila, P52 project students (2018), who took on the preliminary characterization studies and set the stage for this project.

The UCT Chemical Engineering Department Analytical Laboratory team (Sandeeran Govender, Russell Geland, Sibongile Nyimbinya, Shene Klink, and Zulfa Le Riche) and Charney Anderson-Small of the Stellenbosch University Central Analytical Facilities are thanked for the analysis of my samples.

It was a pleasure to share postgraduate studies in the Hydrometallurgy research group. To my colleagues, all your constructive criticisms, questions, suggestions, and recommendations during seminars provided the

fine-tuning to the structure of this thesis. You all (Luis Beiza, Patrick Prestele, Dasmi Maharaj, Archippe Manzila, Kathija Shaik, Chad Naude, De Waal Hugo, Jordy Dinga, Nicole Uys, Sfiso Mkhize, Cledwyn Mangunda, Aysha Lotter, Blessing Chirume, Senzo Mgabhi, Natasha Davids) are wonderful people who made my space in Hydromet memorable. Special thanks go to Dr. Mehdi Safari and Dr. Thandazile Moyo who provided their space and time to clarify vague ideas; always providing the critical analysis that shaped my thinking and approach to this project. Dr. Alexey Cherkaev is thanked for his insightful contributions to the RTD studies and PFR-P model interpretation.

A very big thank you goes to the University of Liberia for the funding of this project. This was realized through the instrumentation of Prof. Ophelia Weeks, who interest has always been in the capacity development of her staffs. I am gratified for your unwavering confidence in my ability. I would like to thank A/Prof. Saeed C. Chelgani for being a mentor and friend, who discovered a potential in me and has never stop encouraging me to do more.

Finally, I am extremely grateful to my parents, Pastor Borbor D. Gibson & Mrs. Carman M. Gibson, and brother, J. Laygbemah Gibson I, for their tireless prayers, guidance, and all levels of support and encouragements during this journey. I would have never made it without them. God be praised.

"I waited patiently for the LORD; and He inclined unto me, and heard my cry."

Psalm 40:1

Table of Contents

List of Figures

List of Tables

Glossary of Terms

2D	Two Dimensional Space
3D	Three Dimensional Space
Ag	Silver
AS	Agglomerated Size
BDC	Blending Distribution Coefficient
CF-FBR	Circulating Fluidized Fixed Bed Reactor
CSTR	Continuous Stirred Tank Reactor
CT	Computed Tomography
GGS	Gates-Gaudin-Schumann
GSD	Grain Size Distribution
GVA	Grey Value Analyser
ICP-MS	Inductively Coupled Plasma Mass Spectrometry
ICP-OES	Inductively Coupled Plasma optical emission spectrometry
MSE	Mean Squared Error
OOS	Optimum Operating Size
PET	Positron Emission Tomography
PFR	Plug Flow Reactor
PLS	Pregnant Leach Solution
PMA	Particle Mineral Analysis
PSD	Particle Size Distribution
PVE	Partial Volume Effect
QEMSCAN	Quantitative Evaluation of Minerals by Scanning Electron Microscopy
ROI	Region of Interest
ROM	Run-of-Mine Ore
RTD	Residence Time Distribution
SCM	Shrinking Core Mode
SF	Shake Flask
SHE	Safety, Health, & Environment
SSM	Shrinking Sphere Model
WAM	Water Absorption Measurement
wt %	Weight Percentage
XCT	X-ray Computed Tomography

1 INTRODUCTION

1.1 Background

Heap leaching has proven to be a technology ideal for the process recovery of metals from low-grade ores. The beneficiation process involves irrigating a bed of stacked ore particles at the top and recovering the drained solution from the bottom of the bed through drainage systems. These recovered solutions contain concentrated dissolved metals that have been extracted and transported into the exiting bulk solution, pregnant leach solution (PLS). Precious metals are recovered from the PLS in subsequent stages including carbon adsorption, solvent extraction and electro-winning (SX/EW; *Ghorbani et al., 2016*). Heap leaching technology is characterized to represent flow operation in columns that are of ideal approximation to plug flow mechanism (*Dixon & Hendrix, 1993*); it consists of solution transport through multi-flow channels and stagnant regions in packed beds. The flow of irrigated solution through heap beds is transient, hence it is an unsaturated operation (*de Andrade Lima, 2006; Govender-Opitz et al., 2017*). The path of fluid movement interacting in the bed is neither preferential nor is it uniform; liquid flow is considered to be apportioned into stagnant liquid held in pores and liquid phase flowing through larger particles channels (*Bouffard & Dixon, 2001; Govender-Opitz et al., 2017*).

The mechanism of operation in heap leaching involves reactants fed to the column, solution travelling through bed interstices forming metal complexes in solution (in gold/silver application), exchanging across phase boundaries, diffusing through water-filled pores, and exiting the reactor as partially or completely stable soluble converted products (*Bouffard & Dixon, 2001; Robertson, 2017*). During the lixiviant application to the bed or column reactor, indifferent flow mechanisms including short-circuited flow (by-pass), flow experiencing significant interaction within the bed (well-mixed), or fluid captured in stagnant or dead regions through the bed are most likely to occur. These flow patterns to some extent contribute to the localized metal extraction through micro-channels in each bed particle. Determination of these flow mechanisms is achieved utilizing residence time distribution (RTD) investigation in packed bed systems.

Traditionally, residence time investigation is a technique to elucidate the metallurgical leaching response and hydrodynamic behaviour of fluid flow in different reactor systems (*Bouffard & West-Sells, 2009*). Residence time studies provide insight of flow by identifying molecules (the use of tracers) in reactors and relating the distribution of time as flowing solution navigates the reactor.

In investigations utilizing laboratory columns to mimic actual heap operation, it is expected that fluid flow distribution throughout the reactor should produce typical plug flow type performance. A number of RTD investigations have indicated RTD output performances of column leaching to produce non-ideal plug flow

behaviour. However, recent RTD studies investigating solute transport in packed beds have shown to experience flow type output identical to a continuous stirred tank reactor (CSTR) system.

In fact, there are two things to consider prior to understanding the paradoxical situation of both flow performances. Firstly, continuously stirred tank reactors and plug flow reactors (PFR) are two types of reactors that have a distinct mechanism of operation; hence, their inherent residence time distribution performance. Secondly, solid-liquid interaction in a CSTR system is well mixed, while no mixing occurs in a PFR heap leaching system.

Although the RTD plug flow output distribution as reported in literature, utilizing both small and large columns to interpret heap mechanism for solution hold-up (*de Andrade Lima, 2006; Bouffard & West-sells, 2009; Ilankoon et al., 2013*), *Dixon & Hendrix (1993*) noted that not all assumptions might apply to produce the appropriate plug flow distribution performance in columns. This is evident from recent studies where a major deviation of the plug flow performance was observed (*Govender-Optiz et al., 2017*; *Cherkaev, 2019*).

In operation, two distinct interactions occur in the packed beds. Hydrodynamic fluid transport and hydrometallurgical chemical extraction characterize the dissolution operation. Hydrodynamics (solution transport) is an important characteristic of heap and column leaching systems. It has received increasing attention and has been investigated in RTD studies in the literature. The hydrometallurgical leaching phase (where valuable minerals are dissolved and extracted from low-grade ores) has received very little attention with respect to utilizing it as an approach to RTD investigations. The current investigation considers the hydrometallurgical extraction using RTD studies to investigate the response of solution distribution flow type performance in packed column beds.

Basically, the project utilizes reactive leaching studies where leaching experiment is being performed with a well characterized ore. A tracer RTD study is performed followed by a leach study on the same column bed maintaining similar conditions as the RTD tracer investigations. While the conventional approach of determining the flow type performance in packed column bed is obtained by utilizing the inert tracer response, the information that would be obtained from the leach studies is anticipated to interpret the flow behaviour by comparing reaction curves to simple predicted reactive leach curves of a CSTR and multi-channel models. Hence, to achieve such reactive leaching objective, the project will utilize an ore type that will eliminate the variabilities of natural ore properties. Targeted properties would include, homogeneous mineral content, porous material, well dispersed mineral grains and uniform distribution of grains.

1.2 Problem Statement

Column tests, by and large, are used to mimic the heap leaching process. When initial irrigation occurs, the lixiviant solution preferentially meanders through available pores between particles, permeating through the bed. The time for convolution of the flow may not be the same for every channel of the individual flowing fluid. Three regimes are expected. It is assumed that some fluid percolates quickly through the particle macro voids appearing in the exit stream, others slowly penetrate the particle pores diffusing in and out, while yet others may be captured in stagnant regions where it remains stationary until driven by successive irrigating solutions. Hence, these fluids exit the column at varying times depending on the mechanism of interaction they had encountered during the flow. When the fluid exits the reactor, the discrete flow ultimately describes the flow regime responsible for the emanating fluid in the effluent stream. These flow phenomena which occur in columns are assumed to result in flow distribution performance which reflects a system that is well mixed as in a continuous agitated system; however, there are no moving parts to promote mixing.

The incongruity of RTD tracer studies with established model assumption in some cases demands that the suggested CSTR behavior needs to be understood properly to appropriately use the information in a reactor model. An approach suitable to investigate flow distribution performance occurring in a heap bed as plug flow reactor requires the residence time distribution to elucidate flow behaviour. Most studies of RTD have depended on contingent measurements of traditional soluble tracer, which lacks the ability to quantify direct information on the precise flow mechanisms occurring inside the heap. Therefore, a comprehensive literature review was carried out to understand the problem in order to develop a hypothesis to undertake the investigation.

2 LITERATURE REVIEW

2.1 Heap Leach Technology

Heap leaching is a hydrometallurgical extraction process involving solid–liquid-gas interactions in stacked piles. The solid, liquid, and gas phases are entities represented by ore particles, reagent solution, and air (oxygen) respectively. Ore particles of heterogeneous mineralogy are stationary throughout the leaching cycle. The liquid containing concentrated lixiviant solution applied from the bed top percolates through the static bed of particles dissolving metals from particle surfaces through film layers, pore diffusing into bulk solution flow, and recovering dissolved metal complexes in the effluent PLS (*Figure 2.1*) (*Petersen, 2016*). In the gas phase, air/oxygen influences metal extraction by selectively aiding the reagent enhance extraction as in the cases of oxidative sulphide leaching using microorganism (*Bouffard & Dixon, 2002*; *Petersen and Dixon, 2007*) and redox leaching of gold/silver ores using cyanide (*Bouffard & Dixon, 2007*).

The general concept of heap leaching is presented as the dissolution/extraction, and recovery of metal from low-value mineral ores into the bulk solution for further separation and recovery downstream processes. As irrigating solution infiltrates the bed, all interactions, including chemical, physical, and/or microbial, are responsible for metal dissolution. Solvent extraction and electrowinning are successive methods of separation and recovery where the ponded PLS is sent for value metal recovery (*Kartha & Srivastava, 2012; Ghorbani et al., 2016*).

As in operational large-scale heap leaching, laboratory columns are loaded with ore materials and irrigated with leaching solution. Unlike the industrial operation where the leaching is a more continuously operated system with intermittent flows at about 80~90% recovery (*Ghorbani et al., 2016, Petersen 2016*), the practice differs from laboratory columns where the operation is based on batch mode.

The feed grade of ores for heap technology are of low economic value, however, the technology is well suited for sustainable profit maximization although challenged by long extraction periods. Major cost saving utilizing the technique is attributed to size reduction limited to crushing. This makes the beneficiation process less energy-intensive; hence, the capital and operational cost of processing are lower, compared to conventional agitated systems (*Manning & Kappes, 2016*).

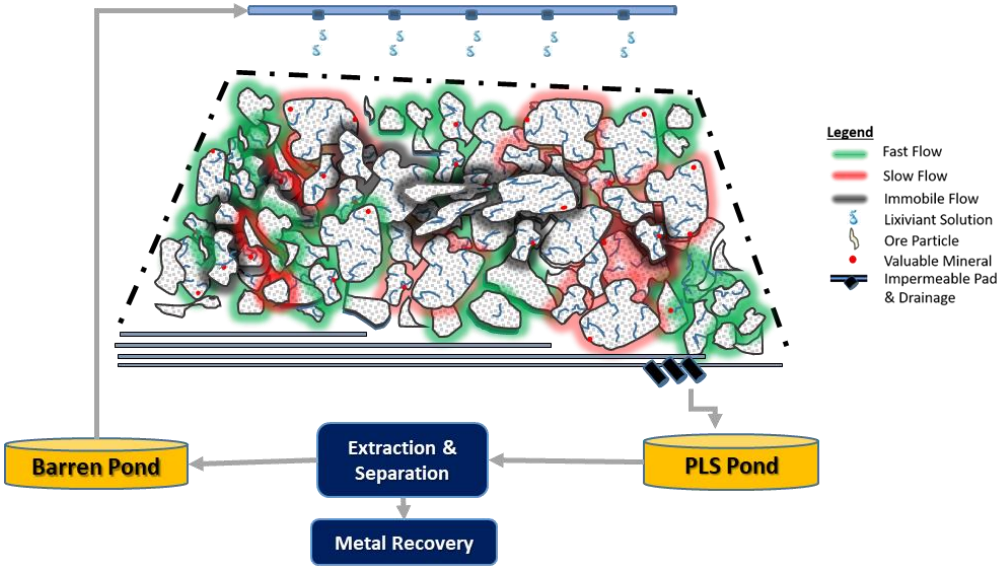

Figure 2.1 Schematic representation of heap leaching process

Although relatively adjustable and economical, heap leach technology is not ideal for metal extraction of high to medium grade economic demanding ores due to long extraction period (*Dixon & Hendrix, 1993, Ghorbani et al., 2011*); however, such high grade ores would be processed only under extreme circumstances (remoteness of the deposit or political risk) (*Ghorbani et al., 2016*).

The mode of operation may seem simple, but the beneficiation technique is a complex process with difficult physical and chemical phenomenological approaches (*Bouffard, 2003; Kartha & Srivastava, 2012; Ferrier et al., 2016*) as well as biological processes (*Petersen & Dixon 2007*). It is described to possess innumerable uncertainties and multifaceted dissolution mechanisms with somewhat unpredictable outcomes (*Dixon & Hendrix, 1993, Kartha & Srivastava, 2012*).

Such constraints provide conceivable disincentives for rapidly expanding the application industrially but suggest a motivation for intensifying scientific investigations. Risks and uncertainties associated with the technology are governed by challenges including low recoveries, long extraction times, detoxification (decommissioning) of spent heap complying with stringent environmental regulations, mass transport mechanism and bed hydrology (*Bouffard & Dixon 2001; Petersen, 2016; Cherkaev, 2019*). These challenges provoke mounting interests in order to pursue an understanding of different mechanisms affecting the nature of operation utilizing the technology.

2.2 Residence Time in Heap Leaching

One approach in studying the mechanisms occurring in packed bed heap is the determination of the interactions of the different phases in the bed through residence time investigations. Unique to understanding RTD is the stimulus-response study of tracer where two fundamental input approaches exist, pulse and step methods (*Levenspiel 1999*). A step change tracer investigation may be conducted as either a step-up considering solution entry into the bed where concentration is increased or a step-down considering residual solution in the bed eluted by water observing concentration drop in the discharge stream (*Bouffard & West-Sells, 2009; Cherkaev, 2019*). For its part, pulse injection method can be very rapid using small volumes (*Govender-Opitz et al., 2017*) or large volumes by switching between solution reservoirs (*de Andrade Lima, 2006*; *Bouffard & West-Sells, 2009*).

RTD curves provide an estimate of the fraction of the solution-containing tracer exiting the bed over the duration of the experiment. An initial delay period, an asymmetric peak (rise/fall) and a long tail characterize the RTD performance (*figure 2.2*). Narrow peaks of the RTD displayed indicate a high flow rate, while a wide or thick peak represents a slow rate of irrigation. The characteristic long tail of the RTD signifies the presence of stagnant zones indicating solute diffusion constraints; where solute transfer at the boundary of stagnant and mobile regions across pores is very slow (*Bouffard & Dixon, 2001; de Andrade Lima, 2006*; *Ilankoon et al., 2013*; *Govender-Opitz et al., 2017*).

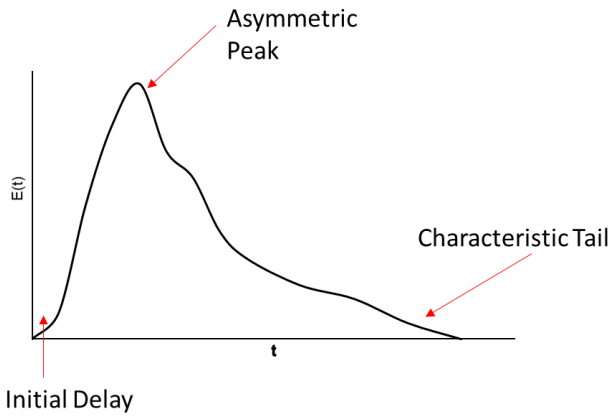

Figure 2.2 Schematic of a pulse RTD response curve illustrating its characteristic properties.

Tracer stimulation is an ultimate method frequently used as an investigative mechanism to endue solution flow transverse in heaps of various scales. Tracers usually possess characteristics of being nonreactive (inert salts), easily detectable (colour), completely soluble, and not absorbing onto the walls of the reactor (*Levenspiel, 1999*). When irrigated, tracer solution flows in no preferential channel; it is discretely convoluted

through the unsaturated fluidized bed. With such inert tracer properties, RTD investigation determines the overall time solution spends in the reactor elucidating possible interactions individual discrete fluid flow may have experienced prior to exiting in the effluent stream. Understanding the factors influencing percolation in packed bed proposed from conventional RTD investigations should inform the current investigation utilizing a reactive leaching approach.

2.2.1 ***Factors Affecting RTD in a Packed Bed***

As mentioned, heap operation is categorized into hydrodynamic and hydrometallurgical interactions. The determination of fluid distribution, retention, and transport into the effluent drainage are achieved utilizing a hydrodynamic approach; while dissolution, and extent of recovery are ultimately controlled by hydrometallurgical chemical interaction. A vast range of research investigations provided in literature outline factors affecting solution flow or hold-up in a packed bed. Axial dispersion, irrigation flow rate, mass transfer rate of solute exchange between flow regimes (mobile and immobile/stagnant flow), particle size, effect of particle size distribution, segregation, particle shape, ore porosity, column height, and flow types are factors considered (*Bouffard & Dixon, 2001; de Andrade Lima, 2006; Bouffard & West-Sells 2009; Ilankoon et al., 2013; Govender-Opitz et al, 2017; Cherkaev, 2019*). A number of factors affecting the solution flow of RTD in heap/column systems relevant to this study are reviewed.

2.2.1.1 *Effect of Particle Size and Particle Size Distribution*

Particle size plays a critical role in the performance of heap leaching operations. It is one fundamental component of heap technology, usually the solid phase in the scale of mm~cm. Unlike conventional tank leaching where particles are liberated to fine size fractions usually in microns, industrial heap leach pads exhibit vast distribution of size ranges with the co-occurrence of small and large particles possessing porous properties in order to obtain successful extraction (*Peng, 2009; Dhawan et al., 2013; Yin et al., 2016; Petersen, 2016*).

At the particle level, the surface area serves as the site for leaching activities when it encounters the irrigating reagent solution. Consequently, mineral grains on the surfaces and in inner pores of particles are dissolved and extracted for transport in solution (*Bartlett, 2013*). At the grain level, challenges exist where grains dissolved are re-deposited in pore surfaces by precipitation perhaps due to poor solubility or sparingly soluble chemical properties of the associated ore mineralogy (*Bouffard & Dixon, 2002; Petersen, 2016*); this is common for less noble metals. For metal grains that are situated in the inner pore structure of particles, percolating fluids are diffused in and out of the particle to extract these encapsulated grains; thus, making particle radius a key functional parameter in the extraction process. Rate kinetics, pore diameter, flow

dynamics, hydraulic conductivity (permeability) are among parameters that particle size significantly influences (*Dixon & Hendrix, 1993; Bouffard & Dixon 2007; Ghorbani et al., 2011; McBride et al., 2012a*).

When interacting with lixiviant solution, rapid reaction is observed with small size particles; while reaction becomes limiting in larger ones (*Bouffard & Dixon, 2007; Ghorbani et al., 2011*). A particle of smaller size possesses more micropores and a higher exposed surface area of the metal grains, while larger size results in longer internal diffusion paths in the particle. Although smaller particle size contains significant liberated grains, the occurrence of these particles invariably causes the adverse influence of solution hold-up in the heap bed. Hence the need for the optimum size distribution of particle for efficient hydraulic and extraction performance (*Dixon & Hendrix, 1993; Yin et al., 2016; Cherkaev, 2019*).

Typical particle size to heap leaching is in a broad range of less than 30 mm to about ~9 mm for coarse particles and less than 3 mm to as low as less than 75 microns for fine particles. Notably, in friable ores, fines of less than 75 microns consist of about 10% of particles in the heap (*Ghorbani et al., 2016*). It is worth noting that in industrial applications, lumps of ore from run-of-mine are directly utilized on heap pad (*Manning & Kappes, 2016*). *Table 2.1* shows the optimum operational size (OOS) and agglomerated size (AS) fractions reported to have been utilized in heap/column and modelling investigations.

Agglomeration is a size enlargement pre-treatment technique to maximize the use of fines, promote effective hydrodynamics, and reduce the possibility of stagnant regions that obstruct conveyance of reagent solution (*Sanchez-Chacon & Lapidus, 1997; Petersen, 2016; Govender-Opitz et al, 2017*). This process has proven to be successful because leaching in heaps is inherently transient characterized by unsaturated flow regime; thus, fines are not easily disintegrated from its agglomerates. The technique is reported to ensure better heap performance.

Table 2.1 Particle size used in heap experimental and modelling investigations

Size	Category	References
25.4~304.8 mm (1~12 in)		*McBride et al., 2012b*
152 mm (6 in)		*Bouffard & Dixon, 2007*
12.7 ~ 38.1 mm		*McBride et al., 2014*
5 ~ 30 mm		*Sanchez-Chacon & Lapidus, 1997*
19~25mm		*Petersen, 2016*
12~25 mm	coarse particle	*Ghorbani et al., 2011*
10~25 mm	size fraction	*Dhawan et al., 2013*
13 mm		*Negron et al., 2016*
12 mm		*Robertson, 2017*
8~11.2 mm		*Ferrier et al., 2016*

7~10 mm		*Yin et al., 2016*
9~9.5 mm	Average agglomerated size	*Bouffard & Dixon, 2002, Dhawan et al., 2013*
<3.3 mm	Considered as fines for agglomeration	*Bouffard & Dixon, 2002*
<2 mm		*Dhawan et al., 2013*
<1.7 mm		*Bouffard & Dixon, 2007*
0.1~0.5 mm		*Yin et al., 2016*
74 microns		*Dhawan et al., 2013*

In RTD investigations, although the rate of flow of the irrigated solution determines how early or late a breakthrough occurs in the effluent (*Peng, 2009*), the distribution of particle size affects the RTD hydrodynamics as well as maximum recovery. The blending mix of particle fractions results in two outcomes. (1.) unwanted creation of stagnant pools (bed consisting of larger proportion of fines consequently rendering longer residence time); or (2.) a packed bed full of voids where there is no significant particle-lixiviant contact to influence metal extraction (shorter residence time and marginal extraction) (*Bouffard & Dixon, 2001; Bouffard & West-Sells, 2009; Govender-Opitz et al, 2017; Cherkaev, 2019*). Leaching at optimum operating size (OOS) distribution results in bed performance where sufficient particle-liquid contact is achieved and fewer stagnant regions are promoted. *Bartlett, (2013)* utilizing the Gates-Gaudin Schumann particle distribution model reveals that optimum blending distribution coefficient (BDC) for crushed ore particles in heap/column leaching is in the range of $0.7 > m < 1.0$.

2.2.1.2 *Role of Bed & Particle Porosities*

Permeability is the ability of porous media to be penetrated. Importantly, permeability is viewed from both holistic packed bed channels and individual ore particles. For its part, porosity is the void space contained in a particle volume expressed as fraction or percent. Ore particles utilized in heap leaching are expected to be porous to allow solution channelling through available voids (*Ghorbani et al., 2016)*. The voids provide permeability for air-solution penetration with minimum stagnant zones. Increase dissolution and extraction of metals are dependent on the adequate distribution of air and solution through these voids (*Bouffard & Dixon, 2001; Kartha & Srivastava, 2012*). Permeability is one of the most technical factors influencing effective solution recovery in heaps. It is dependent on the mineralogy of the ore being leached (*Ghorbani et al., 2016*). Clayey materials are not ideal to be heap leached; ore consisting of clayey minerals prevent solution percolation by clogging macro-interstices, resulting in increased solution hold-up in the bed (*Dhawan et al., 2013*). It is reported that packed bed extraction performance is reduced in the event of excessive compaction, rendering minimum void available for the penetration of hydrodynamic flow of liquid and gas (*Bouffard & Dixon, 2001; Ghorbani et al., 2011*).

The heap bed is thought to have dual-porosity, i.e. macro and micropores. Macropores (inter-particle) are voids between particles in the bed, and micropores (intra-particle) are voids within the particles. Primarily, particle penetration occurs through crack networks, fractures, the random trend of grain boundaries, and contacts within micropore structures (*Ghorbani, 2012; Nwaila, 2014*). In a recent XCT study, *Ram et al., (2020)* revealed that permeability through microporous zones promote effective metal dissolution. Based on the aggressive nature of the lixiviant, gangues dissolution along these paths result in the growth of sub-micron voids. The mechanism through which the dual pore structures in heap beds promotes fluid percolation and extraction result from the coexisting effects of capillarity and gravitational processes (*Yin et al., 2016*). Capillarity governs the movements accountable for mineral dissolution in micropores, while gravity controls penetration in inter-particle macro porous regimes (*Cherkaev, 2019).* In view of such properties pertinent to metal dissolution from coarse ores, the current investigation considered microporosity as a cardinal property in the production of the artificial ore.

2.2.1.3 *Effect of Flow Rate & Fluid Flow on RTD*

Residence time studies have shown that irrespective of the type of investigation – whether using mini-columns (*Govender-Opitz et al., 2017*), laboratory-scale columns (*Bouffard & Dixon, 2001; de Andrade Lima, 2006*, *Ilankoon et al., 2013*), cribs, or demonstrated heaps (*Bouffard & West-Sells, 2009*) – two flow regions occur. Flow channels where solution penetrates the bed through particle interstices is termed as mobile flow, while flow trapped between particles clusters is considered as immobile flow. Mobile flows are fast-moving solution through the open channel between particles, usually bulk solution flow. The slow flow of fluid as film or rivulet around the boundary of particle surface was considered a part of the mobile flow regime (*de Andrade Lima, 2006*). However, later investigations considered the thin-film layered flow as part of the immobile or stagnant solution hold-up identified between particle interstices and captured fluid in inner particle pores (*Ilankoon et al., 2013*; *Govender-Opitz et al., 2017*). It must be noted here that the conceptual consideration of flow regimes in the literature vary based on the ore material utilized in the investigation. *Figure 2.3* describes the different flow regimes in porous ore bed. Slow flow movement surrounds the external surfaces of ore particles, while the immobile fluid is soaked in both intra-particle and inter-particle pore regions; transport from the mobile phase on particle surface into immobile phase inner particle occurs with minimal resistance (*Kartha & Srivastava, 2012; Robertson, 2017*).

The different flow regimes occurring in packed beds are governed by the rate of solution irrigation. RTD investigation has demonstrated that the rate of irrigation influences the bed particle-lixiviant interaction. It has been revealed that high proportion of immobile stagnant fluids in bed is possibly attributed to lower irrigation flow rate (*Bouffard & Dixon, 2001; de Andrade Lima, 2006; Ilankoon et al., 2013*). The increasing number of stagnant regions in the bed consequently respond with poor extraction of dissolved metal in solution and longer residence time. However, *Govender-Opitz et al., (2017)* proposed that the presence of

these stagnant regions promotes accretion of microbial colonies, thus enhancing dissolution of metal and transfer of solution between phases of slow and fast flowing fluids.

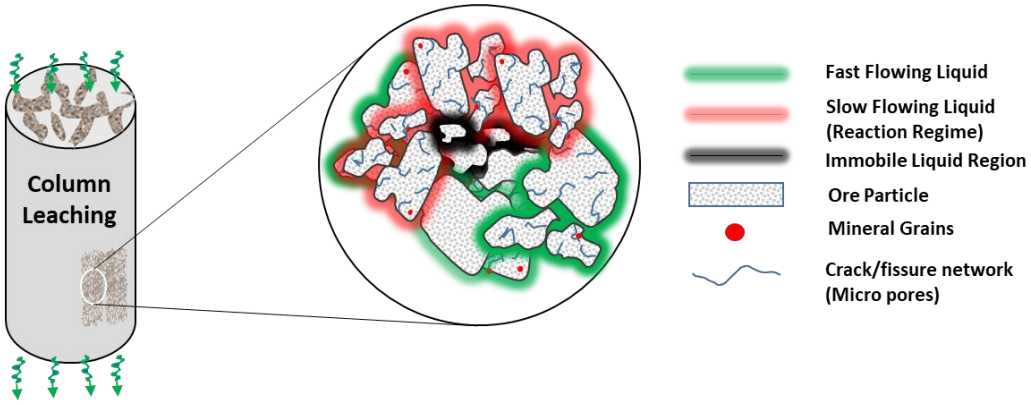

Figure 2.3 Schematic of fluid flow mechanism in heap bed

A slower flow rate invariably exhibits much longer residence time as compared to faster ones. This is attributed to fluid dissipation through the bed. *Ilankoon et al., (2013)* and *de Andrade Lima, (2006)* in their studies identified similar influences of flowrates, although their work utilized ideal particles and relatively high flow rates respectively (*Table 2.2*). This, however, becomes relatively open-ended if the flowrate is compared against anything. The typical irrigation rate in heap applications is reported to be in the order of 3 - 20 L/m²/hr (*Bartlett 1998; Bouffard & Dixon, 2001; Bouffard & West-Sells, 2009; Free, 2013; Cherkaev, 2019*).

A number of RTD studies reported that characteristic tails indicating the availability of stagnant zones were shortened to some extent when flowrate was increased (*Bouffard & Dixon, 2001*; *de Andrade Lima, 2006; Peng, 2009; Ilankoon et al., 2013*) *Figure 2.4a-c*. It must be pointed out that these RTD investigations utilized flowrates both typical and extremely out of range to heap irrigation, evident in *Table 2.2*. A recent RTD investigation revealed that irrespective of the particle size distribution, the packed bed is insensitive to flow rate variation in the range of 3, 10, and 20 L/m²/h typical to heap operational parameter and even up to 40 L/m²/h (*Cherkaev, 2019*). In the study, no change in the effect of solution hold-up from stagnant zones was observed with the varying flow rates *Figure 2.4d*. The author reported that given a blend of PSD, reactor volume is relatively constant and the inherent residence time is not dependent on the flow rate variation.

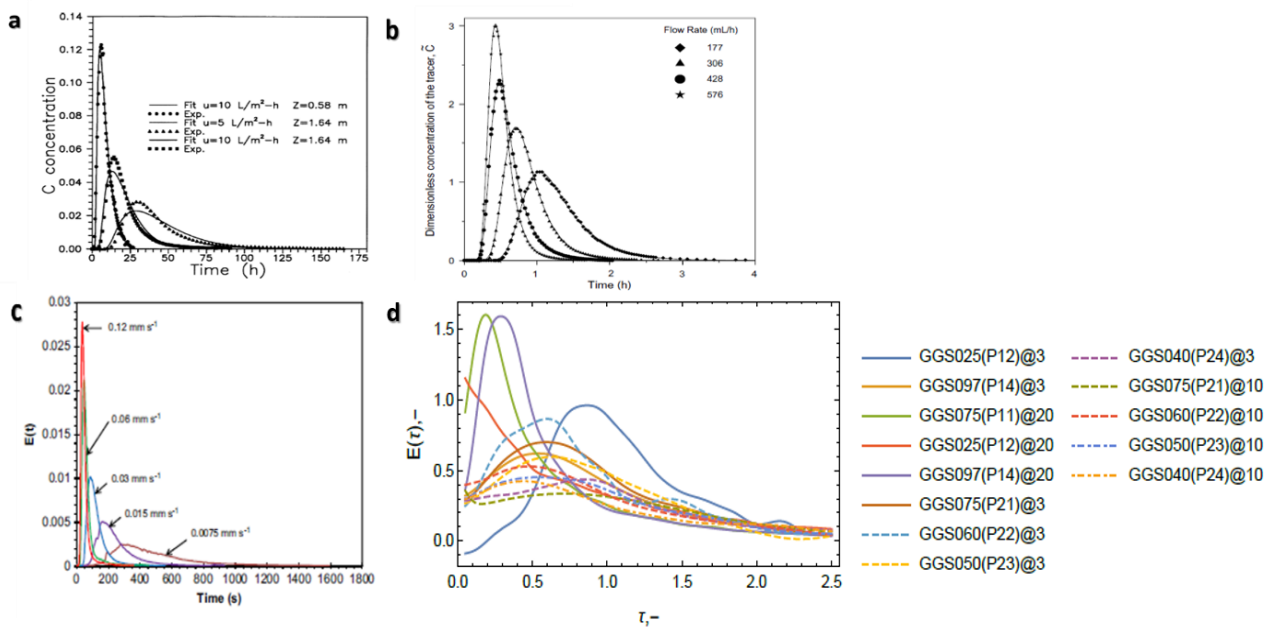

Figure 2.4 RTD graphs illustrating effects of increasing irrigation rates adapted from (a) Bouffard & Dixon, 2001; (b) de Andrade Lima, 2006; (c) Ilankoon et al., 2013; and (d) Cherkaev, 2019.

Table 2.2 Heap leaching parameters from different RTD investigations.

Tracer	Ore type	RTD	Tracer recovery	Irrigation flowrate	Height	Diameter	Particle size	References
$NaNO_3$	Refractory Gold			3 L/m²/h	6,1 m	25cm	Crushed ore(random sizes)	*Bouffard and West-sells, 2009*
$CaCl_2$	Glass beads	100 s	~95%	318 L/m²/h	300 mm	283 mm	18 mm	*Ilankoon et al., 2013*
$CaCl_2$		500 s	~95%	20 L/m²/h	300 mm	283 mm	18 mm	*Ilankoon et al., 2013*
$CoSO_4 \cdot 7H_2O$	Copper Ore	220 min (Steady State)	~90%	10 mL/h				*Govender-Opitz et al., 2017*
$CoSO_4 \cdot 7H_2O$		205 min (Unsteady State)	~90%	10 mL/h				*Govender-Opitz et al., 2017*
HCL	Quartz			69.39, 119.98, 167.81, 222.31 L/m²/h.	83cm	5.7 cm	2.17 mm	*de Andrade Lima,2006*
$NaNO_3$	Refractory Gold	95 hr	~95%	5 L/m²/h	180 cm	25.4 cm	<19 mm	*Bouffard & Dixon, 2001*
		18 hr	~95%	10 L/m²/h	50 cm	25.4 cm	<19 mm	*Bouffard & Dixon, 2001*
		45 hr	~95%	10 L/m²/h	180 cm	25.4 cm	<19 mm	*Bouffard & Dixon, 2001*
KNO_3	Refractory Gold			3, 10, 20, 40 L/m²/h			<26 mm	*Cherkaev, 2019*

2.2.1.4 *Flow Types in Heap Investigation*

Packed bed reactor performance is distinguished by distribution curves obtained from RTD investigations that interprets and predicts the possible interactions pertinently occurring between the solid-liquid phases. It is well established that laboratory RTD investigations are expected (*Dixon & Hendrix, 1993*) and has been proven to produce characteristic curves more similar to plug flow type behaviour (*Petersen & Petrie, 2000, Bouffard & Dixon, 2001; de Andrade Lima, 2006; Bouffard & West-Sells, 2009; Ilankoon et al., 2013*). Figures adopted from literature sources are illustrated in *Figure 2.5*.

Irrespective of the flow rate (either typical to or largely deviating from heap application), type of feed particles, single or multiple particle size distribution, and the conceptualized focus of the investigation, unique to the aforementioned studies were RTD curves (either *F*- and *C*-curves) similar to that for a plug flow type system.

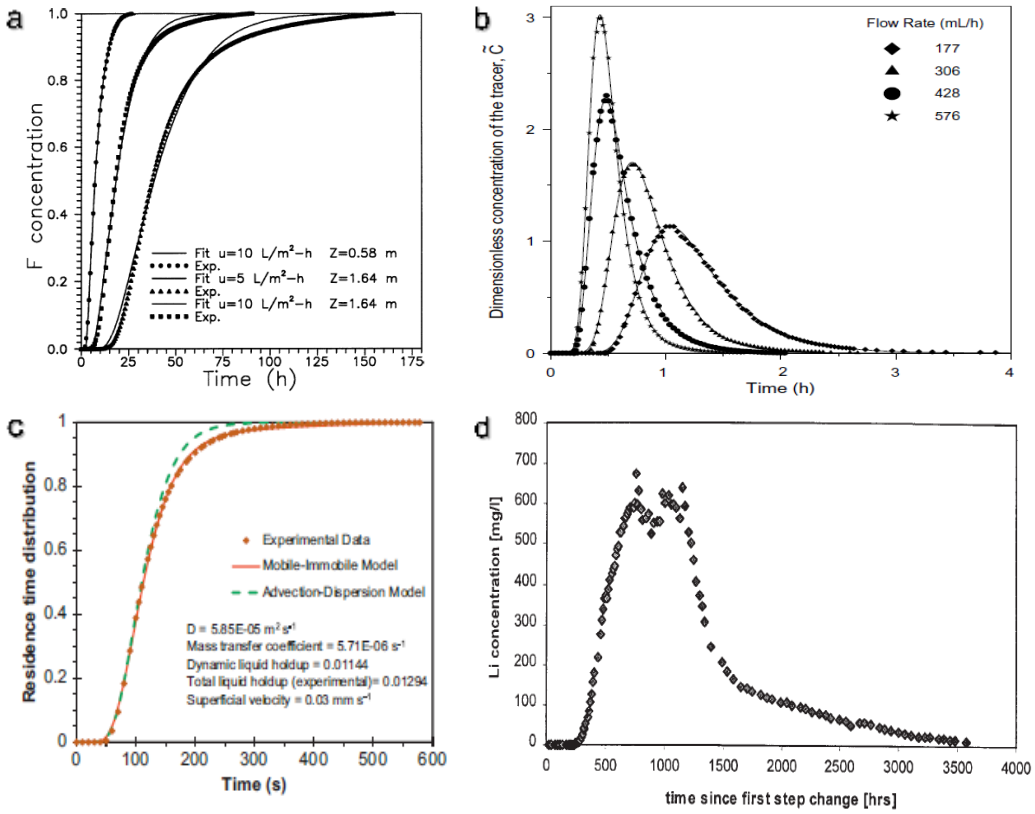

Figure 2.5 Illustration of plug flow type
(a). Plug flow performance with varying column height and irrigation flow rate adopted from (Bouffard & Dixon, 2001). (b). Plug flow output in an RTD investigation determining solution hold-up at varying flow rate adopted from (de Andrea, 2006) (c). Determination of dispersion coefficient at varying flowrate parameters adopted from (Ilankoon et al., 2013), and (d). Lithium tracer concentration profile ferro-chromium slag material column experiment adopted from

While the mechanism of operation in column beds remain to be approximated to plug flow distribution performance, other RTD investigations encountered a flow distribution where the output performance reflected curves similar to a CSTR flow type (*Govender et al., 2015; Govender-Opitz et al., 2017; Cherkaev, 2019)* (*Figure 2.6*).

Noteworthy, column flow type performance in RTD investigation has not gained much attention. To date, there has been little reliable evidence for the anomaly in the flow performances. It is believed to be of growing importance in the light of its prevalence of use in recent studies. With the flow type producing different performance curves that largely deviates from a single operational mechanism, this has prompted the interest to understand reactor performance from an experimental approach using RTD investigations of both conventional inert tracer and innovative reactive leaching techniques.

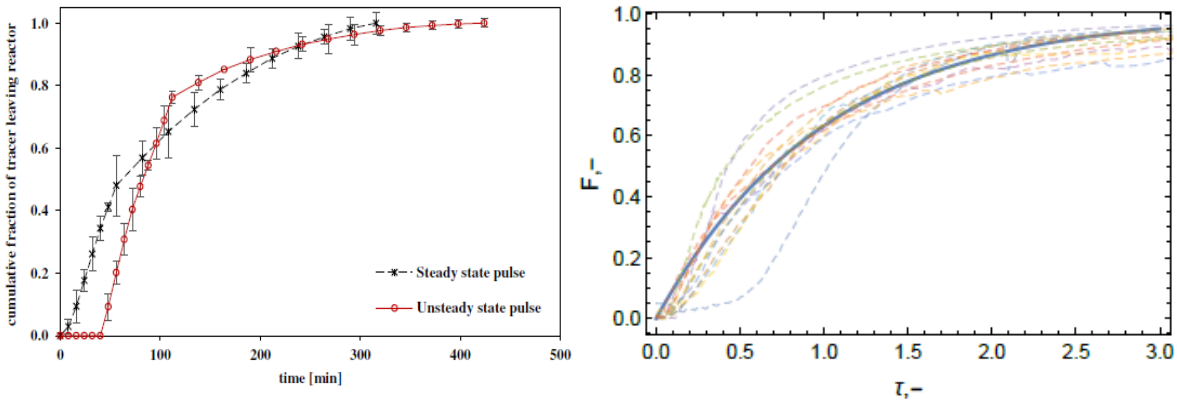

Figure 2.6 Illustration of CSTRflow type
RTD curve demonstrating well mixed CSTR flow behaviour observed in mini column reactors (Govender-Opitz, et al., 2017)[left] and validation of experimental results with single CSTR model showing a well-mixed RTD output laboratory reactors (Cherkaev, 2019)[right].

2.3 Modelling Approaches to Heap RTD

The use of heap modelling approaches has aided the advancement of scientific research and commercial applications of the technology (*Dixon & Hendrix, 1993; Sanchez-Chacon & Lapidus, 1997; Petersen & Petrie, 2000; Petersen and Dixon, 2007; McBride et al, 2012b, 2014*). The conventional inert tracer technique used in understanding the interactions of fluid travel through column bed has received much attention in the literature (*Bouffard & West-Sells, 2009; Cariaga et al., 2015; Govender-Opitz et al., 2017, Cherkaev, 2019*). In these investigations solute transport in packed bed systems is modelled utilizing hydrodynamic parameters established from tracer studies combined with topological particle-level models to predict the bed performance. Thus a number of different models developed have been used in such RTD investigations (*Dixon & Hendrix, 1993; Sanchez-Chacon & Lapidus, 1997; Petersen & Petrie, 2000; Bouffard 2003; Cariaga et al.,*

2015). *Cherkaev (2019*) proposes a modelling approach which takes into account the reaction source term considering the dissolution taking place at the mineral grain surfaces – to elucidate the flow distribution. This novel attempt allows to elucidate possible inherent multiscale interacting mechanism in low-grade packed rock bed systems..

To validate the applicability of generic models to the coarse particle dissolution system requires comprehensive laboratory experimental leaching to determine the intrinsic reaction kinetics at the coarse particle level and for the bulk bed mineral dissolution system (*Ferrier et al., 2016*). However, the reaction source term of a generic hydraulic model may be calibrated against data that might not adequately fit any leaching reaction system thus resulting in development of model to suit each reaction case. This relies on the use of existing particle level mineral conversion models, such the shrinking core model or extended topology model (*Ghorbani et al., 2013*), which have proven to be appropriate in characterizing mineral dissolution from coarse particles. Kinetic information from such models thus obtained can be translated into more comprehensive RTD hydraulic models (*Bouffard, 2003; Cherkaev, 2019*). This approach possibly reduces invariabilities that may affect fitting the models to extraction results of the system.

2.4 Leaching of Gold/Silver Ores

Considering the interest of utilizing silver as the targeted metal in the proposed homogeneous ore material, this project seeks to provide an opportunity to advance the understanding of the chemical kinetics. This section considers reviewing essential leaching parameters that characterize metal extraction in sodium cyanide media as well as contributions of visualizing imaging techniques to elucidate chemical interactions in ore particles.

Gold and silver usually occur together in many ore mineralogies. While gold occurs naturally as a native metal, silver occurs in several forms characterized in sulphides and compounds with other metals (Au, Hg, Sb, As, Cu, Pb and Pt) as well as in native metal (*Marsden and House, 2006; Bouffard & Dixon, 2007; Teja Ruiz et al., 2017*). However, their chemical characteristics are similar, thereby inheriting similar processing techniques. In low-grade ores, mineral grains deportment occurring as very fine inclusion are disseminated in the interlocking mineral gangue phases thus making low-grade ores inefficient for traditional tank leaching operation.

2.4.1 ***Chemical Kinetics***

Chemical reactions occur initially at high leaching rate on the mineral surface in packed beds. A number of researchers have reported that depending on the dissolution rate and the exposure of metal grains to percolating reagents, reaction of non-refractory gold oxide can achieve recovery as high as 90% during a

heap leach cycle (*Yin et al., 2016*) and silver at 55% (*Manning & Kappes, 2016*). Chemical leaching kinetics are reported to be influenced by reactant concentration, pH, the reaction of gangue phases, and temperature change (*Marsden and House, 2006*; *Esmkhani et al., 2013; Free, 2013; Petersen, 2016*).

Gold/silver ores are naturally heterogeneous, exhibiting different rates of reaction. Variable chemical conditions exist in the particle as the result of variable grain sizes; the rate constant at these conditions reacting at surface sites are not linear as may be expected in a homogenous system with similar grain characteristics (*Nwaila, 2014*; *Govender-Opitz et al, 2017).* Variable leaching kinetics in ore of similar characteristics result from the instantaneous availability of large mineral grains/nuggets in the particle (*Bouffard & Dixon, 2002*; *Ghorbani et al., 2011*). Gold/silver grains are in a range of 1 ~ 10 µm. With a narrow grain size variation, chemical leaching is invariably constant in heap bed except limited by cyanide consuming mineral associations (*Bartlett 1998*).

2.4.2 ***Reactions***

Leaching behaviour in heaps can be categorized into three reaction fronts; mineral grain, single particle, and collection of particles (*Ferrier et al., 2016*). Lixiviant-particle interaction functions at the mineral surface; such extraction regions are expected to have sufficient contact to incur complete dissolution reaction at the surface and partial dissolution into the inner particle pores (*Bartlett, 2013*).

The chemical reaction of gold/silver ore is an oxidation-reduction process where the reagents in solution are dissociated into ions reacting at surface sites of particles to dissolve metallic mineral grains into soluble metal complexes and diffuse back into the bulk solution. The precious metals chemically dissociate according to a stoichiometric relationship elucidated in the reaction as follows in *Eq 2.1* and *Eq 2.2*, where the stability constants for both gold and silver are log β_2 = 39.3 and log β_2 = 20.48 respectively *(Wang et al., 1990).*

$$4Au + 8NaCN + O_2 + 2H_2O = 4NaAu(CN)_2 + 4NaOH \qquad \textit{Eq. 2.1}$$

$$4Ag + 8NaCN + O_2 + 2H_2O = 4NaAg(CN)_2 + 4NaOH \qquad \textit{Eq. 2.2}$$

At the grain level, the metal dissolves in cyanide anodically while oxygen is reduced on the gold surface cathodically. In a stoichiometric relationship, the dissolution of 1 mole of gold/silver metal requires 2 moles of cyanide and ¼ moles of oxygen to produce 1 mole of complex dissolve metal solution. While the leaching of silver is chemically analogous to gold, percent recovery of silver tends to be less than that of gold due to

significantly slower dissolution reaction rate; however, silver occurs at higher grades than gold in rock host lithology or concentrate feed (*Deitz & Halpern, 1953; Habashi, 1967; Marsden & House, 2006; Manning & Kappes, 2016*).

2.4.3 ***Reagents***

Reagents used in the cyanidation of gold/silver ores include cyanide, water, oxygen and pH buffers.

2.4.3.1 *Cyanide*

Cyanidation with gold is more reactive than silver. This is due to the reason that gold is native metallic while silver is semi-metallic occurring in variations of insoluble chemical compounds (e.g. antimonides and arsenides). Maximum recovery of silver and gold from the industrial operating heap is typically about 55% and 70% ~ 90% respectively. While the average concentration of sodium cyanide (200 ~ 600 mg/l) is required for the leaching of gold, a significant amount of sodium cyanide (600~1000 mg/l) is needed for silver recovery (*Manning & Kappes, 2016*). In the leaching process of precious metals from mining waste or tailings, an extremely high concentration of cyanide (2.5 ~10 kg/t) is required (*Kasaini et al., 2008*). In industrial heap leaching, cyanide concentration in the range of 0.1 ~ 1.0 kg/t is required to offset probable consumption by volatilization, oxidation, or complexation by other mineral constituents (*Ghorbani et al., 2016)*. Largely, a significant amount of cyanide is needed to overcome undesirable side reactions and increase dissolution recovery of the gold/silver metal present. The presence of solid reactants amendable to the reagent other than the anticipated value mineral may affect the overall leach kinetics with high competition for available lixiviant in solution. Most common soluble impurities in gold/silver cyanide systems are copper, zinc, mercury, nickel, and iron known as cyanicides (*Habashi, 1967; Esmkhani et al., 2013; Manning & Kappes, 2016*).

2.4.3.2 *Oxygen*

Oxygen is a gas phase reagent that accompanies cyanide (liquid phase) in the oxidation process at the particle surface (solid phase); this process is applicable typically to non-refractory gold oxide ores (*Bartlett, 2013*). The amount of oxygen needed for the reaction of cyanide with gold/silver metal is marginal (7 ppm) but still important.

The significance of oxygen depletion is shown much attention in refractory ores where sulphidic constituents (pyrite) have the tendency to rapidly react, exhausting the available oxygen (*Bartlett, 2013, Ghorbani et al., 2016*). The presence of cyanicides (sulphidic minerals) promptly consumes available cyanide and oxygen, making the precious metal extraction very slow (*Marsden and House, 2006*). Based on this dissolution retardation, oxidative bioleaching has been suggested and is used as an optimum economic pre-

treatment method for sulphidic refractory gold/silver ores (*Bouffard & Dixon, 2002; Petersen & Dixon 2007; Petersen, 2016*).

2.4.4 *Effect of Temperature on Gold/Silver Heap Leaching*

It is reported that an increase in temperature results in an increase in the reaction extraction rate (*Bouffard & Dixon 2007; Hlabangana et al., 2018*). Higher temperature reduces the viscosity of the reagent solution and promotes diffusion (*Esmkhani et al., 2013*). It was put forward that in the leaching of gold/silver ores, increasing temperature enhances extraction recovery until maximum recovery of gold is attained at a temperature in the range of 80 °C ~ 85 °C (*Julian et al., 1921; Habashi, 1967*). However, extraction decreases at higher temperatures beyond 85 °C. The decrease in extraction is possibly attributed to gas (oxygen) solubility that tends to decrease with increasing temperature (*Marsden and House, 2006; Esmkhani et al., 2013; Hlabangana et al., 2018*).

It is, however, worth noting that in industrial gold/silver heap cyanidation system, the blanket of air surrounding the footprint is essentially sufficient for providing ambient conditions for the precious metal dissolution (*Ghorbani et al., 2016*).

2.4.5 *Effect of pH and pH Buffers*

Generally, gold/silver leaching is an alkaline process where the pH is usually 10~11. Although in acidic regions cyanide attack is highly selective for the precious metals, very toxic hydrogen cyanide gas is produced according to *equation 2.3* which incur a high level of safety concerns. The equation describes the hydrolysis of cyanide ion responsible for depleting free CN^- ions in solution at low pH range below 9.5.

$$CN^- + H_2O = HCN + OH^- \qquad \textit{Eq. 2.3}$$

Excess alkalinity, however, decreases the rate of dissolution at a pH level above 12. This is due to the dissolution of silica (*Manning & Kappes, 2016*), decomposition of cyanide by atmospheric carbon dioxide (*Habashi, 1967*), formation of calcium oxide film on the metal surface from the buffer salt (*Deitz & Halpern, 1953*), and the formation of passivating oxide layer on the metal surface caused by the presence of arsenic and antimony sulphides (*Marsden and House, 2006*).

Optimum pH condition for gold/silver dissolution in cyanide media remains at pH 10 ~11 (*Marsden and House, 2006; Bartlett, 2013; Petersen, 2016*). Chemicals responsible for obtaining and maintaining pH at specified operating conditions are NaOH, CaO, or Na_2CO_3 & $NaHCO_2$ (*Nwaila, 2014)*. However, *Deitz & Halpern, (1953*) have revealed that at high alkalinity (pH ~ 11.5) CaO creates a film on the surface of the mineral thereby inhibiting extraction.

2.4.6 *On the Rate Controlling Step*

In the leaching process, the extraction is driven by the slowest rate controlling mechanism. Essentially two phenomena exist, namely reaction kinetics and mass transport occurring in heap operation. Either phenomenon is considered to be limiting when its effect impedes the progress of extraction of the value metal from ores. The rate-controlling phenomena of coarse particle heap leaching have been subjected to considerable debate in gold/silver heap investigations (*Sanchez-Chacon & Lapidus, 1997; Bartlett, 1998, Bouffard & Dixon, 2007*).

It has been established that diffusion governs extraction in coarse particle leaching (*Sanchez-Chacon & Lapidus, 1997*; *Bartlett, 1998*). A contrary view was purported by *Bouffard & Dixon (2007)* where it was argued that the controlling mechanism was predicted to be reaction kinetics. However, their study did not take into account the heterogeneous nature of gold metal grains (in terms of size) occurring in the ores that could have possibly affected the dissolution by increasing the dissolution time of extraction. What is not considered in the investigation is the absence of a microscopic determination of the metallic grain size distribution in the utilized oxide ore for their studies.

Another investigation proposed that in large particle leaching, dissolution mechanism is either diffusion-controlled, surface-chemical reaction-controlled, or diffusion-reaction controlled dependent on the availability of induced cracks/fissures to the material promoted by the comminution mode (*Ghorbani, 2012*). Leaching of coarse particles is characterized by diffusion influences considering the pore radius of the particles and their inherent torturous property that is overcome to some extent by the fractures available.

2.5 Micro-XCT Characterization

An anticipated visualization technique proposed in this investigation is the use of Micro X-ray Computed Tomography technique. In principle, CT operates where a beam of X-rays is shone through a particles at various angles and the variation of the attenuation of the beam is then analysed to re-construct a 3D image of the sample. X-ray CT technology is based on the energy intensity of the linear attenuating coefficient relative to the atomic number and density of the sample at the point of detection. It is an advanced diagnostic high-resolution non-destructive visualization technique used to describe the characteristics of the internal structure of solids. It has been proposed to be an adequate tool for 3D data acquisition for mineralogical and structural coarse particle investigations (*Morrison & Gu, 2016*). Usually, the technique is coupled with traditional 2D measurement techniques (MLA or QEMSCAN) for validation of mineral deportment.

Despite all of the advancements in XCT, it has its limitations; minerals with similar densities occurring in a sample makes them hardly distinguishable compared to minerals containing clearly discernible densities.

Using the technique, high attenuation suggests minerals with high densities usually bright grains. However, it is reported that using only density to distinguish minerals present is misleading. Using both the empirical formula and density of the sample mineralogy to obtain the attenuation coefficient is a much more reliable approach (*Bam et al., 2020*). Furthermore, another limitation of the technique is observed in the provision of contrasting signals of high-density solids between air-liquid phases (*Ghorbani et al., 2016).*
Thus, in order to use the technique effectively to distinctly recognize minerals present, calibration is proposed (*Ghorbani, 2012*). With the use of a homogeneous ore matrix constituting only one highly dense mineral present, these limitations are perceived to be avoided in this current investigation.

2.6 Critical Review Summary

Heap leaching technology is considered a feasible technique for the beneficiation of low-grade porous ores. Laboratory columns are used to mimic and study heap leaching performance through RTD studies. Findings from investigations at this scale are not safely adaptable to the actual large-scale operation but require investigation on incremental stages as in cribs to demonstrated pilot studies. The review of the literature has established that RTD of fluid in column bed reactors is affected by several factors that influence the tracer/lixiviant distribution performance. Those relevant to this investigation were particle size and size distribution, flow rate, ore porosity and flow type. These factors determine interactions plausible between the ore particles and lixiviant relative to the time it takes the fluid to reside in the bed.

Varying particle size fractions from boulders or ROM (cm-mm) down to fines (microns) are possible in a heap. The effectiveness of the heap to perform in terms of particle parameter is dependent on the reduction of fines (agglomeration) and the distribution of the size fractions of the feed particles. The reacting volume or retain liquid in a reactor is revealed to be constant irrespective of the irrigation rate in the range typical of heap operation. While this is so, the convoluting fluid experiences fast movement, slow movement, and fluid held in stagnant or dead zones. These flow regimes are characterized by distinct residence times. This review revealed that RTD reactor flow type performance largely depends on the bed PSD and flowrate parameters. While reactor height is not considered here, it cannot be overlooked.
At present, the RTD flow type performance of column flow type behaviour determined from inert tracer studies is not clear, which suggests room for other interest areas that could possibly aid the understanding of flow performance.

RTD studies primarily serve the purpose of characterizing the fluid flow through a reactor system. The information gained from such studies can then be used in the formulation of a suitable reactor model. This is no different in heap leaching. In reactor models, a fluid flow model is linked to a chemical reaction kinetic model. Given the complexity of heaps, approximation need to be used and the question is to what extent the approximations capture the real reactor behavior. Essentially, these models are either plug-flow models

combined with some particle-level reaction model (such as shrinking core) or they are flow-channel (plug-flow) / side-branch diffusion models (also known as dual-porosity models). These different models deliver typical RTD responses, which often do not match well with what is measured from 'classic' RTD studies. Quite clearly, this finding makes no sense as heaps have no part being 'mixed' and a CSTR approach cannot be used to model heap reactors, as the system is physically different and will result in a different model prediction becoming completely misleading.

Determination of the effective chemical interaction during the leaching process promotes the understanding of lixiviant-particle extraction as it relates to the factors influencing solution flow in packed beds and provide insights into improving extraction in the effluent streams. Primarily, pH, reagent concentration, associated minerals present, oxygen, and temperature govern the dissolution of silver by cyanide in low-grade metal disseminated ores. In ores where minerals likely to compete with silver are absent, the literature reveals that ambient oxygen and temperature conditions, as well as lower sodium cyanide concentrations (200~500 mg/L), are optimum for the dissolution extraction.

With the findings obtained from the review of the literature, this study formulates the proposal of a new technique to investigate RTD flow type response.

2.7 Hypothesis

It is therefore postulated that the peculiar RTDs of heaps/columns are a consequence of the convoluted flow-paths encountered in heaps, some of which are long-winded and some straight-through, and their distribution is relatively random given the nature of the bed, but the larger the fines content in the packing, the larger the probability of a distribution of long paths relative to short paths. As a result, an RTD study will result in a wide distribution of channels with many different individual residence times and hence the distribution will resemble that of a mixed reactor more where the same principle applies (as distribution of random paths of any fluid 'particle' from inlet to outlet).

2.7.1 *Key Questions*

Reactive leaching indication of sodium cyanide as the lixiviant amendable in dissolving metal from the ideal ore will be based on extraction data of artificial silver ore and compared to the reactor flow performance of the nonreactive (potassium nitrate) tracer to interpret the flow pattern.

Key questions are presented to interpret the hypothesis.

- What could be responsible for a plug flow reactor (PFR) residence time curve to demonstrate a CSTR flow type performance?

- What effect would the changing parameter conditions of flow rate and particle size distribution have on the dissolution kinetics in the column reactor?
- How do the changing parameter conditions of flow rate and PSD influence the flow type performance of both nonreactive RTD and reactive leaching response?
- Would the chemical kinetics of the reactive leaching technique adequately interpret the flow type response?
- What could be the influencing factor if the lixiviant residence time is shorter than the time of reaction or vice-versa?

2.8 Project Objective

The aim of this study is to investigate the RTD flow performance of laboratory column using conventional nonreactive and reactive leaching techniques. Hence, the following set of objectives were developed to understand the nature of the research and possible outcomes.

- To understand what causes a static multi-channel plug flow system to exhibit a perfectly mixed CSTR system flow distribution.
- To produce an artificial ore that will be ideal in the following properties:
  - Homogeneously Porous
  - Uniform grain size distribution
  - Highly dispersed grains
  - Even head grade distribution
- Use visualization techniques to characterize the artificial ore and validate the ideal properties.
- Perform leaching characterization studies on the ore material to achieve optimum operating parameters for the column leaching investigation.
- To understand the influence of particle size blending and flow rate on RTD hydrodynamics and reaction kinetics.
- Relate both RTD experimental data to an existing plug flow and CSTR models to determine the flow type performance.

2.9 Research Approach

Towards the approach taken to proving the hypothesis, essentially this project seeks for an experimental proof of what *Cherkaev, 2019* has already proven using a modelling approach. The concept here is to conduct conventional tracer studies in a given ore bed and compare this to the same ore bed under reacting conditions. In order to do this, the ore bed needs to react as homogenously as possible to eliminate noise such as nugget effect, uneven particle porosity, random dispersion and distribution of mineral grains. Hence the need to create an 'ideal' ore artificially – here the study use the idea from *Dixon & Hendrix, (1993)*. Prior to the tracer RTD and reactive leaching investigations to compare the test results qualitatively, a considerable portion of this project focuses on the development and characterization of this ideal artificial ore leaching behaviour.

In order to achieve the objectives of the investigation, the study was contextualized into three stages including the production of artificial ore, characterization studies (Micro-XCT and leaching kinetics) of the ores, and RTD column investigation (*see Figure 2.7*).

Artificial silver ore was prepared manually to be utilized in all the investigations. It can be noted that a real ore sample may contain variation in grain size, uneven distribution of grains, and a significant amount of gangue matrix in the ore. These variables may result in too many different uncertainties influencing the reaction interaction. Thus, in order to reduce this uncertainty to a single variable to relate to the objectives of this investigation, it was resolved to develop and use an artificial ore. Such ore characteristics will allow for much more control in the ore.

Reaction kinetics, particle size, metal grain size, volume % porosity, lixiviant concentration and temperature effects were determined independently in the characterization studies. Micro-focus X-ray computed tomography characterization technique was used to validate the ideal nature of the synthetic silver ore. The influence of irrigation rate and particle size distribution were investigated during the column RTD experiments using both nonreactive tracer and column leaching techniques. The governing mechanism of the leaching dissolution in the characterization studies was determined with the use of the shrinking core and extended mixed topology models. RTD experimental data were examined with the application of existing simple plug flow and CSTR models to obtain interpretations to validate the flow performance. While leaching results were examined with simple particle blending model incorporating the extended mixed topology model.

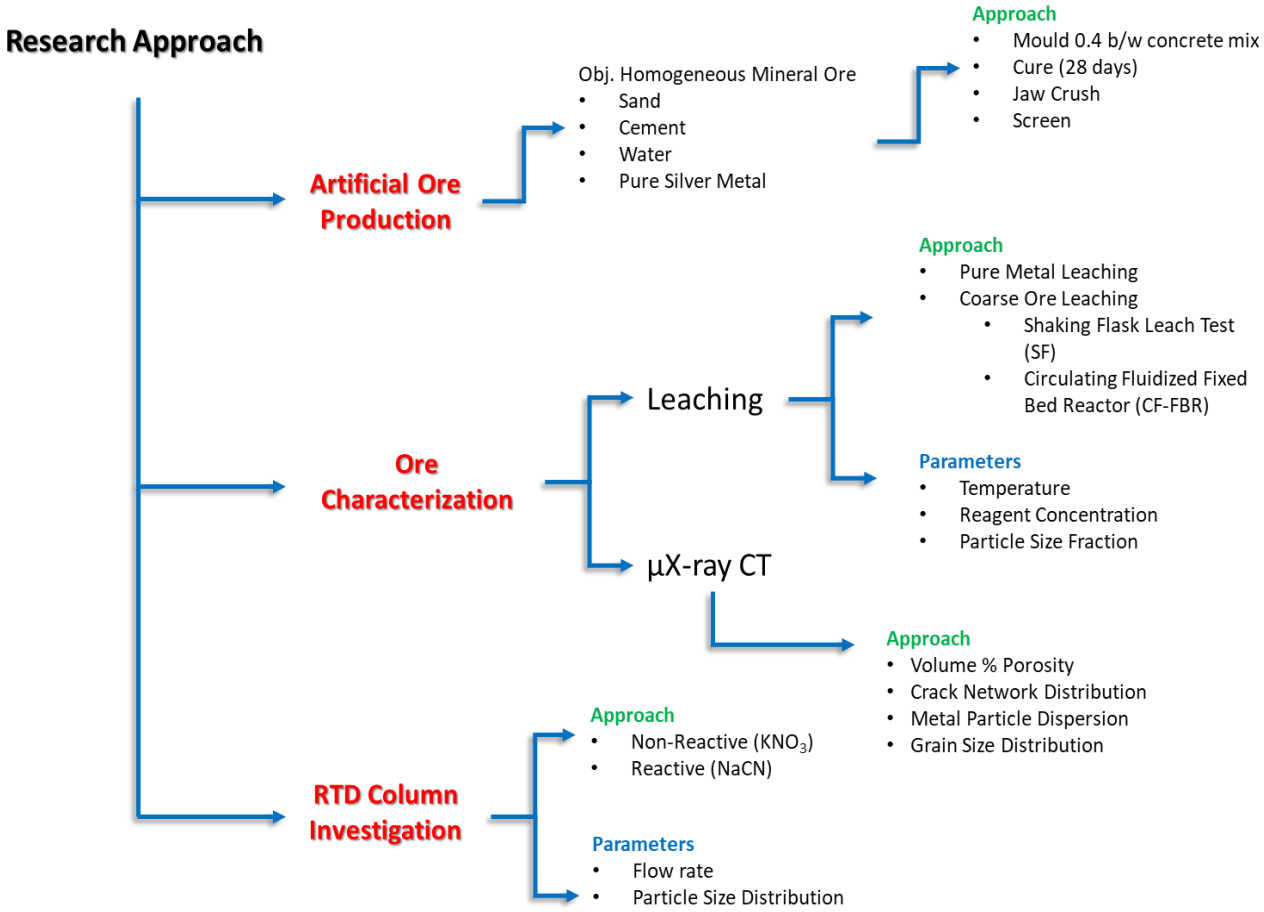

Figure 2.7 Research approach schematic

3 MATERIALS & METHODOLOGY

3.1 Introduction

Procedures, equipment/apparatus, materials, and methods used in this investigation are presented in this section. Experimental plans outlined here are expected to satisfy the project objectives and validate the postulated hypothesis. The following are areas of emphasis of the project.

- Micro X-Ray characterization of the artificial silver ore of its ideal properties.
- Leaching characterization of pure silver metal and the artificial silver ore of variable particle sizes.
- Determination of performances governing residence time distribution of packed column beds.

In order to address the outlined project objectives emphasized, various sections of this chapter was developed. Section 3.2 discusses the methodology of the artificial ore preparation and grade analysis with respect to the size fractions utilized in the study. Section 3.3 presents the reagents and parameters of solution preparation. Procedures and methods used in the leaching kinetics and visual characterization is presented in section 3.4. Column residence time study procedures, conditions, and methods are detailed in section 3.5.

3.2 Artificial Silver Ore

3.2.1 *Preparation*

Throughout this study, the use of artificial silver ore, free of reactive gangues, was utilized. By this, the ore would need to possess certain homogeneous properties, notably in mineral constituent, metal distribution, grain size, and material porosity. In order to obtain such ideal ore sample, an artificial ore was made from a b/w 0.4 mixture of cement, sand, water, and known amount of silver powder, APS 4-7 micron, 99.9% pure (metal basis), with a surface area of 0.1~ 0.4 m^2/g with average grain size of 5.4 micron. The metal was obtained from Alfa Aesar through LGC Industrial Analytical ZA. *Table 3.1* presents the matrix detailing the mortal mix.

Table 3.1 Single mortal mix per batch produced

Casting Mix		Units
Sand	11,09	kg
Cement	6,95	kg
Water	2,78	kg
Metal (Silver)	10	g

3.2.1.1 *Manual Ore Mix Production*

The production of synthetic ore was performed manually to improve the spatial distribution of metal in the concrete mix. This approach was considered due to reason that in a preliminary leaching study (*Gani & Manzila, 2018*), a concrete mixing machine was utilized to produce the synthetic ore but did not seem to have distributed the metal grains effectively. Although the manual mixing method is labour-intensive and time-consuming, this robust approach was used in order to minimize errors of the metal distribution in the ore. Considering the large volume of material (ore) needed for this investigation, the production was divided into six (6) batches and manufactured according to the b/w 0.4 mixture of *Table 3.1*. The process was approached primarily by mixing the cement and silver powder incrementally; i.e., for instance, taking 3 trowel loads of cement (approximately 695 g) to 1 g of silver powder and mixing it for a period before repeating the step. This was done cumulatively until the 10 g of silver per batch was exhausted into the cement mixture. The sand was then added to the mixture at 1.5 kg after every 5 min interval of thorough mixing. After a period of full dry mix visible as a grey matrix *(see Figure 3.1a)*, water was added and the final mixing was achieved.

Figure 3.1 Batch ore production (a) thorough mortal mix before water addition, (b) curing cylindrical lump ore sample.

The mortar was moulded into small plastic bags (average dimensions about ~ 40 mm diameter and ~70 mm height). The concrete ore was left to cure for a period of 28 days at room temperature (*see Figure 3.1b*). The final cured ore was cylindrically shaped with an average diameter of 35 – 40 mm. The ore shape and dimension was sizable to directly fit into the laboratory jaw crusher.

The artificial ore preparation was modified after *Dixon & Hendricks, 1993* where their ore was made into pellets. Whereas in this investigation, the ore was made in large lumps about ~ 40 mm in order to be

crushed, that should represent random shapes from the primary crushing feed as is obtained in industrial applications.

3.2.2 *Particle Sizing*

After a 28 day period of curing, the lump samples were crushed and screened using a TM Engineering laboratory jaw crusher and a Fritsch (Labotec) vibrating screen respectively. The crushed ore achieved a top feed size of -19/+16 mm and 103.3 kg was the total mass of the crushed ore. *Table 3.2* illustrates the weighted mass of each sieve size categorized into nine (9) class fractions as -19/+16 mm, -16/+11.2mm, -11.2/+8 mm, -8/+5.6 mm, -5.6/+4 mm, -4/+2.8 mm, -2.8/+2 mm, -2/+1 mm and < 1 mm. In this study, all ore particles below -1 mm were considered as fines. The classified fractions of ore were weighed and piles were stored in 25 L plastic buckets for further use in all the investigations covered in this study.

3.2.3 *Ore Grade Analysis*

Each crushed and screened size fraction was split to obtain representative samples for head grade analysis. A riffler was used in the splitting of the -19/+16 mm size fraction; while a ten (10) cup rotary splitter was utilized for the other eight (8) size fractions. 300 g of each class was obtained as the representative sample after initial splitting. Further preparation of pulverizing and splitting was done to achieve the final representative sample for the assay-by-size to obtain the head grade of each crushed particle fraction. Assay-by-size was performed with the MARS 6 iWave digestion unit, Analytical lab, UCT. Digestion of samples was performed with 8 ml of nitric acid (HNO_3) and 2 ml hydrofluoric acid (HF); and neutralized in 20 ml boric acid. The assay-by-size for all representative samples were performed in triplicates. Result of the grade analysis is presented in *Table 3.2*. Bulk ore assay was also achieved using the aforementioned method. This was performed in order to authenticate the homogeneous grade of the ore. The theoretical head grade for the bulk ore obtained from the production of the batches was calculated to be ~ 0.0581 wt%. The overall head grade assay obtained was 0.0511 wt%. Both assay and theoretical values were in close proximity with a relative variation of 0.35%.

Table 3.2: Synthetic silver ore crushed weight and grade distributions

Size Fractions (mm)	Ore (kg)	Ag. Grade (wt%)	Ag. Total (g)
-19/+16	10.662	0.05	5.331
-16/+11.2	21.413	0.05	10.706
-11.2/+8	13.782	0.05	6.891
-8/+5.6	18.847	0.05	9.423
-5.6/+4	7.186	0.05	3.593
-4/+2.8	5.243	0.05	2.622
-2.8/+2	4.215	0.06	2.529
-2/+1	5.995	0.05	2.997
-1	15.982	0.05	7.991
Total	**103.323**	**0.0511**	**52.083**

3.3 Chemical Lixiviant

Two reagents were utilized throughout this investigation. Potassium (K^+) in Potassium Nitrate (KNO_3) and Sodium Cyanide (NaCN) were used as nonreactive tracer and reactive leaching lixiviant chemicals respectively. The characterization of individual particle fractions was leached with sodium cyanide solution at varying conditions to determine the leaching kinetics. The concentration levels of potassium and sodium cyanide used throughout this study was 1 g/L K^+ and 50, 275, 500 mg/L NaCN.

Working with cyanide poses safety concerns requiring a specific pH operating condition. Alkaline sodium salts were used in the studied as a buffer to maintain the pH at 10~11 and prevent the hydrolysis of free cyanide ions to produce toxic HCN gas. The pH of all experiments in this work stayed relatively constant at about pH 11~12.5. Buffer chemicals to achieve alkalinity of solutions were sodium carbonate (Na_2CO_3) and sodium bicarbonate ($NaHCO_3$). The alkaline solutions contained the concentration of 9.3 g/L and 1 g/L for sodium carbonate (Na_2CO_3) and sodium bicarbonate ($NaHCO_3$) respectively. All solution pH was measured with the use of Crison Basic pH meter. Deionized water at basic conditions was used throughout this investigation except otherwise stated. With the use of sodium cyanide as the major leaching lixiviant which suggest constant contact with the reagent, Safety, Health, and Environmental (SHE) working and waste disposal procedures were straightly adhered to and are provided in ***Appendix I***.

3.4 Leaching Procedures

The artificial ore kinetics of reaction studies were achieved utilizing two different methods including Shake flask (SF) leaching and circulating fluidize fixed bed reactor (CF-FBR) leaching. Pure silver metal leaching was investigated as well to determine the maximum extraction rates at varying experimental conditions.

3.4.1 *Batch Shake Flask Leaching*

The reaction kinetics was achieved by cyanide leaching performed using a matrix of shake flask tests. The concentration of cyanide solution, temperature, and particle size of the ore was varied to obtain key kinetic information such as the rate constant, the reaction order, and the activation energy of the ore. The flask tests were performed using 300 g of ore in 600 ml lixiviant solution (1:2 solid-liquid ratio). The duration of each experiment was about ~8.5 days. The experimental sequences are depicted in *Table 3.3* and *Figure 3.2* illustrates the setup.

Table 3.3 Parameters for Shake Flask leaching studies

Test Conditions	Run 1			Run 2			Run 3			Run 4
T (°C)	25*			48			60			25*
NaCN (mg/L)	50	275	500	50	275	500	50	275	500	275
Particle Size (mm)	-16/+11.2; -8/+5.6; -2/+1**									-19/+16; -11.2/+8; -5.6/+4; -4/+2.8; -2.8/+2; -1
Sampling Intervals (mins)	5, 15, 30, 30, 45, 60, 120, 180, 360, 540, 720, 1440, 2880, 5760									

*During the experiment, the temperature varied between 25 °C and 28 °C.

** -2/+1 mm experiment was not conducted at 60 °C.

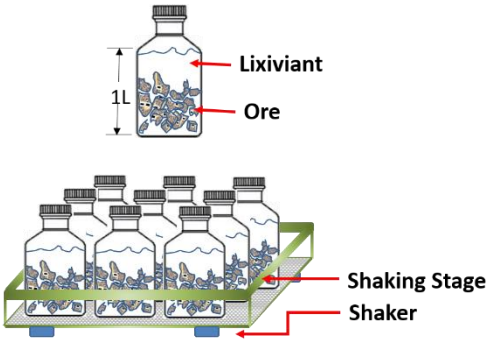

Figure 3.2 Schematic of the shake flask experimental setup where the ratio of solid-liquid was 1:2.

An amount of 14 samples (10 ml each) was collected over a period of sampling interval for each run condition. After achieving an optimum sodium cyanide concentration (275 mg/L) at the lowest temperature (25 °C) for the first 3 runs of the selected particles, the rest of the experiments for the remaining size fractions (run 4) and subsequent experiments including the circulating fluidized fixed bed reactor (CF-FBR) and reactive leaching were operated at those conditions.

3.4.1.1 *Pure Silver Metal Leaching*

The pure silver metal grains leaching experiments were quite similar to the coarse particle leaching. This experiment was performed in order to establish a standard for comparing the extraction from the coarse artificial ore. The experiments were conducted for a duration of ~ 59 hours. For the determination of the initial dissolution rate, additional 2 repeats of the experiment were performed over a period of ~3 hours. Detailed parameters are presented in *Table 3.4*. An amount of 200 mg of pure silver powder was leached in 200 ml sodium cyanide solution at varying temperature and reagent concentration conditions. At every sampling, a 0.22-micron reg cellulose syringe filter was used to filter the samples before analysis.

Table 3.4 Pure silver leaching parameters

Test Conditions	Run 1			Run 2			Run 3		
T (°C)	25*			45			60		
NaCN (mg/l)	50	275	500	50	275	500	50	275	500
Pure Silver Metal (mg)	200			200			200		
Sampling Intervals (mins)	5, 15, 30, 30, 45, 60, 120, 180, 360, 540, 720, 1440								

*During the experiment, the temperature varied between 25 °C and 28 °C.

3.4.1.1.1 Batch Stirred Reactor Leaching

The shake flask tests of both pure silver metal and coarse synthetic silver ore were performed with the use of conical flasks and Schott bottles respectively in the Labotec Inco Shaker and Labcon Shaking incubators interchangeably. Shaking settings were constant at 90 RPM, while temperature settings were adjusted according to each experimental parameter.

A separate diagnostic leaching test work was performed on the pure silver to validate the initial dissolution rate obtained from the shaking incubator experiments. The duration of the test was ~3 hours at similar conditions according to *Table 3.4*. The only difference was the setup. This experiment utilized 3 separate jacketed batch reactors agitated with magnetic stirrers at a speed of 700 RPM *Figure 3.3*. Temperatures were regulated with circulating water baths.

Samples extracted from the batch leaching of both pure silver and the coarse synthetic particles were analysed for dissolved silver concentration using inductively coupled plasma optical emission spectrometry (ICP-OES) and inductively coupled plasma mass spectrometry (ICP-MS) techniques. All ICP-OES and ICP-MS analyses were performed at the Chemical Engineering Department Main Analytical laboratory, UCT and the Central Analytical Facilities at the University of Stellenbosch, respectively.

Figure 3.3 Batch stirred reactor setup. ~3 hours of run at varying temperatures (25 °C, 48 °C, & 60 °C) and concentration (50, 275, 500 mg/L) dissolving 200 mg silver in each reactor.

3.4.2 ***Circulating Fluidized Fixed Bed Column Reactor Leaching***

The use of a circulating fluidized fixed-bed column reactor was another leaching approach implemented during this investigation to study the leaching kinetics in the coarse synthetic silver ores. In principle, the device operates in continuous mode where lixiviant solution and air are both pumped upward through the

reactor. The down-flow circulates through the fully immersed fixed-bed of ores stack in baskets (*Figure 3.4* and *Figure 3.5*). The air was bubbled from the bottom through a central shaft tube to create an updraft in order to keep the volume of solution in continuous recirculation throughout the duration of the experiment. As depicted in *Figure 3.5*, air reaching the top of the reactor escaped through a gas outlet opening. As the solution circulates through the reactor, the metal grains are leached into the solution and recovered from the lixiviant outlet stream at the top side of the reactor.

The circulating reactor rig contains four columns each with an operational volume of 7 L. The leaching experiments were performed on selected crushed ore particles from four class fractions (-19/+16 mm), (-16/+11.2 mm), (-8/+5.6 mm), and (-4/+2.8 mm). The (-4/+2.8 mm) size class was used as the minimum size in this experiment because the aperture of the baskets in the reactor was wider for all the other fractions below this fraction.

Figure 3.4 CF-FBR rig setup according to the flow diagram in figure 3.5. 7L of reactor volume run at 50 ml/hr flowrate, 25 °C and 275 mg/l NaCN.

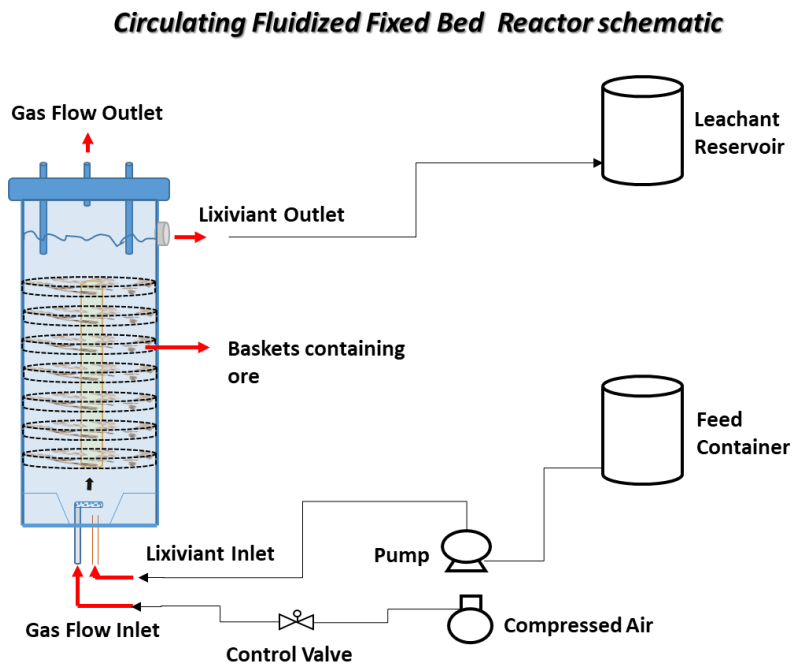

Figure 3.5 CF-FBR column reactor flow diagram

Conditions of the reactors were set and monitored at 25 °C temperature and 275 ppm NaCN while the air was bubbled at 2700 mL/min (0.27 vvm). The system was operated in continuous mode with a throughput flow rate of 50 ml/hr (2.83 L/m²/hr). The duration of the experiment was about ~17 days. Intermittent stops were observed for sampling after 0.5, 1, 2, 3, 6, 9, 12, 24, 48, 96, and 192 hours of leaching. The periodic stoppage was done in order to conduct 3D μX-ray CT scan on a number of selected particles of the four class fractions being leached (*see section 3.5.2*). The CF-FBR leaching experiments were performed in the organic chemistry lab facilities at the South African Nuclear Energy Corporation (Necsa) where the micro-focus X-ray scans were acquired.

At every sampling interval, liquid samples were extracted from the effluent stream of the reactor as depicted in *Figure 3.4*. The effluent volume at every sampling interval was measured and disposed of into waste containers. During the period of effluent sampling, the reactors were stopped and the loaded baskets containing the ores were lifted out, drained, submerged into deionized water for a rinse, and let alone in the fume hood. Rinsing was performed to wash out cyanide from the surface of the ores in order to occlude reaction until the 3D scan was completed to begin the next interval of the experimental run at which time the baskets were resubmerged in the reactors. During the stoppage, the cyanide leaching solution in the reactor was kept standing until the operation resumed.

About 300 g of feed material from each size fraction according to batch shake flask experiment feed was loaded in the reactors. It must be noted that the reactor has the capacity to take more samples; however, the selection of the loaded material was deliberate. Extraction data received from ICP-OES assay of the liquid effluent was compared with results from the batch leaching studies and used to predict the leaching potential of the synthetic ore for the column RTD investigation.

3.5 Ore Characterization

3.5.1 ***Pore Characterization***

Pore volume experiments were performed in order to determine how porous the coarse synthetic particles were to aid the advancement of lixiviant ingress on metal dissolution into solution. Water Absorption Measurement (WAM) and MicroX-ray Computed Tomography scan analysis are two methods that were used to obtain pore volume data for the crushed coarse fractions. Both experimental techniques were performed on four selected classes according to the CF-FBR leaching experiments.

3.5.1.1 *Water Absorption Measurements (WAM)*

Water absorption porosity measurements were conducted by analysing the amount of water absorbed by different particle size fractions over specific time intervals (i.e. periodically over ~17 days). Dry pre-weighed samples were immersed in a known volume of water for measured time intervals. An estimate of the penetration rate of water was obtained from the mass of water absorbed and the period of immersion. Porosity was determined by calculating the ratio of water absorbed by the mass of the difference of dry to wetted/saturated sample by the final mass of the wetted sample.

To determine accurately the mass of water absorbed inside the pores and not the water on the surface of the samples, drying the ore surface while maintaining the moisture inside the particles was critical. To achieve this, air was blown by a fan on the surface of the samples until they appeared dry exhibiting a grey coloured surface. Since some internal moisture could have been lost during the drying process, the porosities obtained were considered minimum values. The WAM method was performed in triplicates in order to obtain confidence in the results.

Because the XCT investigation was based on the CF-FBR sampling schedule, the pore adsorption experimental sampling interval was also aligned after such schedule and duration. Approximately ~150 g of each selected crushed fractions was submerged in 200 ml of deionized water over a period of 0.5, 1, 2, 3, 6, 9, 12, 24, 48, 96, and 192 hours amounting to ~17 days (*see Figure 3.6*).

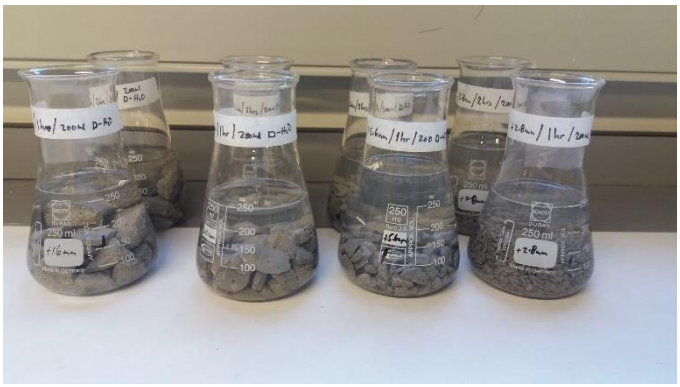

Figure 3.6 Pore absorption experiments on four select size fraction using 200 ml D-H_2O and 150 g of ore material.
(-19/+16 mm), (-16/+11.2 mm), (-8/+5.6 mm), and (-4/+2.8 mm)

3.5.2 ***Micro-XCT Characterization***

Micro-focus 3D characterization of volume percent porosity including crack/fissure network, silver grains size, grains dissemination, and grade distribution in each selected size fraction was studied before, during, and after the course of the full CF-FBR leach experiments. All 3D scans were achieved by utilizing the NIKON XTH 225 ST Micro X-ray computed tomography equipment in the MIXRAD facility at the South African Nuclear Energy Corporation (Necsa).

As mentioned, the CF-FBRs were stopped from time to time to run scans on selected particles with the aim of investigating the progress of leaching in each particle fraction. Parameters and scan conditions at both low and high resolutions used in the study are presented in *Table 3.5*. Scans obtained from XCT was analysed using the VGStudio Max 3.2.4 software package.

Table 3.5 X-Ray CT measurement parameters

Voxel Size (Resolution)	**~ 20 µm**	**~ 4.8 µm**
Number of Projections	1000	1000
X-ray energy	130 kV	130 kV
Beam Current	110 uA	37 uA
Radiation Filter	0.25 mm Cu	0.25 mm Cu
Scan Duration	30 mins	60 mins

Size (mm)	-19/+16	-16/+11.2	-8/+5.6	-4/+2.8
# of Particles	21	21	59	356
Sample Picture				

Figure 3.7 Selected class fraction and number of particles analysed for the determination of the synthetic ore grade distribution.

About 2~3 particles were analysed from each class for the pore volume analysis, while more particles according to *Figure 3.7* were utilized in determining the silver grain distribution and XCT grade analysis.

3.5.2.1 *Sample Prep and Data Extraction*

During the intermittent stops of the reactor leaching system, the selected particles were loaded unto polyester foams for the scan. The orientation of the particles was kept constant during each scan in order to maintain and keep track of grain dissolution (*see Figure 3.8a*).

When a scan is conducted on an object, X-ray images are usually 2D radiography projections. The development of these 2D shadows into the virtual 3D volume is achieved in the reconstruction process. After every periodic sampling and scanning, radiographs obtained from raw scans were reconstructed using the CT Pro software package. A reconstructed 3D volume file of the stack sample of *figure 3.8a* is shown in *Figure 3.8b*.

3.5.2.2 *Processing & Analysis*

Reconstructed radiographs were processed and analysed utilizing VGStudio Max 3.2.4 software package to visualize the internal structure of particles for assessing the following parameters including metal grain detection and dispersion, pore volume percent, and grade distribution.

The processing of images required the extraction of individual ore particle from the full stack of particles scanned (as shown in *Figure 3.8b*) prior to analysing for the aforementioned XCT characterization objectives. This was achieved by identifying individual particles with the navigation cursor follow by selecting a region of interest (ROI) using the region growing tool. It must be noted that defining the surface boundaries is very important with respect to subsequent pore analysis. The selected ROI on an individual particle may influence the downstream result by either exaggerating the number of pores at the surface of

a

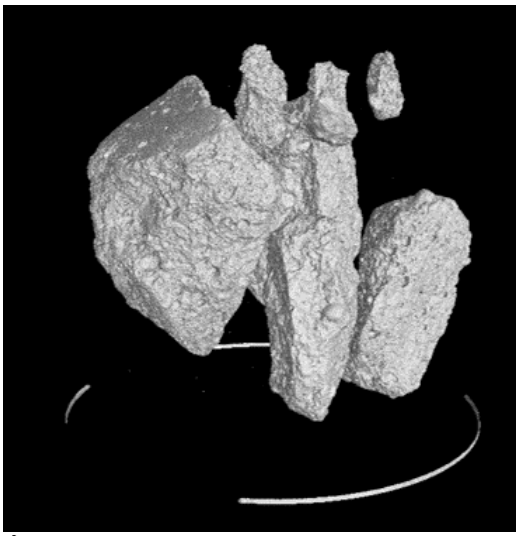

b

Figure 3.8 (a) Stack of selected ore particles before scan; [front stack] up, 2.8 mm, down 5.6 mm, [back stack] 11. 2mm and (b) full stack after reconstruction of radiograph.

the particles or it may exclude existing pores. Therefore, errors associated with determining surface boundaries of particles was avoided with careful use of the erode/dilate and open/close tools.

After successful extraction of particles from scanned stacks, pore volume and silver metal grain quantification data were obtained by utilizing the defect analysis and the grey value analyser (GVA) tools. Applying defect analysis for the quantification of pores required the largest pore in a particle to be selected and analysed using GVA to determine the grey value of the deepest pore voxel. The determined grey value was used as the threshold value for the maximum void. The maximum void value was further toggled until all visible small and residual pores were filled prior to initiating the defects analysis.

The analysis of metal grains extraction was similar to the pore volume; however, instead of obtaining value for the maximum void, VGStudio considered the grains as inclusions. Thus, the minimum grey value of brightest grain (inclusion) and grey value of the second dense phase (most likely impurities; *section 4.3.3*) in

the particle-matrix were individually quantified using the GVA tool. Grey values of both phases were calculated by applying the principles of partial volume effect (*Nwaila, 2014*) to obtain the minimum inclusion value of the metal grain. Prior to applying the final step of defect analysis for grains quantification, the rendering tool was used to authenticate that the selection of the targeted grains was effective and the second dense material (gangues) was not captured into the silver defect analysis.

3.5.3 *QEMSCAN*

Quantitative Evaluation of Materials by Scanning Electron Microscopy (QEMSCAN) data processing was integral in determining the modal bulk mineralogy of the synthetic ore matrix. The FEG QEMSCAN using an FEI Quanta 600F scanning electron microscope platform and Bruker detectors located at the University of Cape Town was utilized in this investigation. The equipment settings are detailed in *table 3.6*. While no other mineral composition amendable to leaching with NaCN was used in the production of the ideal homogeneous ore, the QEMSCAN 2D technique was employed in order to validate the synthetic ore bulk mineralogy for the X-ray analysis; it may be recalled that sand and cement were two other components that made up the ore matrix.

Table 3.6 QEMSCAN measurement settings

Measurement mode	Particle Mineral Analysis (PMA)
Field size	2000 µm
Magnification	102X
Point spacing / pixel size	4 µm
Beam current	10 nA
High Voltage	25 kV

Samples of the sand (used in production) and -4/+2.8 mm were split to the right quantities and sent for prep and bulk mineralogical analysis with QEMSCAN. Parameters conditions use for obtaining the scan is provided in *table 3.6*.

3.6 Column Leaching Equipment & Procedures

The residence time investigation of reagent flow through the column was determined by two mechanisms, the approach using a conventional inert tracer method and an innovative reactive leaching approach. The reaction method was conducted to elucidate flow performance based on the maximum extraction from the ore. Chemical analysis of the effluent stream samples was used to evaluate the amount of the solid reactant species that was dissolved over the residing fluid percolation time through the column bed.

Laboratory column reactors were used for the research investigation of the residence time fluid percolation studies. The columns had dimensions of 0.53 m height and diameter 0.093 m with a capacity of 3 kg. A plexiglas perforated plate was fitted to the column bottom and glass beads were used as the packing material at both the bottom and top of the reactor. Glass beads at the top of the columns served the purpose of distributing fed solution to the bed. Glass wool was placed between the perforated plate and the glass beads to capture any fine material that may have penetrated the layer of glass beads. A peristaltic pump was used to supply lixiviant solution at the column inlet (top) from the feed reservoir, while the pregnant leach solution was obtained from the column exit stream. The reactor was jacketed with a heating coil connected to a thermostat that regulated the temperature. From time to time, the regulator box malfunctioned and was not stable. Fortunately, all column experiments were conducted at room temperature so this was not a major challenge. Detail schematic and diagram of the column is presented in *Figure 3.9* and *Figure 3.10*.

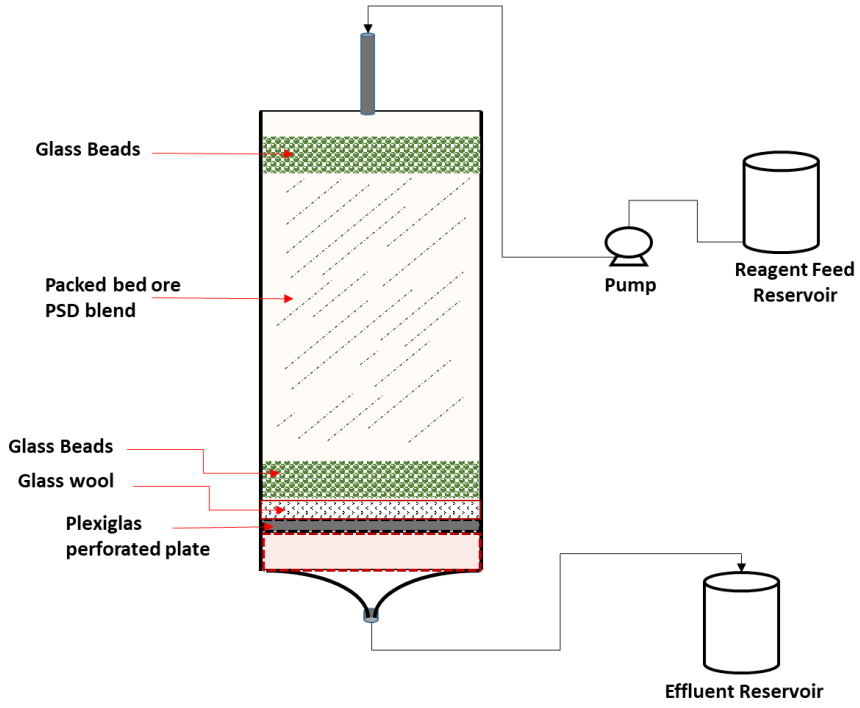

Figure 3.9 Detail schematic of RTD column reactor

Figure 3.10 Laboratory RTD column reactors setup

Optimum experimentally observed parameters from the kinetics investigation were employed to the RTD column experiments. Temperature conditions for the column study were kept constant at room conditions (~ 25 °C), and reagent concentration was kept constant at 275 mg/L in pH 10~11 alkaline solution. The extraction performance was ultimately monitored in the effluent stream through chemical solution assays using ICP-OES; while inert tracer K^+ was analysed by atomic absorption spectroscopy (AAS) at the Analytical Lab, UCT. The RTD experiment procedure is summarized in *Table 3.7*. Each column configuration RTD experiment lasted for 24 days (12 days each for both nonreactive tracer and reactive leaching studies).

3.6.1 *Column Irrigation*

Considering reactor flow rate as a parameter of investigation in this study, irrigation rates were kept constant at 2 L/day, 1 L/day and 0.5 L/day in specific experiments according to *Table 3.7* while relating the effect of leaching to the different blending ratios of particles (*section 3.6.3*). Reagent solutions were delivered to the reactor beds through single drip emitters. To improve solution distribution, glass marble beads used on top of the bed were underlain with a flat thin layer of tissue/cotton just above the ore. 10 ml routine samples were collected 3 times daily from the drained effluent reservoir and the total volume per sampling interval was measured. For all experiments with an exception of the consolidated test, nonreactive tracer RTD preceded the reactive leaching investigations.

The RTD studies used the inflow step-change tracer response technique. For the inert RTD tests, the solution was pumped from the feed reservoir until the maximum concentration of the feed was attained in

the effluent solution; then the pump was switched to deionized water for the step-down. After the step-down leaching duration, the pump was immediately switched to the alkaline NaCN feed reservoir.

Table 3.7 All RTD experimental conditions at constant room temperature.

Column	PSD coefficient	Irrigation Flow Rate ($L/m^2/h$)	NaCN/K^+ Concentration (mg/L)
YT1	0.721	12.27	275/1000
YT2	0.721	6.13	275/1000
YT3	0.721	3.06	275/1000
YT4	0.25	6.13	275/1000
YT5	1.0	6.13	275/1000
YT8*	0.721	6.13	Mixed reagents (NaCN & KNO_3)

*Consolidated experiment.

3.6.2 *Peristatic Pump*

Throughout the study, both investigations including the circulating fluidized fixed bed reactor leaching characterization and RTD studies utilized a MasterFlex Peristaltic pump to supply fresh lixiviant solutions from feed reservoirs to the respective reactors. Calibration for the CF-FBR was 4.166 ml/ 5 mins to obtain a flow rate of 50 ml/hr. The pump was switched on and ~ 4.166 ml deionized water was measured for every 5 mins followed by readjustment of settings until the desired flow rate was obtained. For the RTD columns calibrations, 6.95 ml, 3.5 ml, and 1.75 ml were measured in marked sample bottles for 5 mins each to obtained desired flow rates of 2, 1, and 0.5 L/day respectively. The flow rate was monitored daily and recalibrated in order to achieve steady accurate operation. Operating at lower flowrates (0.5 L/day) was problematic, requiring daily recalibration; while higher flow rates did not seem to create problems. The MasterFlex cartridge tubing was changed after every other week during maintenance and the pump was recalibrated.

3.6.3 *Particle Size and Blending Distribution*

The synthetic silver ore utilized in the RTD column investigation and throughout this study was prepared as described in *section 3.2.1*. After successful preparation of crushing, sieving, and weighing for each size, distribution of the ore fractions was obtained (*Table 3.8*). The Gates-Gaudin-Schumann (GGS) particle size distribution (*Eq. 3.1*)was applied to the weighted particle size distribution.

$$Mp = 100 * \left(\frac{x}{J}\right)^{m} \qquad \textit{Eq. 3.1}$$

where *Mp*, represents the mass passing of a class fraction, *x*, is the size or the average size of the particle class fraction, *J*, is the maximum passing size in the total mass (when *Mp = 100*), and *m*, is the distribution coefficient. The GGS equation best fitted the plot of sieve analysis from the weighted crushed ore and was well situated in the optimum range of heap feed particle distribution (*Bartlett, 2013*). *Figure 3.11* demonstrates the best fit considered as the "*true*" blend distribution coefficient (BDC) for the synthetic ore.

Table 3.8 Synthetic silver ore particle size distribution

Fraction Size (mm)	Retained (%)	Cumulative Retained (%)	Cumulative Passing (%)
+ 19	0	0	100
+ 16	10.319	10.319	89.681
+ 11.2	20.724	31.043	68.957
+ 8	13.338	44.381	55.619
+ 5.6	18.240	62.621	37.379
+ 4	6.955	69.576	30.424
+ 2.8	5.074	74.651	25.349
+ 2	4.080	78.730	21.270
+ 1	5.802	84.532	15.468
- 1	15.468	100.00	0.000
Total	**100**		

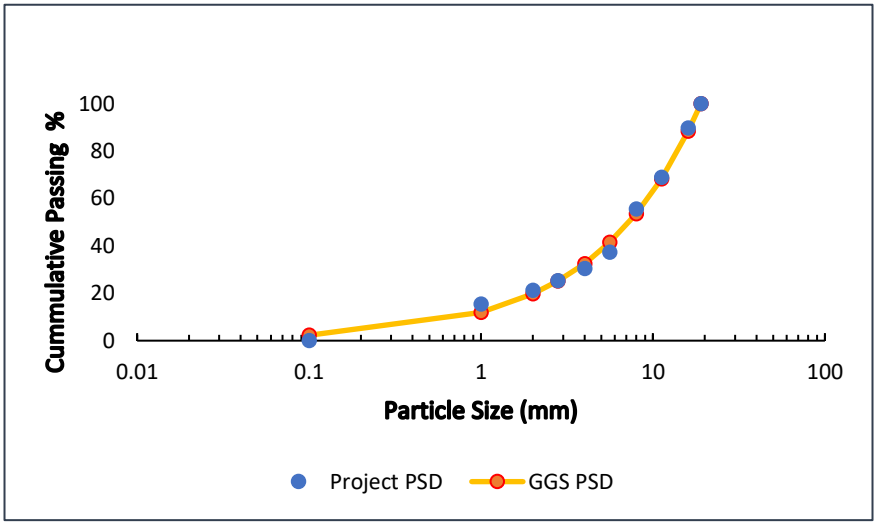

Figure 3.11 PSD of crushed size synthetic silver ore fitted to the Gates-Gaudin-Schumann distribution model.

The figure shows that the distribution of particles prepared had similar distributions within marginally acceptable variance with the correlation of the GGS model. The *m* value obtained for the crushed synthetic silver ore was 0.721. The parameter *m* was fitted by the sum of square error minimization with the used of MS-Excel Solver tool. All data presented were obtained directly from sieving and not interpolation except otherwise stated; as in the case of determining the d_{80} passing. For the investigation of varying the effect of column bed PSD on RTD, an additional 3 artificial blending distribution coefficients (BDCs) using the GGS model were developed. The BDCs were 0.25, 0.5 and 1.0 aside from 0.721 that was the original/true PSD of the crushed ore. Each column investigation was characterized with 3.0 kg of ore material. The weighted PSD developed for all the BDCs relative to the column capacity are provided in ***Appendix II***.

The d_{80} of the crushed feed describes the size fraction of particle diameter which 80 % undersize of the bulk feed mass passed the sieve. It was observed that as the particle distribution coefficient shifts from higher to lower values, the d_{80} of the GGS also shifts to smaller size fraction (*Figure 3.12*). This is indicative of a larger proportion of fines reporting to the bulk particle feed. The values of d_{80} at changing coefficient used in this investigation were obtained by interpolation and is presented in ***Appendix II***.

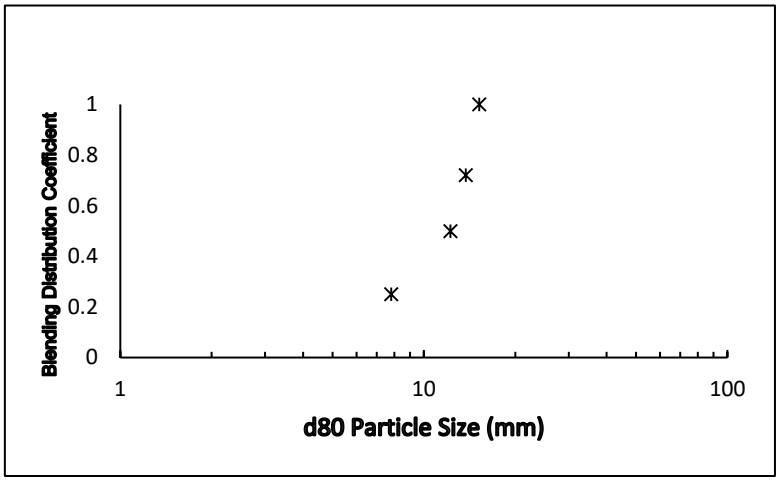

Figure 3.12 Plot of distribution coefficient vs d80 value obtained from crushed synthetic silver ore.

3.6.4 *Flooding and Rinsing*

It was observed in preliminary test work that the artificial silver ore contained significantly high background concentration (1~2 g/l) of potassium, sufficient to offset the concentration conditions used in the RTD investigation. Hence, all RTD columns were flooded and drained continuously for about 7~10 days with tap water at a flow rate of 14.5 ml/min. A Mettler Toledo Seven Compact S230 conductivity meter was used to monitor each sequence of flood and drain effluent volume. This process was carried out until the effluent solution conductivity had dropped to a similar measurements as that of the tap water (0.075 ~

0.15 mS/cm). The last effluent volume from flooding before the RTD was analysed with AAS for K^+ . At this point, samples result showed that the potassium concentration had dropped in the range of 1.54 ~ 54 mg/L for all the columns after the final rinse. Finally, the reactors were left alone to drain for 2 days before commencing the RTD investigations.

3.6.5 *Column Loading*

Because all the columns were washed down thoroughly before each RTD test, no agglomeration was performed before loading the columns with ore feed. The packing mechanism of the column considered a thorough mix of the blend prior to column loading in order to avoid segregation of the size fraction. Ore weight measured according to the GGS coefficient was dry mixed in a closed 20 L bucket, left alone for the dust to settle, and then gently loaded in the reactor. Each column investigation was characterized with 3.0 kg of ore material.

4 μX-RAY COMPUTED TOMOGRAPHY CHARACTERIZATION OF ARTIFICIAL SILVER ORE

4.1 Introduction

Characterization of the artificial silver ore for the validity of its ideal properties using X-ray computed tomography is presented in this chapter. Micro-focus material characterization was performed on selected crushed ore particles from four class fractions, including (-19/+16 mm), (-16/+11.2 mm), (-8/+5.6 mm), and (-4/+2.8 mm) utilizing the NIKON Micro X-ray computed tomography MIXRAD system at the South African Nuclear Energy Corporation (Necsa).

The critical objectives for the production of the synthetic ore included attaining homogeneity in the composition and distribution of silver grains, a homogeneously porous ore matrix, which contains no reactive gangue minerals to interfere with the silver dissolution and a well-distributed, uniform metal grain size within the gangue matrix. The micro-XCT technique evaluates the ore in terms of these parameters for metal grain detection and dispersion throughout the ore particle; as well as pore volume percent and cracks network distribution quantified for total particle voidage. Validation of mineral dispersion and bulk mineralogy of the artificial ore was achieved with the use of traditional 2D QEMSCAN technique. Parameters for both XCT and QEMSCAN are provided in *section 3.5.2*.

4.2 Particle Voidage

The volume of a particle that is not occupied by a mineral or gangue phase but creates hollow spaces in the particle is considered a void. Voids categorized in the context of large particle characterization constitutes internal pores, usually naturally occurring during rock formation (*Negron et al., 2016*), and most often cracks/fractures induced by comminution methods (*Ghorbani et al., 2013*). These voids can provide conduits through which metals embedded in the inner subsurface of particles are dissolved and extracted during heap leaching, thus making them available for leaching. The voidage of the particle, therefore, includes available pores and crack/fracture networks. The porosity of the synthetic silver ore was evaluated using both Micro XCT and water absorption techniques.

4.2.1 ***XCT Porosity***

4.2.1.1 *Pores*

The porosity of the synthetic ore obtained using micro-XCT was accomplished by identifying the darkest regions in the pores and the very light dense material/gangue that was next to the darkest phase. This was achieved with the partial volume effect approach. It can be noted that the production of artificial ore played an important role in inducing the ore particle porosity. Care was taken in order to avoid the ore being overly compact so that it becomes less porous, or excessively porous, and thus loses the similarity to natural ore. *Figure 4.1* illustrates the porous nature of the particles scanned, while *Figure 4.2* demonstrates the porosity of individual class fractions and overall average porosity.

The colour bar in *figure 4.1*shows the extent of pore volume in the synthetic ore. The capacity of these pores varied in different fractions among particles. The largest pore was observed to be in a range of about 2.8 ~ 3.4 mm^3; at the resolution of 20 microns, the images revealed that pores were not visibly interconnected. The appearance of pores spontaneously occurring is attributed to the presence of trapped air bubble during the manufacturing of the material. A laboratory vibrator table was utilized in a preliminary study (*Gani & Manzila, 2018*); however, it had the propensity to induce settling of the silver grains to the bottom of the lumps; hence, vibration moulding was avoided subsequently in the project ore production stages.

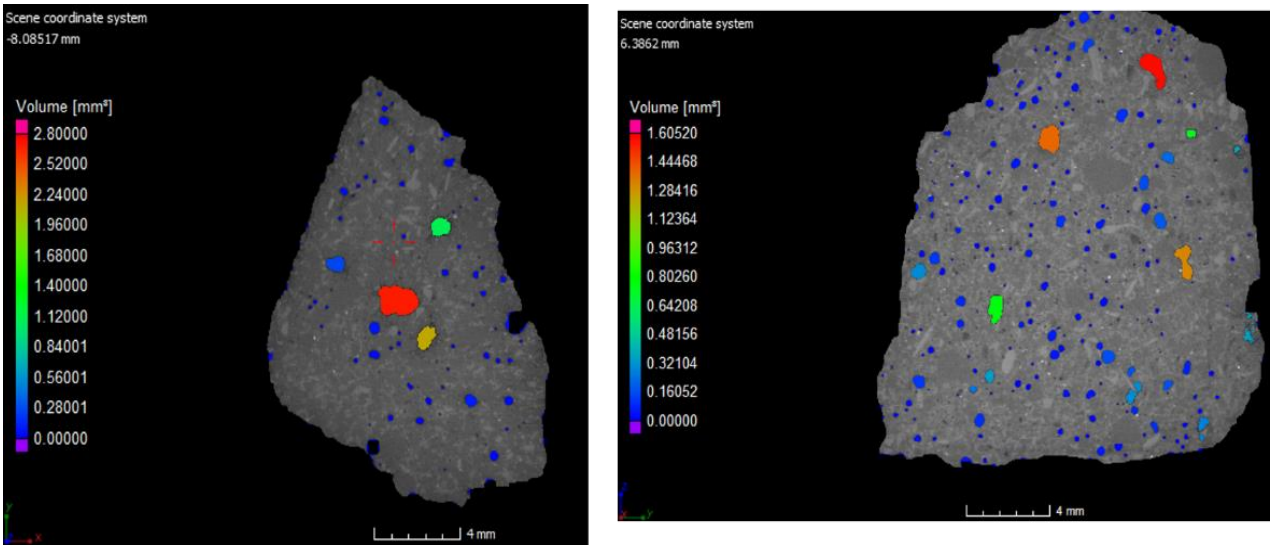

Figure 4.1 XCT pore volume map of -19/+16 mm particle left (top view) and -16/+11.2 mm particle right (right view).

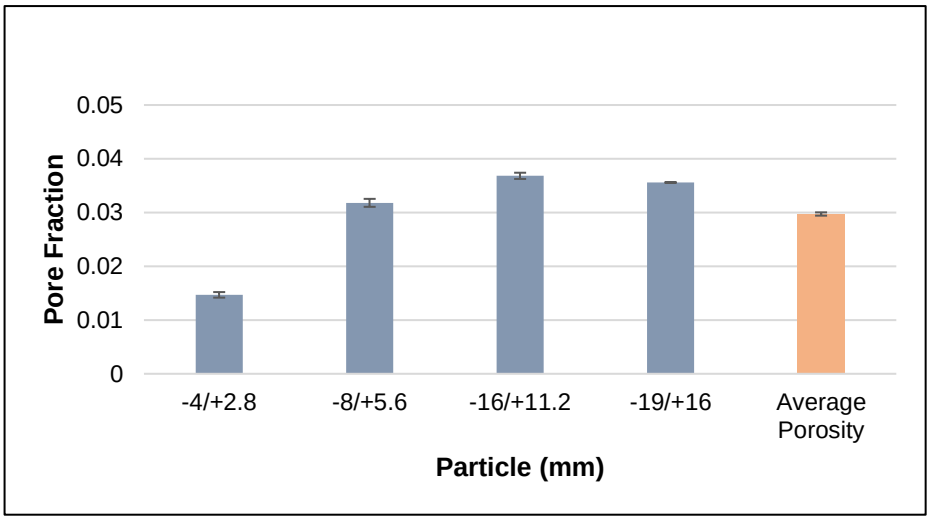

Figure 4.2 XCT porosity of selected particles of the synthetic silver ore before the leaching experiment at 20 μm resolution.

Figure 4.2 demonstrates that the porosities of the individual selected particles increase with an increase in particle size up to the -16/+11.2 mm fraction; but the -19/+16 mm fraction did not experience similar trend as the data shows lower porosity than the -16/+11.2 mm fraction. The overall average porosity of the synthetic ore was ~ 2.97%.

4.2.1.2 *Fracture/Crack Network*

In the quantification of the synthetic silver ore with XCT, no definite network structure of cracks/fractures were captured in the 3D mapping of the ore voidage (*Figure 4.3*); probably due to the scan resolution. Some slices of the ore showed visible crack structures; however, these fissures could not be quantified (*Figure 4.4*).

Quantifying visible cracks below the XCT scanned resolution (20 μm) was challenging as it was considered below the detection limit. Furthermore, applying defect during the imaging analysis, the maximum void threshold below the partial volume analysed would result in exaggeration of the particle porosity. *Ghorbani, et al., (2011, 2013)* encountered a similar challenge in investigations on zinc sulphide ores scanned at 15 ~ 20 μm resolution.

Sphericity data obtained from the XCT defect analysis was used to verify the voids of scanned particles attempting to quantify cracks/fissures. Sphericity is the ratio of particles/voids volume to the surface area usually on the scale from 0 - 1. Highly spherical particle/void will exhibit a sphericity > 0.81 approaching 1 (perfect sphere); while lower sphericity suggests cavities that are cylindrical or elongated approaching 0 which indicate no volume. *Figure 4.5* demonstrates that a large proportion of voids in the ore were about the average sphericity of 0.66 ~ 0.7. This suggests that a third of the pores are fairly spherical. Some very

spherical pore exist but the majority of the pores were not that spherical. Voids constituting pores defined by the quantified sphericity were much more pronounced compared to the presence of cracks/fractures. Should the presence of cracks had been prevalent in *Figure 4.5*, it would have resulted in data shifting to the left; however, the data showed a left-skewed normal distribution about 0.66 indicative of semi-rounded spheres. These pore structures are visibly evident in *Figure 4.4*. Void sphericity graphs of the other selected particles showing a very similar trend are provided in ***Appendix III.a***.

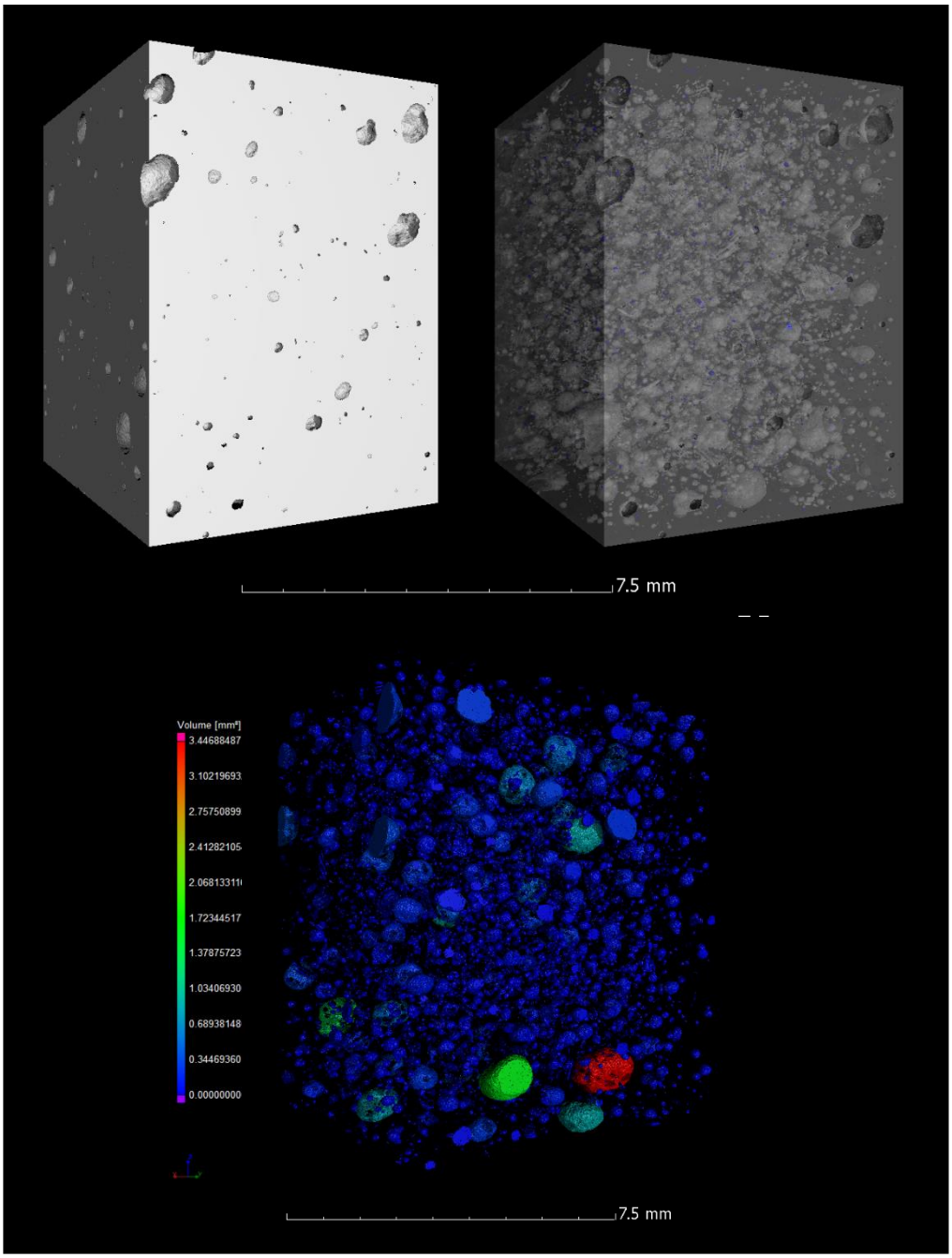

Figure 4.3 3D slice cross section of the synthetic ore showing non-continuous porosity of the material from the outer matrix through the internal structure of the material (top to bottom).

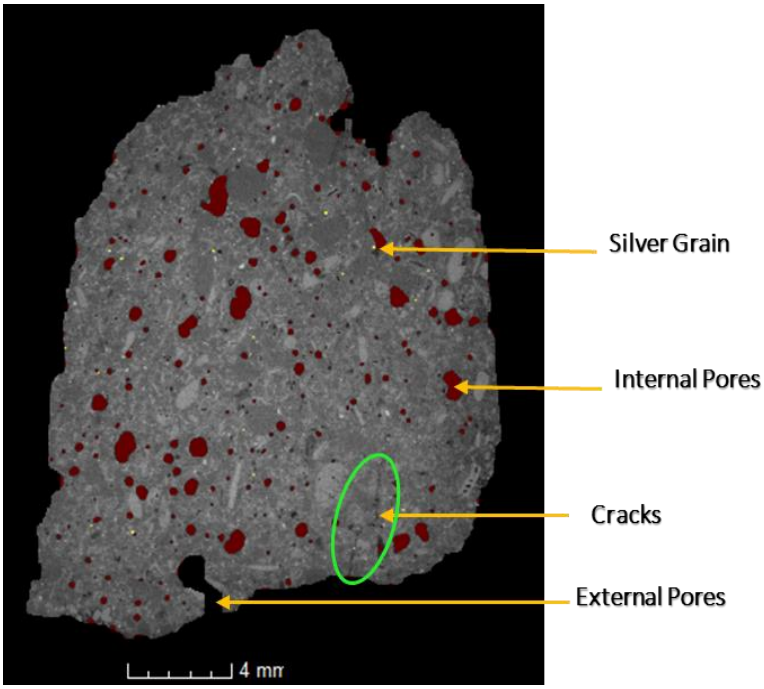

Figure 4.4 XCT defect analysis of 11.2 mm particle showing the presence of pores opening to the surface of the particle (external pore), internal pores showing substantial roundness without network, and cracks observed to be below detection threshold for quantification.

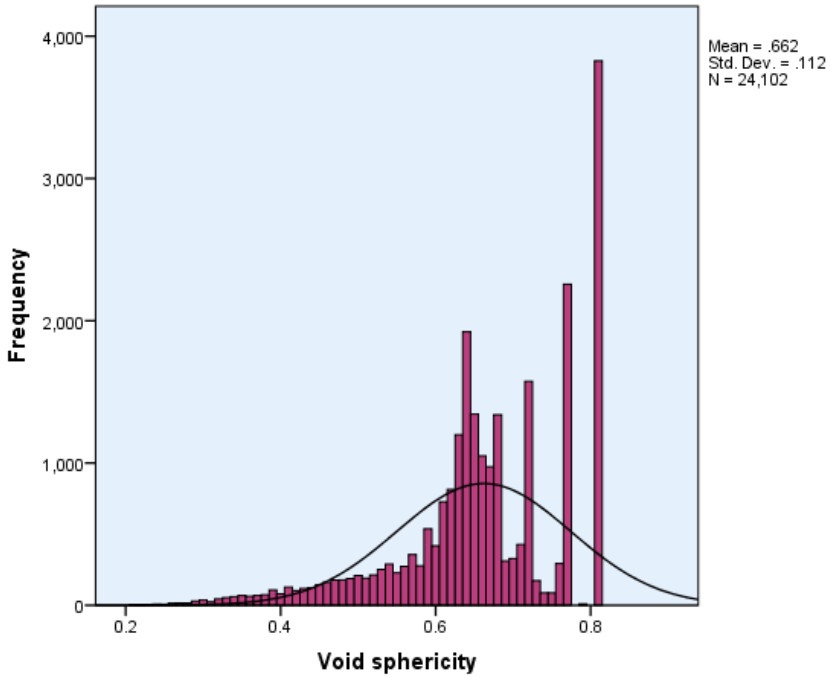

Figure 4.5 Characteristic graph illustrating void sphericity showing higher possibility of spherical pores (+16/-11.2 mm) particle. Sphericity index on a scale of 0 - 1.

While fissures were not readily quantifiable, it was observed that cracks preferentially formed in the vicinity of large pores, probably during crushing because of the material being structurally weaker in such regions. As seen in *Figure 4.6a,* pores of a lump particle before crushing clearly excludes the dendritic structure of cracks in the voids. *Figure 4.6b* demonstrates the presence of cracks developed along large pores, while *c* shows no crack throughout the particle. However, *Figure 4.6c* has pores that are smaller than the particle of

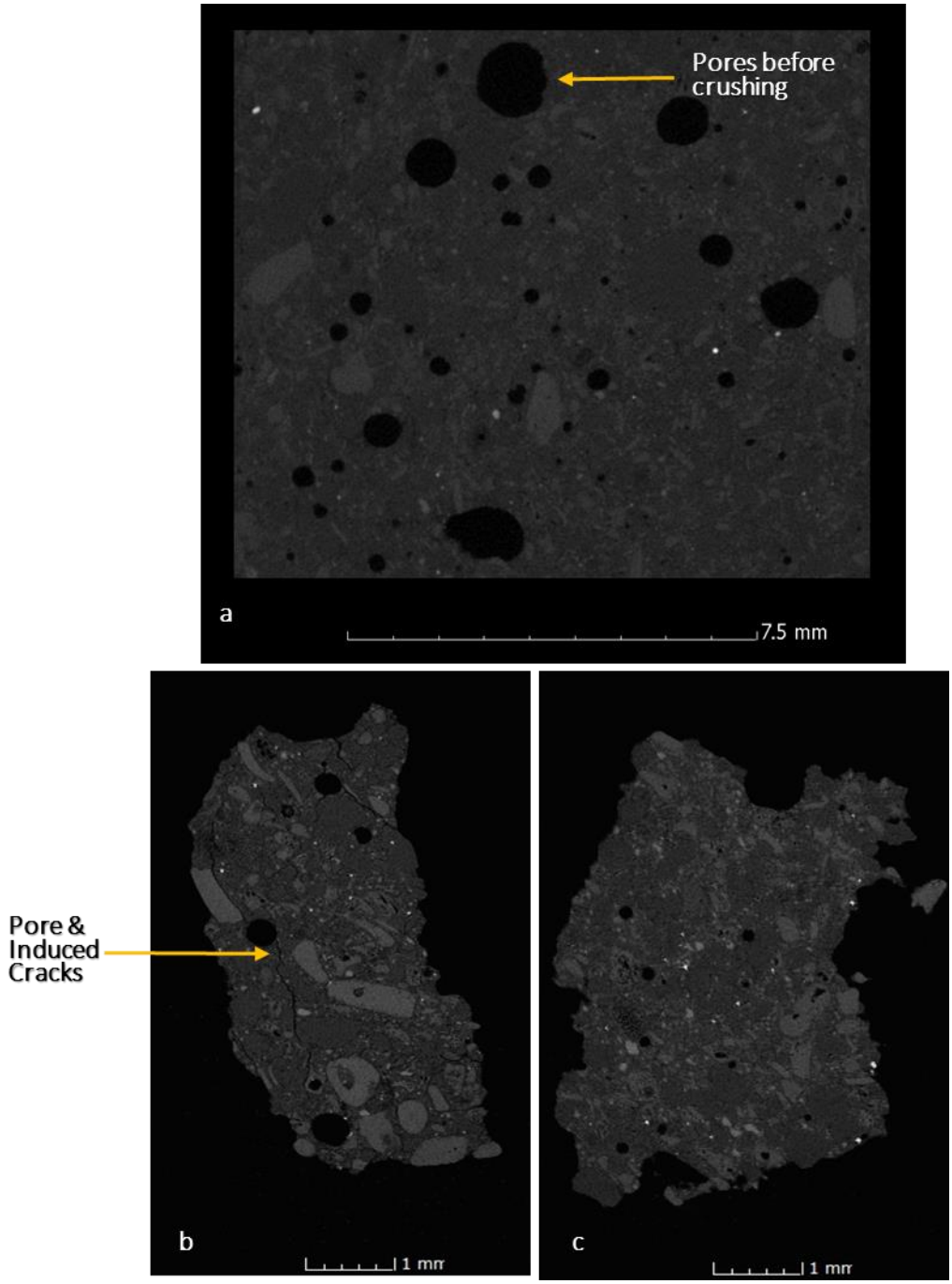

Figure 4.6 (a) Reconstructed XCT diagram of lump synthetic ore (40 mm) showing no cracks before crushing. (b) 2.8 mm practice showing induced cracks along large pores as well as running through the particle. (c) 2.8 mm particle exhibiting smaller pores without visible fractures along pore regimes nor through the particle. a) was scanned at ~20um while b & c were scanned at 4.8 μm resolution.

b. Cognizant of sub-micron cracks possible in the material (*Ghorbani, 2012*), it is not safe to postulate that no crack exists in such particles with spontaneously isolated pores.

Although it was initially anticipated that crack networks could have been independently determined after crushing due to the brittle property of the ore, cracks were not easily quantifiable at the 20-micron resolution used in the investigation. With a scan performed at a higher resolution (4.8 µm), cracks were also unable to have been quantified. Thus, it is perceived that the fissures were of a submicron size which disallowed making any inferences given the resolutions (20 µm & 4.8 µm) used in the tests.

4.2.2 *Porosity by Water Absorption Tests*

The determination of the porous nature of the synthetic silver ore through water absorption was done in order to compare the overall average porosity with XCT and the literature. Porosity tests were conducted by analysing the amount of water absorbed by different particle size fractions over specific time intervals (i.e. periodically over ~17 days) as outlined in *section 3.5.1.1*.

The results of porosity tests are presented in *Figure 4.7*. It reveals minor variations in porosities between the particle sizes used in the study. Water penetration in larger samples was quite slow or almost negligible, resulting in a lower water mass gained; while smaller particles, on the other hand, possessing more exposed void spaces resulted in higher porosity values. The very high porosity determined in the -4/+2.8 mm size fraction has been consistently observed after repeated runs and was attributed to larger surface-volume ratio of the samples in this size class. Unlike the larger particle size classes, the smaller fractions had a large number of particles in a given weight of the ore measured across all the investigated size classes, thus resulting in increased absorption at the surface and sub-surface of the -4/+2.8 mm samples. The average porosity obtained utilizing the pore absorption technique was 3.5%. It must be noted that the absorption

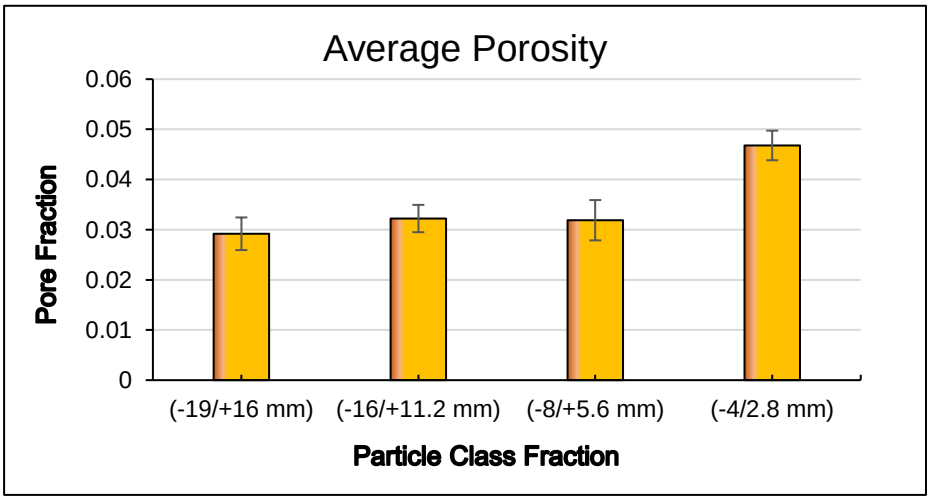

Figure 4.7 Average porosity fraction of each particle class obtained using manual water absorption measurement.

approach was probably biased to some extent due to residual surface wetness considering that not all surfaces attained uniform drying after the soaking test.

In an effort to compare the pore volume of the synthetic ore, average porosity results of micro-XCT, the water absorption approach, and pore volume per cent of artificial ore from *Dixon & Hendrix (1993)* are collected into *Figure 4.8*. Both methods give similar results with a relative variation of 14 %. This suggests the two tests differed by no more than 14 % in terms of their prediction of the synthetic ore porosity measurements.

However, the pore volume performance of each class fraction of both water absorption measurements (WAM) and XCT shows that the small size fraction gives the highest pore volume using the adsorption method and the lowest using XCT. The opposite trend was observed with the other selected investigated particle fractions. Thus, it could be postulated that the two methods targeted different pores - XCT measured the bubbles which give a certain voidage that is not visibly connected, while absorption measurements suggest clearly there is continuous pore structure that absorbs the water.

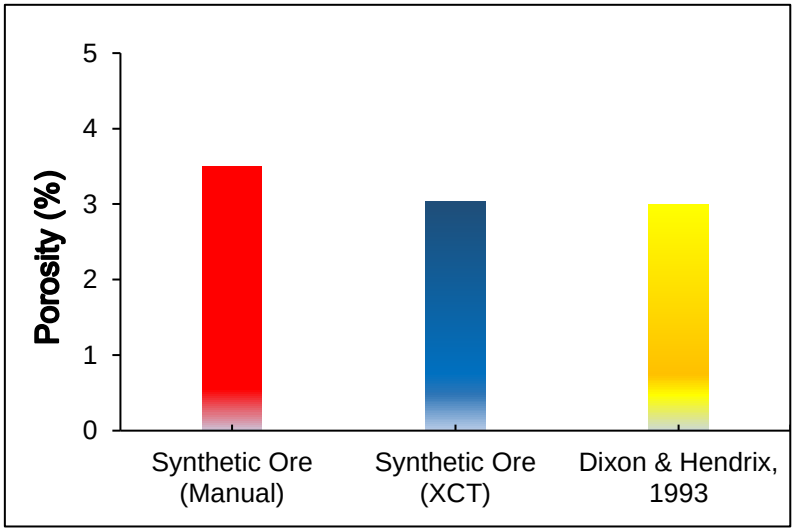

Figure 4.8 Porosity comparison of both XCT and manual approaches as well as pore volume of artificial ore from literature [Dixon & Hendrix (1993)].

For the water absorption test, water migrates into the particle, hence the migration was achieved through micro-porous networks that were not visible in the XCT at the scan resolutions. Considering that the smaller fractions possess more micro-porous fissures, it is perceived that only the small particles were properly soaked through, whereas the bigger ones were not fully penetrated.

Therefore, assuming the pores in the particles were filled over the experimental time, then the total pore volume of the WAM should be higher than the pore volume of the XCT investigation as observed in *figure 4.8*. The higher pore volume in the WAM test is obviously attributed to the volume of water absorbed into

cracks (ultimately within the -4/+2.8 mm fraction) as well as the pores within the particles. Whereas, XCT only measured the isolated larger voids in the particles.

Categorically, the two methods would have only been identical if the XCT had quantified as many cracks as the WAM ultimately did. Thus, because there are two mechanisms of pore volume operating in the two methods, it can be concluded that the pore volume of the synthetic silver ore is in the range of 3~3.5 % characterized with apparently large isolated pores and submicron fractures.

4.3 Grain Characteristics

4.3.1 *Grain Size Distribution*

Metal grain characteristics were determined in order to investigate the dispersion of silver grains in the artificial ore and obtain the ore grade value. The size of the silver metal used in this study was predetermined in the size range of 4~7um (*section 3.2.1*). This provides a perfect correlation for metal size occurrence in low-grade ores. We recalled that individual fine grains occurring in natural low-grade gold/silver deposits are in the range of 1~10um (*Bartlett, 2013)*. Markedly, such fine grain size range is not visible to the eye without visualization techniques such as XCT or QEMSCAN.

Determination of the grain size as observed in the XCT investigation was conducted at 20 μm resolution. This suggests that smallest grains quantified in the analysis may have been a combination of a few grains (three to five grains) agglomerated; while larger grains were an indication of many silver grains combined. This effect is illustrated in *Figure 4.9* right-skewed showing the distribution of grains present where more than 90 % of the grains are less than 200-micron diameter. *Nwaila, (2014)*, corroborates similar right-skewed trend and grain distribution of low-grade gold/silver ore.

The size of grains determined as shown in *Figure 4.9* tends to validate the initial assumption that grains visible at 20 μm resolution were as a result of several infinitesimal grains aggregation during the production of the artificial ore. However, the size distribution of the grains at 20 μm resolution is perceived to be highly exaggerated as a result of the partial volume effect thereby overestimating the grain size in each investigated class fraction. In order to determine if the objective of having a homogenous grain size distribution of the metal was achieved in the ore, the XCT scan at 20-micron resolution was not sufficient nor reliable. Therefore, QEMSCAN and XCT Scans were performed at higher resolutions (4 and 4.8 microns respectively) on selected particles of the -4/+2.8 mm class fraction.

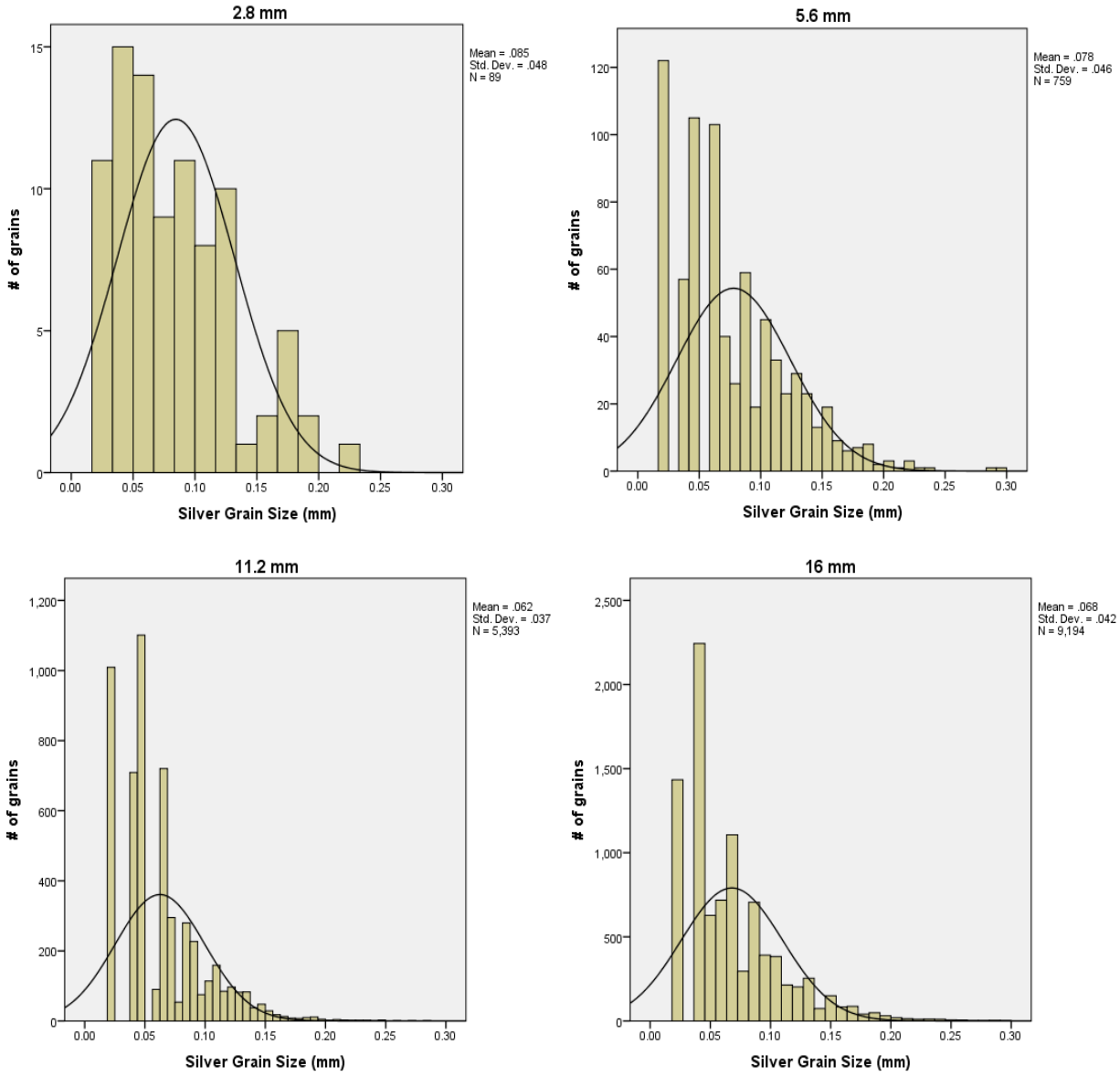

Figure 4.9 Frequency distribution of silver grains diameter in each fraction of the synthetic ore at 20 μm resolution.

Figure 4.10 presents a data comparison of both QEMSCAN and XCT of the -4/+2.8 mm particles scanned at 4-micron and 4.8-micron resolutions respectively. Cumulative Mass wt% of silver grains from the QEMSCAN data shows that more than 85 % of the actual silver grains observed are below 20 microns, while XCT shows that 85 % of the grains are below 40 microns. The XCT analysis revealed that grain size in the range of 6-15 μm constituted 33 % of the total grains present in the particle; while the QEMSCAN data in a similar grain size range (5-15 μm) constituted 43 %. It is worth noting that ~6 microns were the minimum grain size analysed in the CT data at 4.8 μm resolution.

Metal grains below 6 microns were available but were captured in the minimum inclusion of the impurities (2nd dense phase) grey values, thus leading to those results been excluded from the analysed defects. For its

part, the QEMSCAN technique preferentially distinguished the different mineral phases present and provided data for silver grains below 5 microns present in the ore. The <5-micron grains fraction alone consisted of 43 % of the total grains. Thus the full range (<5~15um) constituted about 86 % of the total particle grains of silver.

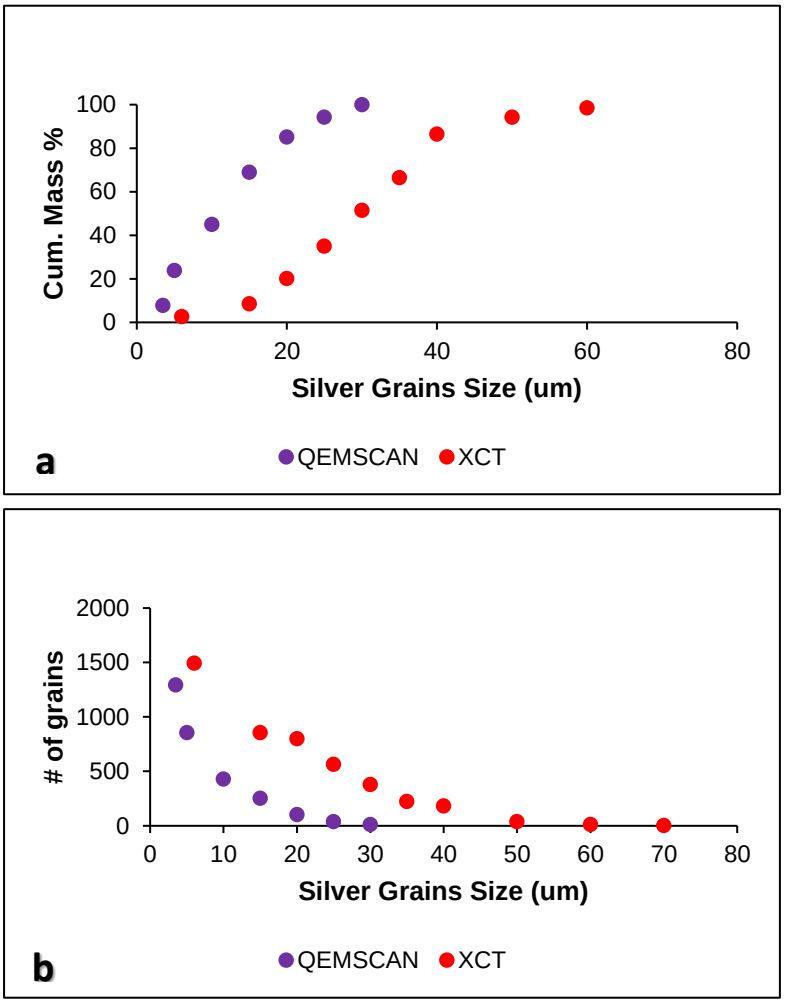

Figure 4.10 QEMSCAN vs XCT data of 2.8 mm class at 4 µm and 4.8 µm respective resolutions plotting silver grains size against (a. Cumulative Silver mass % and (b. Number of grains.

Comparing the two data sets from XCT and QEMSCAN, the latter revealed and validated the presence of silver in a range of grain sizes close to those seeded into the concrete mix. Furthermore, the elemental composition of impurities responsible for influencing the grey value of the silver metal in the XCT technique is provided in a later section (*4.3.3*). From *figure 4.10,* the total number of silver grains were fewer in the QEMSCAN data. This is attributed to the fact that usually, 2D analysis underestimates the size characterization of mineral grains due to stereological biases (*Becker et al., 2016*). While it was not safe to conclude that the d_{80} of the silver grains in the synthetic ore was about ~ 20 microns, the 2D results provided an appreciable basis for analysis to the 3D XCT.

XCT data at 4.8 μm scan resolution illustrated in *figure 4.11* was therefore used to determine the average silver grain size. At such higher resolution (4.8 microns), 80~90 % of the grains were about < 40 microns with the average silver grain size tending about 21-microns. It must be noted that the relatively large grain size up to 40 microns was due to clusters of the silver grain during the production of the ore. The result is reasonably acceptable because no nuggets or very large grain of the metal were formed. Therefore, it can be concluded that the synthetic silver ore is uniformly homogenous in size about 21 μm.

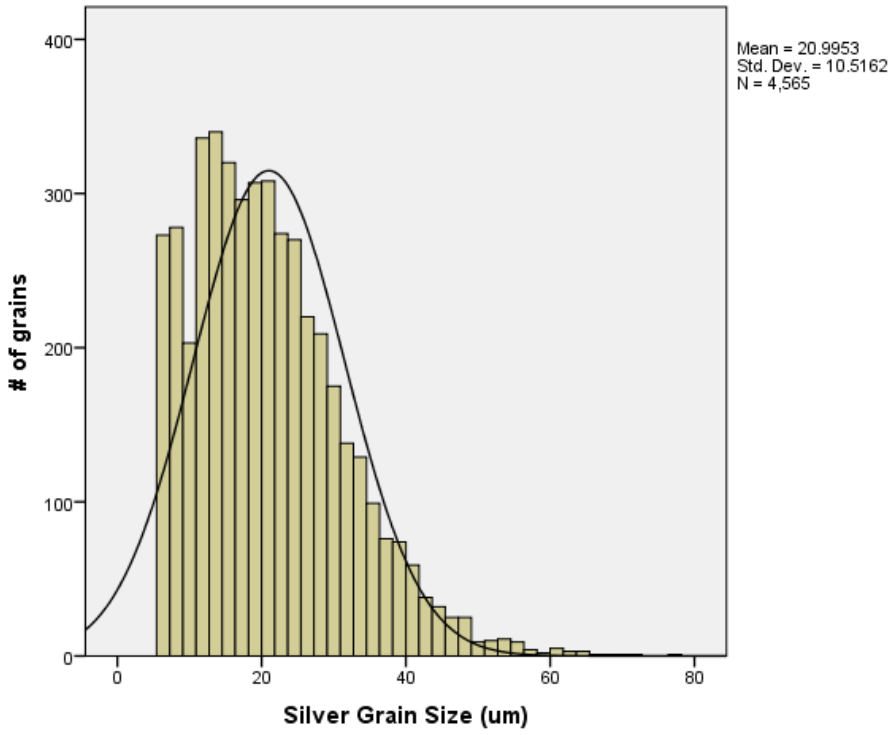

Figure 4.11 Illustration of homogenous distribution of silver grains of the synthetic ore scanned at 4.8 microns XCT resolution.

4.3.2 *Grain Sphericity*

Having established that metal grains are distributed in the ore about a specific size (mean size about 21 microns), the shape of these aggregated grains were studied. *Figure 4.12* presents quantitative data of the mineral sphericity. The figure shows that constituent silver grains in all particle fraction demonstrated sphericity in the range of $0.5 > x < 0.8$. However, the sphericity at 20-micron resolution cannot reliably be considered the true sphericity of the metal grains. This is because the partial volume effect significantly influences the grey value of each voxel at low resolution, resulting in over amplifying the actual shape of grains.

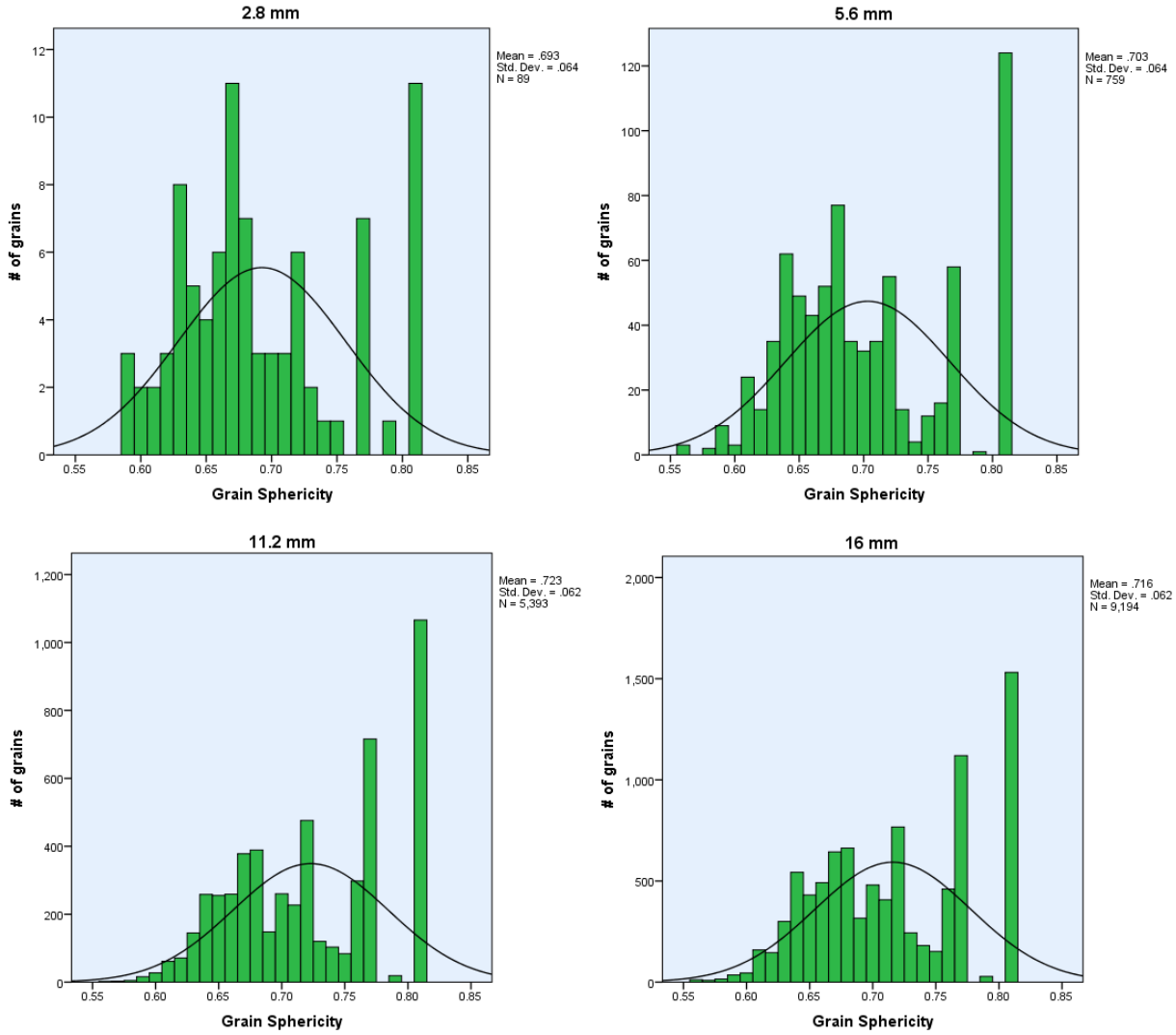

Figure 4.12 Sphericity of silver grains in each selected particle scanned at 20 μm resoluton.

Selected particles of -4/+2.8 mm were scanned at 4.8 μm and 20 μm resolution and compared to validate the true shape of the metal grains present in the matrix (*Figure 4.13*). *Figure 4.13* reveals that sphericity of silver grains obtained from both resolution parameters was similar in range. Obviously, at higher resolution,

the number of silver grains identified was - about two orders of magnitude - greater than the 20-micron resolution.

The sphericity achieved at high XCT resolution (4.8 microns) demonstrated the true sphericity of the silver grains present in the matrix to be about 0.6~0.7 spherical ratio on average. This suggests that only a proportion of the metal present is spherical but the majority was characterized by multifaceted angular phases (*see* QEMSCAN images in *section 4.3.3* and ***Appendix IV***). This is in agreement with *Nwaila, (2014)* who observed similar sub-rounded grain shape in an investigation of naturally occurring gold/silver ore.

Unlike real ores where nuggets of metal grains spontaneously occur amongst fine grains, an effect that influences the metal dissolution kinetics, the XCT investigation reveals that the ideal 'designed' ore met its proposed properties. Achieving these properties in the synthetic ore alleviates possible variability of the study parameters for a potential heap leaching reactive investigation.

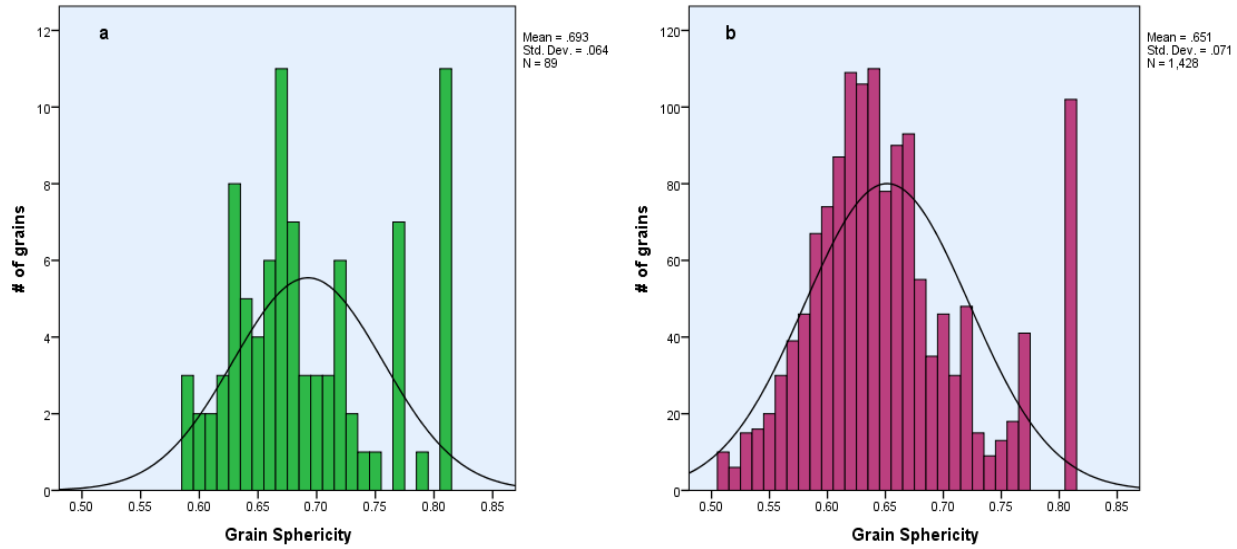

Figure 4.13 Sphericity of 2 particles of the 2.8 mm class fraction scanned (XCT) at (a. 20 microns and (b. 4.8 microns resolutions.

4.3.3 *Particle Grade Distribution*

The grade distribution of silver grains with respect to the increasing size of selected particle fractions was investigated in order to validate the homogenous dispersion of the metal throughout the ore. Grade distribution per cent (XCT mineral grade) was obtained using *Eq. 4.1*.

$$GD = \frac{Vg}{Vp - Vv} \; x \; 100\% \qquad \textit{Eq 4.1}$$

where V_g is the total volume of silver grains in the analysed particle, V_p is the volume of the particle per class fraction, and V_v is the volume of the total void. While the values obtained from XCT were measured in volume (as in *Eq 4.1*), the calculation for the grade distribution wt% was converted and presented as mass wt% utilizing the densities of silver and the ore particle. *Figure 4.14* shows the grade distribution for

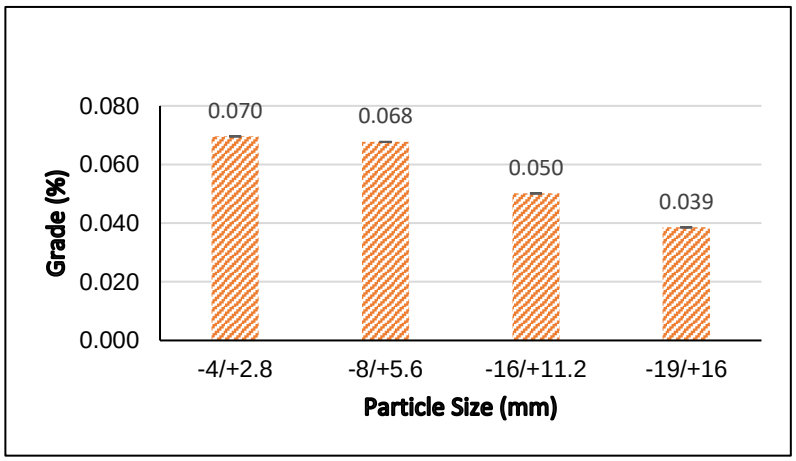

Figure 4.14 XCT grade analysis presented as mass wt%.

each particle fraction. It can be noted that while the grade described in this section is not a full representation of the bulk ore used in the entire study, the results provided estimates and describes the grade distribution possible in the bulk ore. Four of the nine class fractions were investigated. *Table 4.1* gives information on the number of particles analysed.

Table 4.1 Selected class fraction and number of particles analysed for the determination of the synthetic ore grade distribution at 20 μm resolution.

Particle Size (mm)	(-19/+16)	(-16/+11.2)	(-8/+5.6)	(-4/+2.8)
# of particles analysed	21	21	59	356

The dispersion of silver grains seems to not be quantitatively uniform with respect to the increase in the particle size class. This trend was due to fewer particles having been scanned for the larger size fraction. Moreover, impurities were observed in the ore during the XCT analysis evident by lower grey values. Different from the large particles, these impurities observed did not occur in all the small particles to influence the grey value analysis of the silver present. Thus, the grey value minimum inclusion limit was lower (thereby capturing more silver grains) for more smaller particles than in the case of larger ones where the adverse influence of attenuation due to the presence of impurities was apparent.

In order to avoid analysing the impure grains, the minimum inclusion grey value limit of silver was set to values greater than the maximum grey value of the attenuating impure mineral phase. This resulted in a shifting of values that had the propensity of rendering very small grains of silver (perceived to be occurring at just about 20-micron aggregates) as gangue mineral present. Although the number of particles analysed were few, the very small error bars shown on *Figure 4.14* suggest that the analysis of the silver grain was a function of impure phases present in the ore matrix rendering the analysis with fewer silver grains reporting in the larger particle analysed.

The grey value analysis from XCT characterization indeed indicated that not all bright grains quantified were silver grains. It was observed and perceived that attenuation of silver grains was influenced by the presence of large grains of dense phases exhibiting lower grey value. These phases appeared not to be grains of silver, manifested by large grain volume when compared to the silver grains. Essentially, the dense phases apparent in the larger particles exhibiting grey values closer to the silver particles are attributed to these xenophases (*Figure 4.15*). *Figure 4.15* demonstrates that the grey value of the xenophases was observed at the lowest end of the grey value minimum inclusion of silver grains quantified, yet exhibiting large volumes. As evident in *Figure 4.16*, the fewer xenophases were perceived to be other mineral grain association instead of silver present.

The number of these foreign dense minerals was small (1~2 grain(s) per particle and 3~10 grains per class fraction); however, their presence significantly affected the grey value when quantifying the silver grains. Due to the challenge of the partial volume effect as it relates to voxels captured in slices and the limitation of XCT to identify elemental composition of the attenuating dense phases, QEMSCAN was initiated in order to validate this argument and identify the presence of the asserted unknown phases in order to redefine inclusion parameter for the grade distribution analysis. It is believed that these phases were sourced from the sand during the production of the synthetic ore (*Table 4.2*).

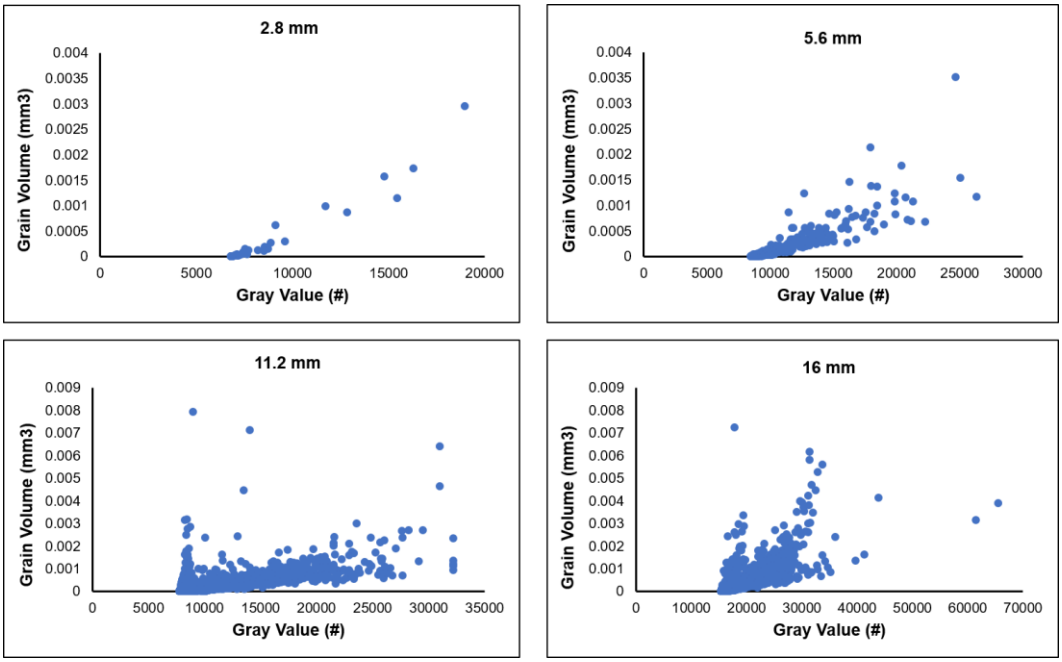

Figure 4.15 Illustration of foreign dense minerals other than silver present; where large volume and lower grey value illustrates the presence of impurities.

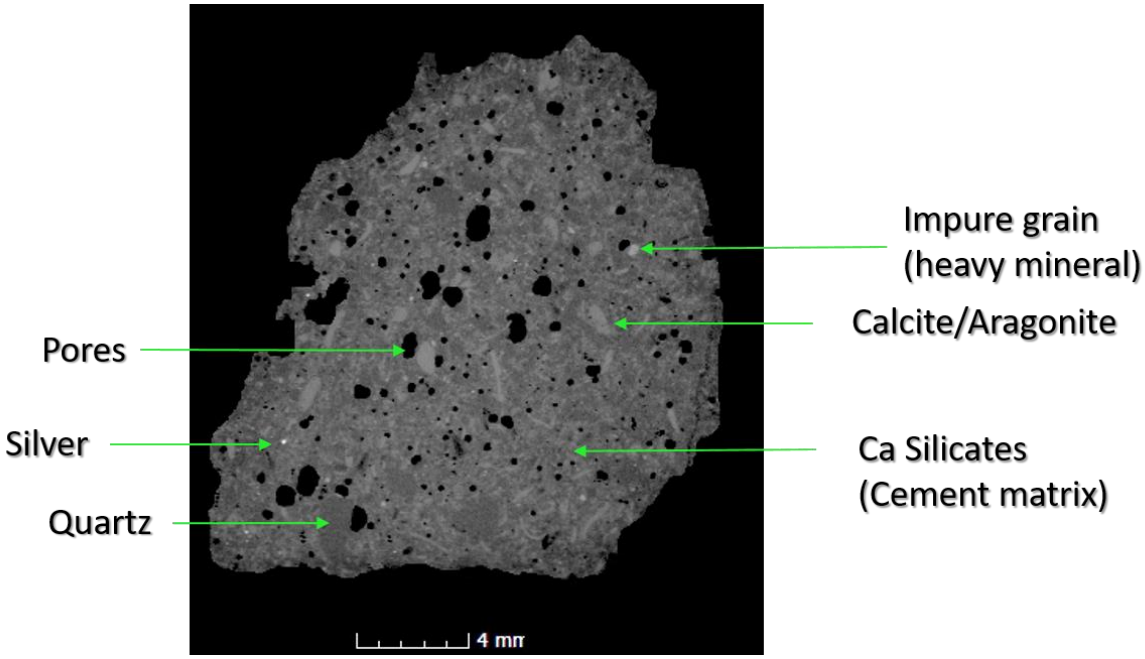

Figure 4.16 Reconstructed slice of 11.2 mm synthetic silver particle illustrating different phases present based on the variation of grey value during analysis.

Table 4.2 Modal composition of sand utilized in the production of the synthetic silver ore.

Mineral	Mass %	Volume %
Quartz	67.121	67.886
Feldspar	0.823	0.834
Mica	0.399	0.405
Amphibole	0.210	0.174
Zircon	0.002	0.001
Calcite / aragonite	30.849	30.222
Fe oxides / hydroxides	0.053	0.034
Ilmenite	0.009	0.005
Rutile	0.011	0.008
Apatite	0.193	0.161
Other	0.329	0.270

Modal composition from QEMSCAN data, depicted in *Table 4.3*, further demonstrated that grains of comparatively large volumes and attenuation, as bright phases similar to silver were indeed not silver (*see Figure 4.15* and *Figure 4.16*). *Figure 4.17* shows the QEMSCAN diagram of the synthetic ore matrix. More diagrams showing the full composition of synthetic ore is provided in ***Appendix IV***.

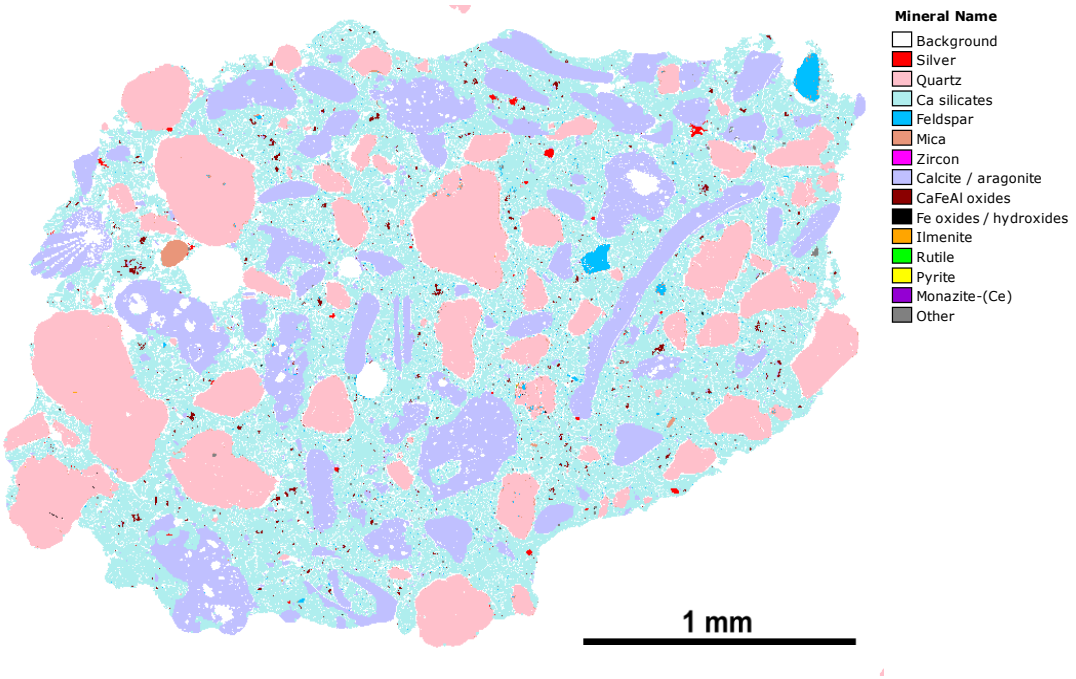

Figure 4.17 QEMSCAN diagram of synthetic silver ore.

Realizing the presence of the foreign grains influence on the attenuation of smaller silver grains, the model developed by *Bam et al., (2020)* based on the empirical composition of minerals to generate attenuation coefficients of each mineral phase, was utilized to determine the attenuation coefficient for each mineral present.

While it is not clear which particular mineral adversely affected the determination of the grade distribution in the XCT analysis, the shape of some of the grains identified in both XCT and QEMSCAN suggests that zircon could have been responsible for these influences. Although monazite exhibited high attenuation, based on the shape and mass wt% observed, it appears that the monazite mineral presence was not large enough compared to the other impurities identified (*see* ***Appendix IV***).

It should be noted that the decision to distinguish the different phases present was not based on the density of the mineral but their X-ray attenuation coefficient. This is due to the fact that density may become misleading in identifying the particular mineral phase present (*Bam et al., 2020*). This can be illustrated in detail as seen in *Table 4.3,* where monazite (Ce) has a lower density than zircon but higher attenuation coefficient; thus disproving the use of only density proportionality to assume mineral attenuation.

Table 4.3 Modal composition of the Synthetic illustrated along with their densities and attenuation coefficients.

Mineral	Mass %	Volume %	Density (g/cm^3)	Chemical Formula	Attenuation Coefficient (cm^{-1})
Silver	0.065	0.076	10.5	Ag	**56.90**
Quartz	25.970	27.969	2.32	SiO_2	**0.57**
Ca silicates*	46.740	43.819	3.15^	$(CaO)_3 \cdot SiO_2$	**1.36**
				$(CaO)_2 \cdot SiO_2$	**1.29**
				$(CaO)_3 \cdot Al_2O_3$	**1.25**
				$(CaO)_4 \cdot Al_2O_3 \cdot Fe_2O_3$	**1.75**
				$CaSO_4 \cdot 2\ H_2O$	**1.04**
Feldspar	0.786	0.778	2.56	$KAlSi_3O_8$	**0.73**
			2.67	$NaAlSi_3O_8$	**0.64**
			2.55~2.76	$CaAl_2Si_2O_8$	**0.77**
Mica	0.292	0.314	2.88	$AB_{2-3}(X, Si)_4O_{10}(O, F, OH)_2$	**-**
Zircon	0.004	0.003	4.7	$ZrSiO_4$	**8.82**
Calcite / aragonite	24.905	26.090	2.83	$CaCO_3$	**1.02**
CaFeAl oxides	0.759	0.565	-	-	**-**
Fe oxides / hydroxides	0.094	0.059	5.24	Fe_2O_3 / Fe_3O_4	**4.44/4.56**
			3.4	$Fe(OH)_2$	**2.64**
Ilmenite	0.027	0.017	4.55	$FeTiO_3$	**3.20**
Rutile	0.016	0.011	4.23	TiO_2	**2.15**
Pyrite	0.005	0.003	5.01	FeS_2	**3.69**
Monazite-(Ce)	0.002	0.001	4.58	$CePO_4$	**24.70**
Other	0.334	0.296	-	-	**-**

* Cement phases (any four compounds are possible)
^ Cement density was used to determine the attenuation coefficient

The objective of the silver grain characterization section was to determine the grade distribution in each class fraction and identify possible mineral inclusions affecting the grade analysis of the synthetic ore matrix. Although the investigation revealed the grain characterization objective was achieved, it is important to point out that limitations exist with XCT when characterizing materials with similar densities. In this investigation advantageously, silver was not only denser but its attenuation coefficient was highest, thereby rendering the grade quantification less problematic. Thus, the homogeneity of grade distribution can be taken as largely dispersed but not entirely.

5 LEACHING CHARACTERIZATION OF ARTIFICIAL SILVER ORE

5.1 Introduction

Ore characterization is the most critical measure in understanding the behaviour of minerals in potential processing contexts. In the advancement of the theoretical understanding of the reaction involving metallic silver dissolution to be used in the heap reactive leaching studies, this chapter reports and discusses results of leaching investigations into the extraction of silver from both pure silver metal particles and from coarse synthetic silver ore by leaching in a sodium cyanide (NaCN) medium. The extraction is presented from laboratory shake flask and CF-FBR results obtained from regular sampling analysis of the leachant solution. Additionally, optimum parameters of the ore leachability were obtained to be utilized in the column investigation. Finally, results in this study are compared to those of previous investigations.

The first part of this chapter characterizes the rate of reaction, activation energy, and order of reaction in the context of pure silver metal dissolution in NaCN. The second part outlines extraction dissolution of the synthetic silver ore coarse particle fractions. The shrinking core model was used to determine the appropriate representation of the process and governing mechanism of dissolution. With a view to establishing reactions involving coarser particle, the extended mixed topology model as proposed by (*Ghorbani et al., 2013*) was used to predict leaching dissolution for heap leaching extraction. The leachable fraction, rate constant and mineral dispersion factor are parameters evaluated with the extended model for application into an existing plug flow reactor model for the heap column leaching investigation (*chapter 6*).

5.2 Leaching of Pure Silver Powder

5.2.1 *Dissolution of Pure Silver*

In view of comparing the solution tracer experiments with a fully characterised leach study on the same ideal ore in a packed bed, solution amendable to the artificial ore was used and studied. The approach of this study includes the utilization of synthetic ore to maximise the homogeneity of the sample. In order to understand the leachability of the synthetic material (ore), characterization of the pure metal used in the concrete was performed. The metal of interest in this study was pure metallic silver powder. The leaching of pure silver was conducted by varying concentrations of NaCN (50, 275, and 500 ppm) in order to rigorously evaluate the rates of dissolution at different temperatures, 25 °C, 48 °C, and 60 °C, in a shaking incubator at 90 RPM.

As recorded in the literature review (*section 2.4.2*)of this study, the extraction of precious metal silver follows analogous reaction dissolution as gold in dilute sodium cyanide solution given, by the Eisner's equation (*Eq 2.2*). In this oxidation-reduction reaction, metallic silver is oxidized in the anodic reaction (*Eq 5.1*) to form stable soluble silver cyanide complexes (argento-cyanide ion).

$$4Ag + 8CN^- + O_2 + 2H_2O = 4Ag(CN)_2^- + 4OH^- \qquad Eq.\ 2.2$$

$$Ag + 2CN^- = Ag(CN)_2^- + e^- \qquad Eq.\ 5.1$$

Rate curves for the dissolution of pure metallic silver according to the Eisner's equation are shown in *Figure 5.1*. The dissolution rate of metallic silver during the experiment shows a trend of increasing extraction with an increase in the reagent concentration. At the operational conditions the experimental result, *Figure 5.1a,* shows that maximum silver leaching was initially achieved after about 9 hours for all concentrations of the NaCN reagent at 25 °C. During this period the curves entered a slower, but continuous leaching phase. However, a similar trend was not observed with the experiments at 48 °C and 60 °C; *Figure 5.1* and *Figure 5.1* of *Figure 5.1* respectively; the latter figures showed more continuous levelling of the extraction after the initial dissolution.

The low initial extraction followed by steady dissolution is believed to be a result of slower dissolution occurring as the NaCN experience mass transfer constraints accessing the surface site of the silver grains. Thus, a limiting effect hindering extraction at this point.

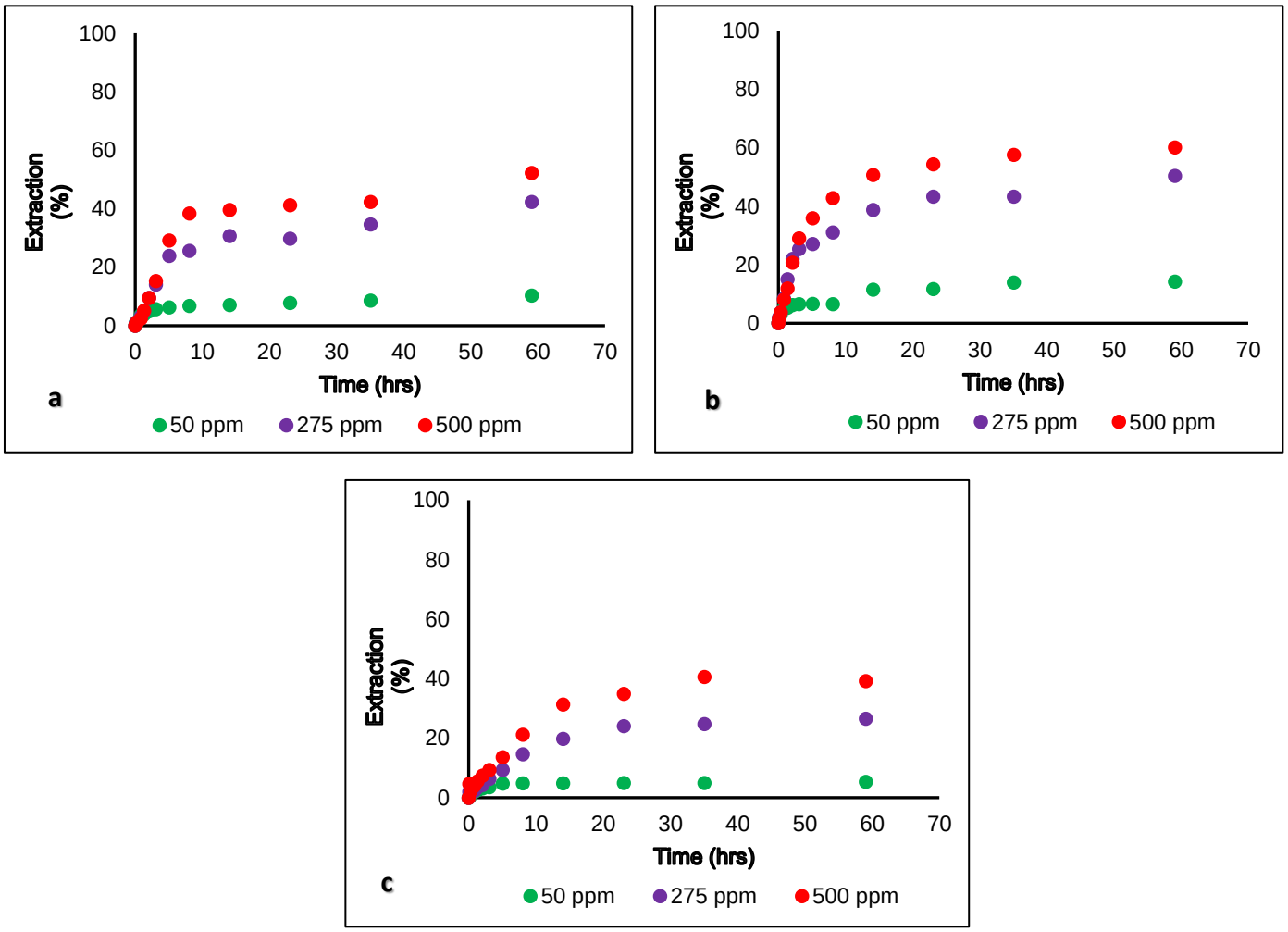

Figure 5.1 Dissolution extraction of pure silver varying NaCN (50, 275,500 ppm) concentrations at different temperature conditions (a) 25 °C, (b) 48 °C, and (c) 60 °C. Using 200 mg pure silver in 200 ml reagent solution.

5.2.2 *Dissolution Rate & Reaction Order*

In order to investigate the rate of dissolution of pure silver, a plot of silver dissolution as a function of time was utilized. By considering the initial slopes of the rate curves, a relationship (*Eq. 5.2*) was developed between the leaching of silver and the lixiviant. Introducing natural logarithms to *equation 5.2*, a linear equation (*Eq. 5.3*) is derived from which reaction order (*n*) and intrinsic rate constant (*k*) can be determined from the slope of the line and *y*-intercept, respectively.

$$\frac{d[Ag]}{dt} = kC^n \qquad \textit{Eq. 5.2}$$

$$\ln\left(\frac{d[Ag]}{dt}\right) = lnk + n\,lnC \qquad \textit{Eq. 5.3}$$

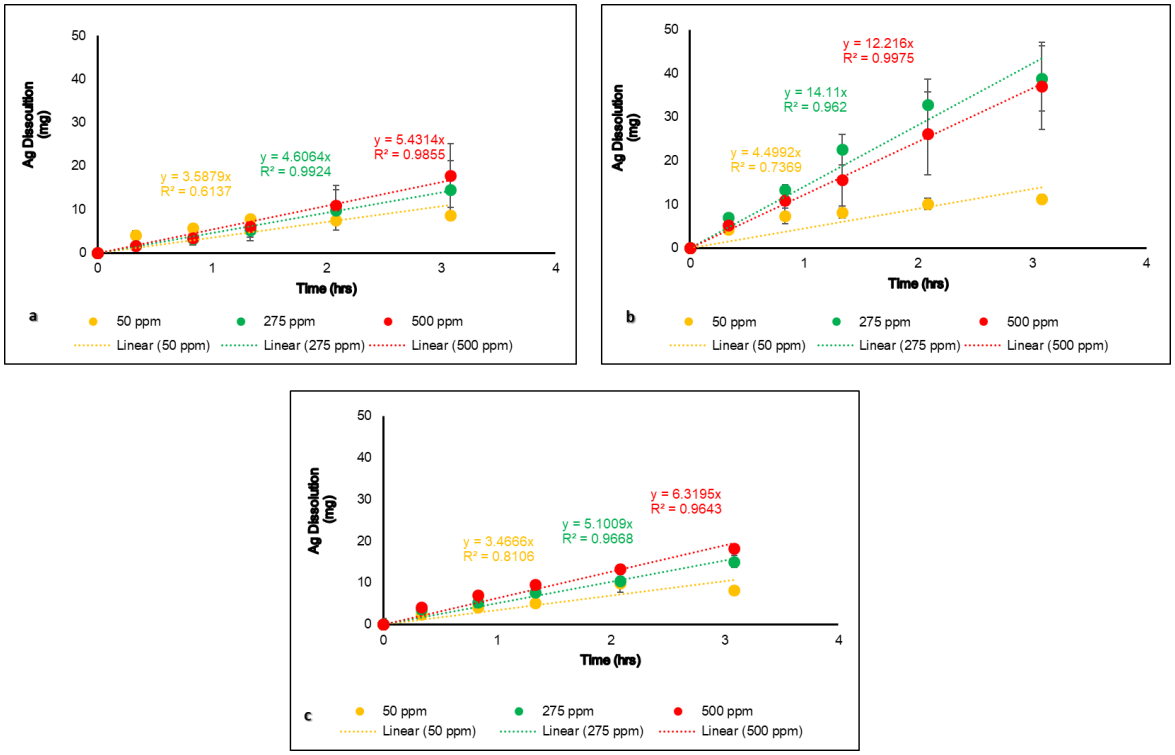

Figure 5.2 Initial rate curve for silver dissolution (mg) at variable NaCN concentrations and temperatures (a) 25 °C, (b) 48 °C, and (c) 60 °C.

The dissolution of pure metallic powder substances, most especially gold/silver metal, occurs rapidly when initially exposed to NaCN solution. This is due to the availability of a larger surface area of the metal and free cyanide ions in the presence of excess oxygen in solution to effect dissolution. *Figure 5.2* presents the results of the initial intrinsic dissolution rate of pure silver powder in varying concentrations of sodium cyanide and temperatures. The dissolution rate of silver is summarized in *Table 5.1*.

As depicted in *figure 5.2*, increasing the concentration of cyanide shows an increase in the dissolution rate of the silver metal grains; however, *figure 5.2b* demonstrates that during the initial reaction extraction the rate of dissolution becomes independent of the lixiviant concentration at higher levels. The change of dependence on the reagent concentration of dissolution is described in the order of the reaction.

The silver dissolution rate obtained from the calculation of experimental data and regression analysis from the plot of *figure 5.2* in *Table 5.1* tends to correspond with marginal variations between the two values. Calculation of the rate of dissolution of the pure silver power was achieved by utilizing the average surface area of 0.25 m^2/g (0.1~0.4 m^2/g) of the pure metal grains. Relating the dissolution rate to those reported

in other investigations, *Table 5.2* reveals that results obtained in this project were some 1~3 orders of magnitude lower.

One reason responsible for the low rate of dissolution compared against literature values relates to the nature of silver used in the each investigation. The ultrafine micron particle used in this investigation may behave invariably different compared to the leaching of plates (*Deitz & Halpern, 1953*) and/or electrochemical electrodes (*Li and Wadsworth, 1992*). Hence, it could be postulated that the slower rate of the metal was possibly due to surface effects which may have influenced the stability of the metal powder in the leaching solution. This surface influence on the rate of silver dissolution from ultrafine particles is perceived to have occurred at small scale. A similar dissolution rate of silver was observed by *Nicol & Mbatha, (1998)* where ultramicroscopic particles of silver were leached in cyanide medium. Although their investigation utilized gelatine to keep the particle continuously dispersed in the solution, the comparable values of the dissolution rate to this current investigation suggest that the leaching of ultrafine particles of silver is assumed to be influenced by surface effects.

*Table 5.1 Rate of pure metallic silver dissolution (**mg/hr**) obtained from experimental data calculation and graphical plot.*

	Calculated Value			Regression Analysis		
NaCN Conc (ppm)	**25 °C**	**48 °C**	**60 °C**	**25 °C**	**48 °C**	**60 °C**
50	4.4	5.4	3.9	3.6	4.5	3.5
275	4.5	14.9	5.5	4.6	14.1	5.1
500	5.2	12.4	6.8	5.4	12.2	6.3

*Table 5.2 Average rate of reaction determined from calculated dissolution data and regression analysis of pure silver powder dissolution (**mol/m²/s**) compared to literature*

NaCN Conc. (ppm)	**25 °C**	**48 °C**	**60 °C**	**Literature**	
50	1.85E-07	2.34E-07	1.79E-07	4.00E-05	*Senanayake, 2006*
275	2.37E-07	7.27E-07	2.63E-07	1.23E-04	*Deitz & Halpern, 1953*
500	2.80E-07	6.30E-07	3.25E-07	4.64E-07	*Nicol & Mbatha, 1998*

In order to achieve statistical confidence with the results of the initial dissolution rate of the pure silver, two additional repeats of the rate experiments over a period of three hours were performed in these studies. Indicated by the error bars in *Figure 5.2,* demonstrating overlap in the error spectra, it is not statistically

conclusive to say with certainty that these data points are different. Although the results might look slightly different, the statistical analysis suggests that there is no significant difference in the performance at a higher reagent concentration; thus 275 ppm NaCN concentration performs as an optimum parameter for the pure silver dissolution suggesting a zero-order reaction type.

Using the initial rates of reaction from the dissolution of silver at varying temperatures, the reaction order for metallic silver powder was determined from the linear regression analysis of plotted dissolution curves. The results are presented in *Table 5.3* and illustrated in *Figure 5.3*. The reaction order was low but not zero, hence it is perceived to be near-zero order with respect to the lixiviant concentration at the experimental temperature conditions. In the event reaction order is completely zero or near-zero order under the range of reagent concentrations considered, the cyanide concentration exhibits a minor global impact on the dissolution process.

The data seems to suggest that the order of reaction at the highest and lowest temperatures was observed to be lower than the middle-temperature parameter. However, accounting for the error margins from the initial rate (*Figure 5.2*), this behaviour can not be confirmed with any certainty. While the lowest and highest temperatures demonstrated a near-zero order of reaction, the middle temperature was observed to show half order of the reaction. This occurred perhaps by a change of mechanism during the dissolution reaction. It was reported by *Li and Wadsworth (1992*) that the inconclusive shifting of dissolution mechanism occurs between the oxidant and the reagent changing from one regime to another in silver dissolution kinetics system. Their investigation leaching rate with respect to cyanide showed a reaction order of about 0.37 with conditions at 24 °C, 500 RPM, and pH 11.

Table 5.3 Order of reaction for the dissolution of pure silver

Reaction Order		
25°C	48°C	60°C
0.1137	0.4498	0.2433

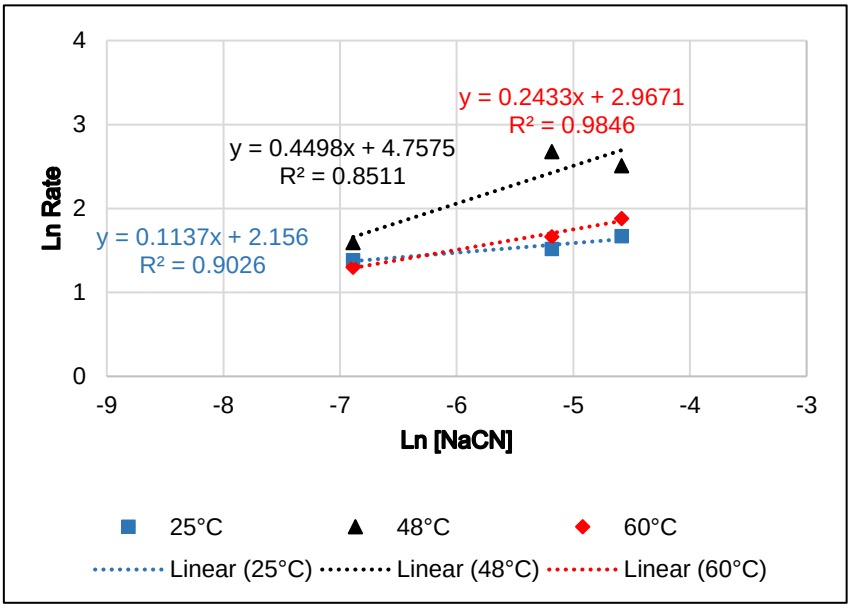

Figure 5.3 Order of reaction determined from silver extraction at varying NaCN concentrations (50, 275, 500 ppm).

Extraction rates were highest at 48 °C compared to the other experimental conditions. This trend perhaps contradicts leaching dissolution of metallic gold/silver which has been proven to exhibit higher rates of extraction as the temperature is elevated up to a threshold limit of 80~85 °C (*Marsden & House, 2006; Hlabangana et al., 2018*). Additional possible explanations for the low rate of pure silver dissolution observed here can be attributed to three circumstances:

- The presence of silver cyanide complex changing to other complexes of silver in solution,
- The low solubility of oxygen in the environment of the leaching experiment, or
- Insufficient agitation to effect vigorous movement to the silver powder in order to alleviate diffusion constraint of NaCN at the surface site of the metal.

In the cyanidation process of silver dissolution, argento-cyanide ions may occur in several forms ($Ag(OH)^0$, $Ag(CN)^0$, $Ag(CN)_2^-$, $Ag(CN)_3^{2-}$ and $Ag(CN)_4^{3-}$), based on the stability of the ions in solution and the ratio of cyanide to silver in solution. Predominantly in solutions of low cyanide-silver ratios, $Ag(CN)_2^-$ is the most stable and abundant in solution while the other species are so marginal that their presence could be neglected (*Senanayake, 2006*). It was further reported that at a slightly high concentrations of cyanide (0.05% CN^-) in the presence of 1 mg/l of metal silver, the complex silver ($Ag(CN)_2^-$) changes to ($Ag(CN)_3^{2-}$), becoming the principal complex form of silver in the solution (*see Figure 5.4*). Nevertheless, the concentration of sodium cyanide in the current investigation is in the range of (1-10 mM CN^-) a stability

region where ($Ag(CN)_2^-$) dominance is maintained. Thus the possibilities of the silver in solution changing from its complex stable form which would affect the dissolution could not have resulted.

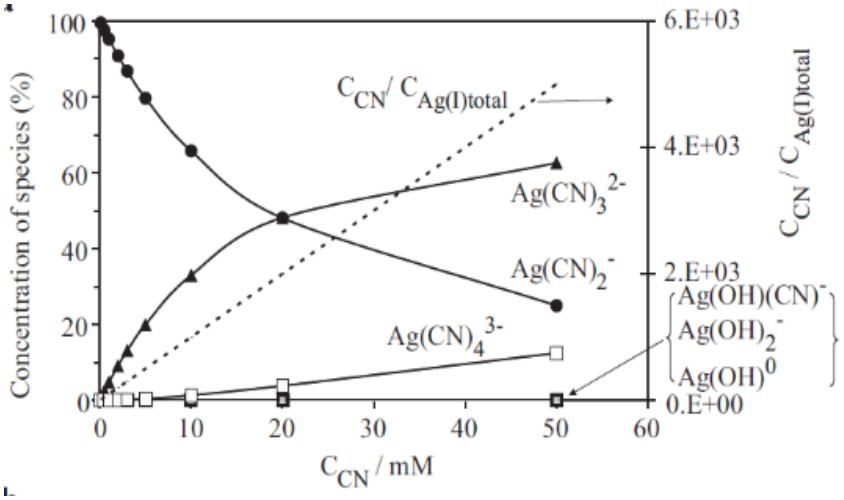

Figure 5.4 Diagram illustrating conditions of stable species of silver cyanide water system at 25 °C adopted from Senanayake, (2006).

5.2.3 ***Activation Energy***

The activation energy of the silver reaction was investigated by varying NaCN concentration solutions with the established Arrhenius equation (*Eq 5.4*) where temperatures were varied in the range of 25 °C, 48 °C, and 60 °C. The Arrhenius plot of the rate constant and the temperature is shown in *Figure 5.5*. Activation energies were determined for each temperature and NaCN concentration. Slopes of initial rate curves were obtained from plots of silver dissolution as a function of time. By introducing natural logarithms to *equation 5.4*, a linear equation (*Eq 5.5*) was derived from which the activation energy (E_a) was determined from the slope of the line (k). Other variables in the equation are the frequency factor (A), the universal gas constant (R), and the absolute temperature (T).

$$Slope\ (\boldsymbol{k}) = Ae^{-\frac{Ea}{RT}} \qquad \textit{Eq. 5.4}$$

$$\ln(k) = lnA - (\frac{Ea}{R})(\frac{1}{T}) \qquad \textit{Eq. 5.5}$$

The approximate energy values required for the dissolution of silver exposed to 50, 275, and 500 ppm NaCN solutions were 6.73, 4.55, and 4.41 kJ/mol respectively. Activation energy determined was far too low for the reaction to be kinetically controlled. This is indicative that the dissolution of silver metal is controlled by a mass transfer constraint.

In similar chemical dissolution reaction using a pure silver plate, *Deitz and Halpern, (1953)* recounted activation energy of 10 kJ/mol at 3.4 atm oxygen partial pressure, 0.18 % NaCN, and a temperature range of 24 °C – 110 °C. It was postulated the reaction was diffusion governed by NaCN transfer to dissolve the metal. It can be noted that the experimental conditions were quite aggressive and reagents in excess; furthermore, the agitation utilized was at 895 RPM. Diffusion of cyanide ions at the surface site in the dissolution of silver was corroborated by *Li and Wadsworth (1993)* reporting activation energy of 10~13 kJ/mol considering a temperature range of 24~60 °C similar to this study.

As mentioned earlier, the rotational speed of the shaking incubator for the leaching characterization test work was 90 RPM. Despite better agitation observed by *Deitz and Halpern, (1953)*, the dissolution of pure silver in their studies corroborated with similar low activation energies in this current investigation. This suggests that the diffusion controlling mechanism demonstrated by low activation energies is perceived to have been systemic rather than the characteristic performance of any particular experimental set-up. This postulation corresponds with results from a follow-up investigation on the influence of agitation to vigorously disperse the silver powder in solution utilizing batch stirred reactors performed at 700 RPM and similar temperature varying conditions (25 °C, 48 °C, and 60 °C). The activation energy in the said investigation revealed similar low energies in the range of 2.71, 2.98, and 11.69 kJ/mol relating to 50, 275, and 500 ppm NaCN respectively. Extraction data is provided in ***Appendix V.a***.

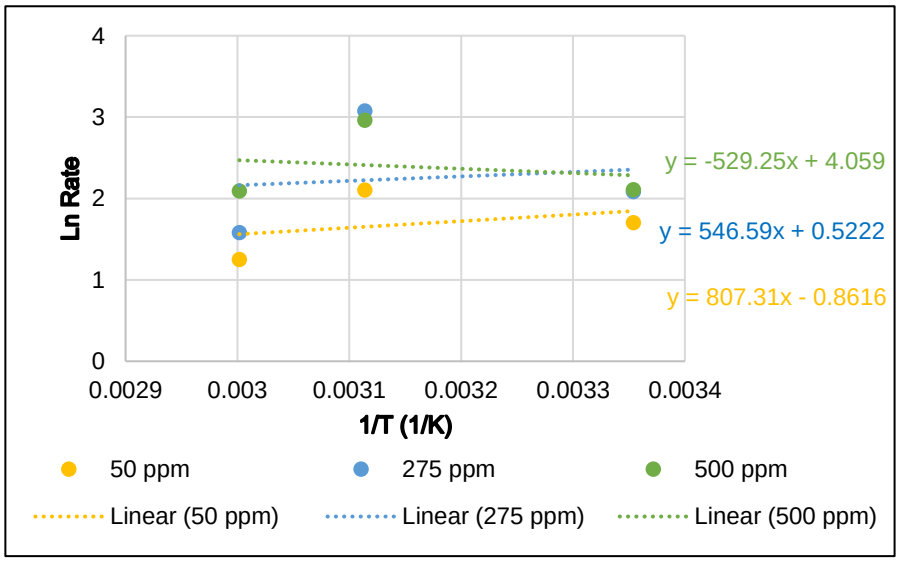

Figure 5.5 Rate constant vs temperature variation illustrating the activation energy of silver reaction.

5.2.4 *Effect of Temperature on Extent of Extraction*

As mentioned in *section 2.4.4*, it is established that the dissolution rate of gold/silver metals increases as the temperature is increased until a threshold temperature limit of 80~85°C is attained. The effect of temperature on the pure silver dissolution extraction assessed in this study did not seem to follow such a trend. From the leaching rate curve in *Figure 5.6* considering the reaction time at ~ 59 hours of pure silver leaching, extraction was observed to be maximum at 48 °C. The leaching at a higher temperature did not improve the dissolution of silver; instead, a drop to below the extraction at 25 °C occurred for each NaCN concentration. This indicates that the dissolution of precious metal (silver) was not governed by increasing the temperature above 48 °C - which was not an expected behaviour-, but apparently limited by surface effects of the ultrafine silver powder.

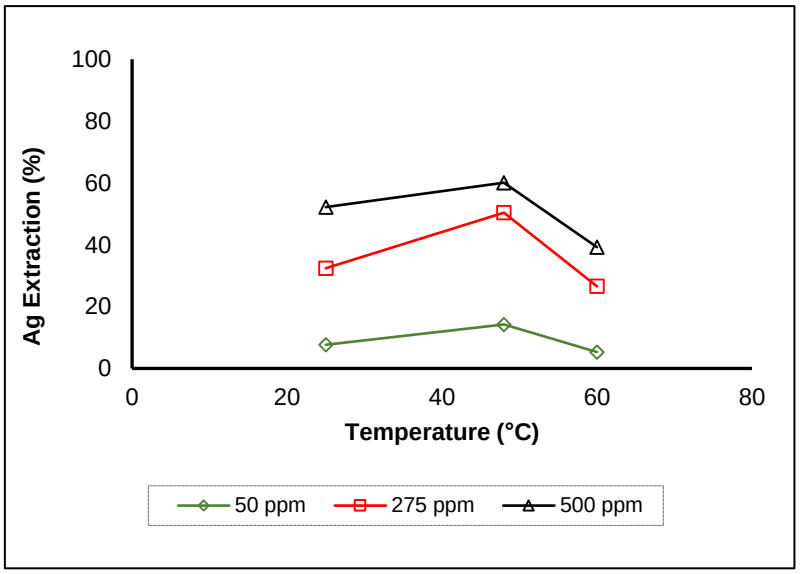

Figure 5.6 Dissolution recovery of silver as temperature is increased at ~60 hours of reaction time in varying concentration (50 , 275, 500 ppm) conditions of NaCN.

The overall silver dissolution (*Figure 5.1* and *figure 5.6*) from the pure leaching experimental work showed that maximum observed recovery was ~ 60 % at 48 °C; while extraction at 60 °C (~ 39 %) was the least, lower than the dissolution at 25°C (~ 52 %). The extent of leaching pure silver for about ~2.5 days was low. This corresponds to the low rate of kinetics discussed earlier.

While it can be argued that the solution was not starved of NaCN to control the process, the rate of dissolution at 50 ppm clearly presents a scenario of a starved system where the dissolution rate showed no improvement. The low rate performance was possibly attributed to global molecular diffusion limiting the reaction at the boundary of the pure metal surface and the NaCN lixiviant. Apparently, products of the reaction were continually deposited on the mineral surface, inhibiting further dissolution. Hence, NaCN is

perceived to have been constrained by mass transfer at the reaction site, inhibiting penetration at the lixiviant-surface boundary layer. This led to rapid extraction over a few percent from the initially exposed surfaces after about 9 hours and was followed by a level-off slow steady dissolution (see *Figure 5.1*). Finally, surface influences of the ultrafine powder of silver and the constant exchange of oxidant-lixiviant interaction, coupled with the recognised molecular diffusion limiting effect were factors perceived to have ultimately influenced lower dissolution rate of the pure silver powder.

5.3 Leaching of Coarse Synthetic Silver Ore Particles

Most silver occurrences are in compounds (i.e antimony and arsenic minerals) that make the leaching difficult (see *2.4*). However, even in its metallic form, the rate of leaching is lower than gold. Adequate knowledge of the controlling stage from kinetics studies provides insights into the reaction mechanisms, with which conditions for improving the leaching extraction using heap technology can be determined. The characterization study of silver in NaCN solution is therefore extended to leaching coarse synthetic ore particles containing pure metal based silver powder. The objective of the characterization studies is intended to obtain optimum parameters typical for implementation in the heap leaching experiments based on the response of the synthetic ore to NaCN attack.

Two experimental setups were initialized in this study phase. Leaching using flasks in a shaking incubator and leaching in a CSTR circulating fluidized fixed bed reactor (CF-FBR). The results of the shake flask leaching at all particle fractions are presented, followed by a discussion of the influences of temperature and NaCN concentration on the coarse particle leaching. Leaching of selected class fractions in the CF-FBR is also presented. The response of dissolution extraction in both systems is compared on the leaching kinetics of the coarse silver synthetic ore. Extraction results are fitted to models to determine dissolution mechanism and to predict large particle kinetic performance in the reactive column leaching investigation. Finally, leaching extraction with respect to the influence of porosity and grain dissolution from XCT defects is discussed.

5.3.1 *Large Particle Silver Extraction (Shake Flask)*

The leaching extraction of silver from large ore particles in this study were calculated from nine sets of leaching data in all the size fractions including -19/+16, -16/+11.2, -11.2/+8, -8/+5.6, -5.6/+4, -4/+2.8, -2.8/+2, -2/+1, and < 1 mm. Conditions for the coarse particle extraction were sodium cyanide concentration at 275 ppm and 25 °C temperature. Leaching was observed over a period of about ~108 hours agitated in flasks by shaking incubators at 90 RPM. Extraction curves for the different size class fractions are illustrated in *Figure 5.7*.

It can be deduced from *Figure 5.7* that extraction from all the ore particles was low. Maximum extraction was observed with -4/+2.8 mm particle fraction extracting about 5.05 mg of silver from a head grade of about ~ 150 mg in 300 g of ore feed utilized in the batch experiments. In the dissolution of metals from large particles, the exposed surfaces of the particles are predominantly the primary regions for initial solution-metal attack for reaction to occur. As leaching continues over longer periods, partial conversion increases until the surface becomes depleted of metals, or until the leaching period is terminated. The leaching rate would become significantly reduced after the initial reaction period.

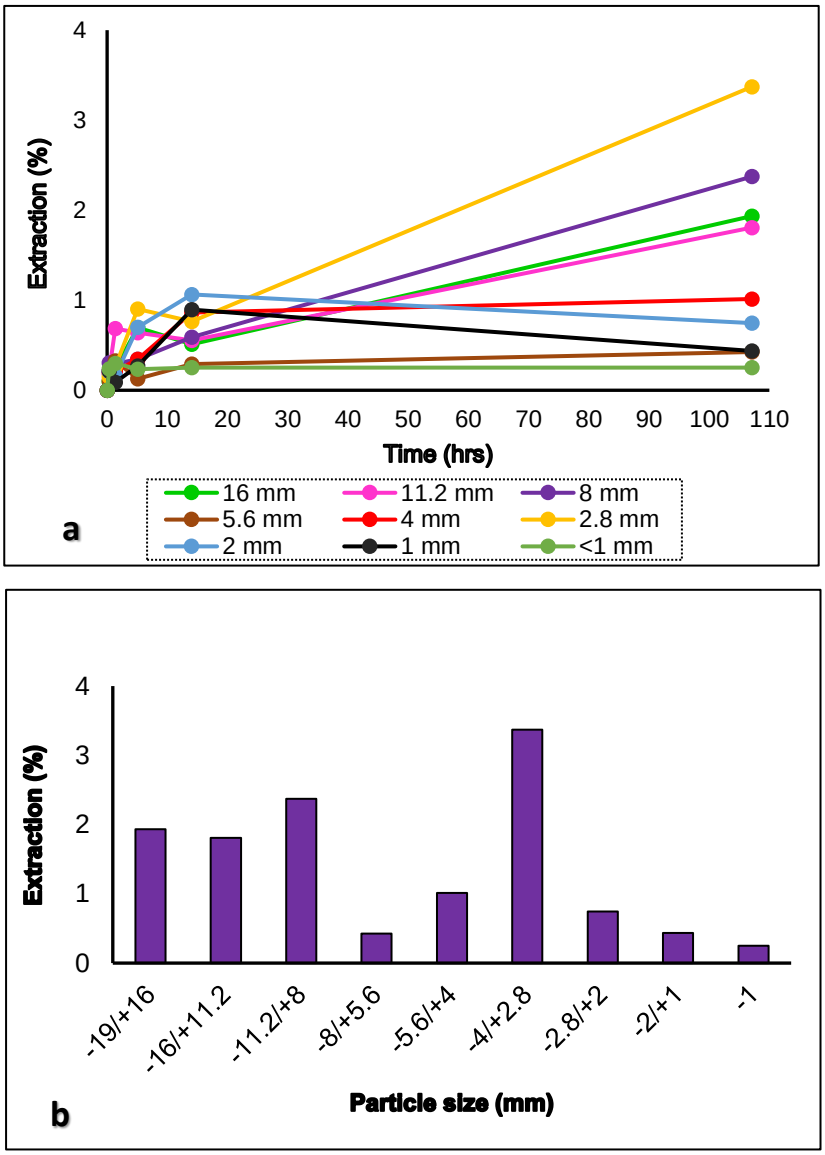

Figure 5.7 Coarse synthetic ore shake flask extraction of silver at 25°C and 275 ppm NaCN (a) vs time, (b) vs particle size fraction after 108 hrs.

The leaching of silver from the <1 mm particles exhibited the least extraction. It is well established in the literature (*Bouffard & Dixon, 2007; Kasaini et al.,2008; Bartlett, 2013*) that leaching of metals is promoted as the particle size is decreased; however, this was not readily the case utilizing the shaking flask leaching approach in this investigation. The leaching behaviour of all the class fractions was inconclusive. Two reasons are assumed to be plausible for the observed extraction trend.

1. The feed sample (300 g) was relatively small to contain much silver; or
2. The coarse particle surfaces contained fewer grains of silver that were initially leached but extraction was not promoted beyond the surface or near subsurface regions; plausibly inhibited by pore diffusion, even in the <1 mm ones.

It was also observed during the leaching that <1 mm particles tended to settle and compact below the agitated lixiviant solution, leaving only the top surface layer for interaction with the NaCN in solution. Complete settling of the fines to the bottom of the flask was observed after six hours of leaching.

The low extraction in the large particle leaching furthermore corresponds to the low reaction kinetics rate of the pure silver powder discussed earlier in the chapter. While the silver dissolution from the coarse particle was low, it is worth to mention that the leaching period (~108 hours) was perhaps relatively insufficient for higher extraction.

5.3.2 *Effect of Lixiviant Concentration*

With an interest to investigate the influence of the cyanide concentration variation on the silver ore leaching, temperatures were held constant while varying the concentration of NaCN. Selected large particles of the synthetic silver ore at different size fractions utilized in this investigation were -16/+11.2, -8/+5.6, and -2/+1 mm. *Figure 5.8* demonstrates a similar trend as compared to the pure silver leaching, where increasing concentration improved the extraction of silver from the large particle. However, the concentration variation seems to not have much of an effect on the dissolution of silver from the coarse particles. This confirms the near-zero order effect from the pure silver leaching.

In gold/silver ores system of leaching, several investigators (*Bouffard & Dixon, 2007, Hlabangana et al., 2018*) also revealed that increasing the cyanide concentrations were found to improve the dissolution recovery of the metal with optimum condition at about ~200 mg/L; although leaching at ~500 mg/L higher recovery is achieved, it can be noted that extraction recovery was not significant than recovery obtained using ~200 mg/L. Therefore, alluding to this study that high cyanide concentration does not affect the dissolution rate significantly.

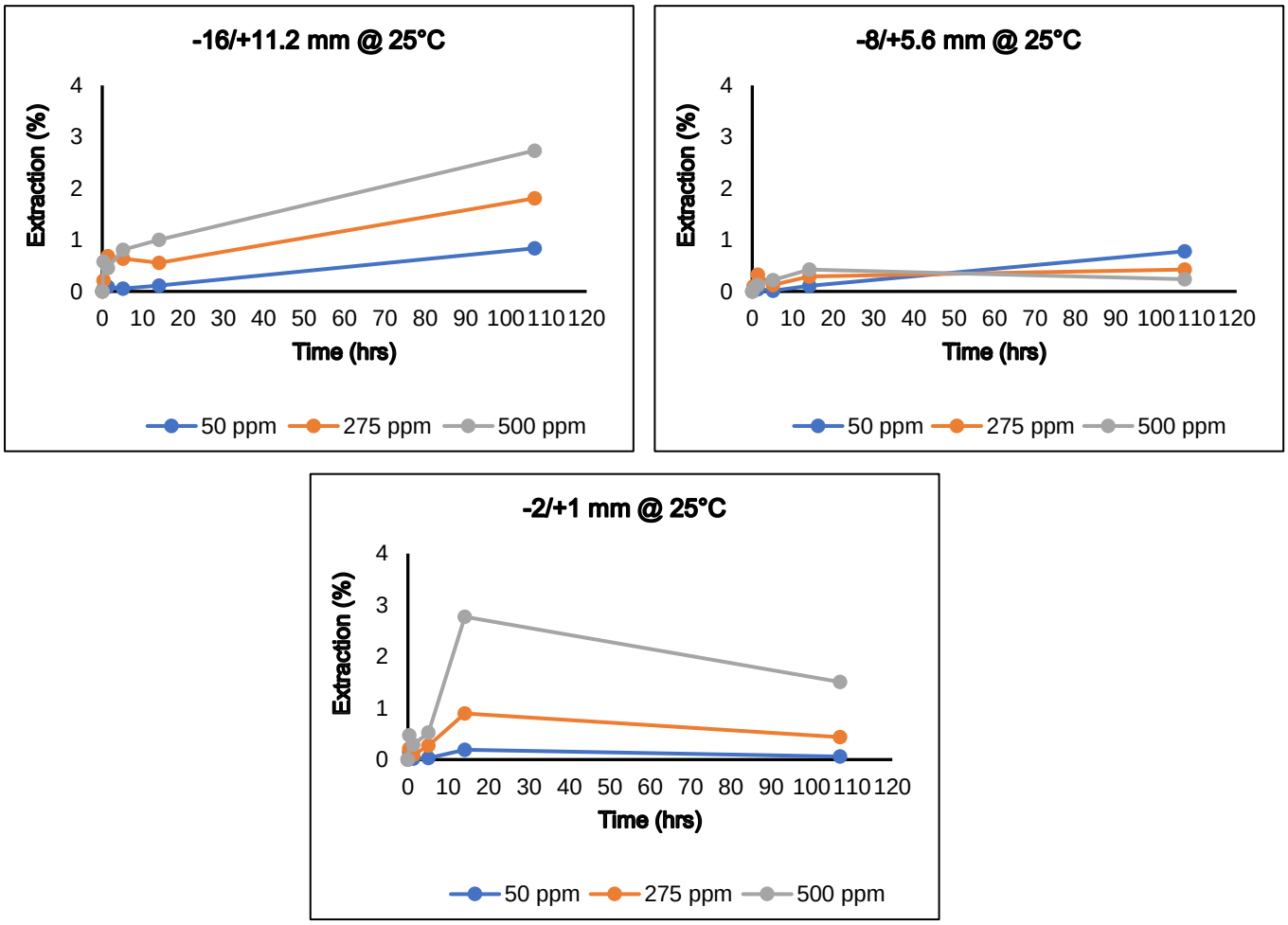

Figure 5.8 Dissolution of coarse synthetic silver ore particle at 25 C temperature while varying the NaCN concentrations on three class fractions. The feed sample was 300 g containing 150 mg head grade of silver.

5.3.3 *Effect of Temperature*

With respect to the influence of temperature on the coarse particle dissolution kinetics of gold/silver ores, a number of investigations have revealed that an increase in temperature results in increased reaction rate and extraction (*Habashi, 1967; Bouffard & Dixon, 2007, Hlabangana et al., 2018*); it is reported that increase in the temperature reduces reagent solution viscosity and promotes diffusion (*Esmkhani et al., 2013*). However, the present study revealed that an increase in the temperature of the solution did not improve extraction for the selected fractions (*Figure 5.9*). Although the extraction of silver was low, increasing the temperature resulted in sudden retardation in the silver dissolution.

One possible explanation for this behaviour suggest that it is due to the decrease in the solubility of oxygen in cyanide medium at elevated temperatures. Furthermore, samples withdrawn periodically from the batch tests were not replenished with a solution containing fresh dissolved oxygen and free cyanide. This low extraction influence of silver extraction with respect to increasing temperature corresponds to (*Wilkomirsky et al., 2010*) where the extraction of metallic silver was maximum at 25 °C but retarded as the temperature was increased (i.e. to 45 °C and 65 °C). The authors moreover reported that at high temperatures, silver attains stronger polarization resulting in the reduced dissolution of the metal.

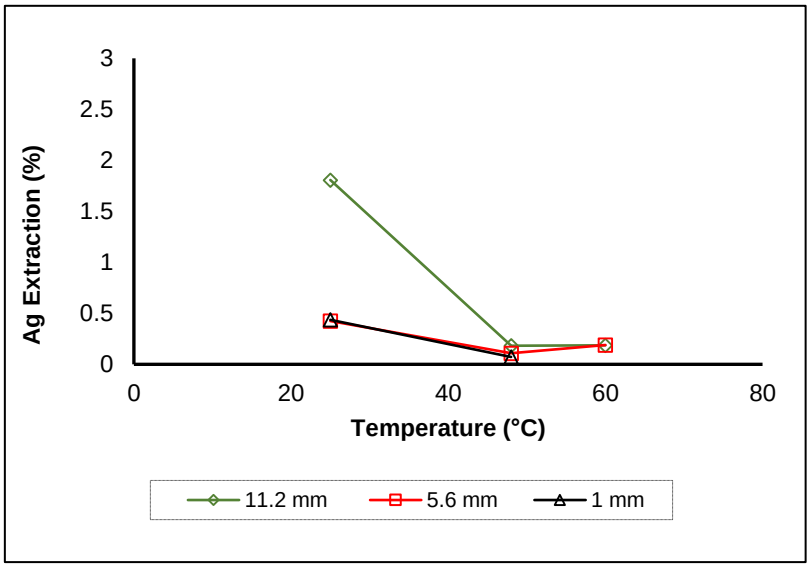

Figure 5.9 Influence of the dissolution recovery of silver at vary particle fraction (-16/+11.2 mm, -8/+5.6 mm, & -2/+1 mm) as a function of temperature at ~107 hours of reaction time in 275 ppm of NaCN solution.Temperatrue test was not performed at 60 °C for the -2/+1 mm class fraction.

Additionally, it is worth mentioning that coarse particle leaching is invariably inhibited by pore diffusion; however, due to the similar trend with respect to temperature influence in the pure metal dissolution (*section 5.2.4*), pore diffusion was not considered to be primarily an inhibiting factor for this aspect of temperature effect, but contributed to the low extraction in the coarse particle dissolution process.

The extraction in the pure silver leaching was optimum at 48 °C; however, the coarse particle experiments exhibited higher extraction at 25 °C. The effect of temperature results in relation to the two studies was inconclusive.

Although this work has different result to what is an expected trend in gold/silver dissolution, grains of silver in the ore in this work and in *Wilkomirsky et al., 2010* were particulates tested at similar temperatures

and produced similar trend in the results. This suggest a need for further investigation but such is beyond this study.

With the leaching performance on the dissolution of both pure silver and synthetic coarse silver ore observed in this study and the fact that gold/silver dissolution normally proceed at ambient temperatures, in any event, 25 °C operating temperature and 275 ppm sodium cyanide concentration are two optimal parameters selected to be used throughout this project for the CF-FBR and all the column leaching experiments. Coarse synthetic silver extraction data are provided in ***Appendix V .a-c.***

5.3.4 *Silver Extraction using CF-FBR*

In order to deepen the investigation, unpacking the factors associated with silver extraction in the leachant solution, another coarse particle leaching approach, using the circulating fluidized fixed-bed reactor (CF-FBR), was initiated. The CF-FBR operates as a CSTR with agitation controlled by the bubbling of air from the bottom of the reactor through a central shaft, drawn down through a set of baskets containing the ore, thus effectively suspending them in solution (*section 3.4.2*). Leaching ran at conditions of 25 °C temperature with cyanide solution of 275 ppm concentration. The CF-FBR operated in continuous mode with a throughput flow rate of 50 mL/hr and the air was bubbled at a rate of 0.27 vvm. Duration of the experiment was about 17 days. While the leaching using the CF-FBR was used to validate leaching extraction of the large synthetic ore particles observed in the shake flask experiments, the progression of leaching into the inner core of the particle using XCT was investigated on selected particles with respect to pore development and metal dissolution. The CF-FBR test work consisted of four columns of which contained four selected size fractions (-19/+16, -16/+11.2, -8/+5.6, -4/+2.8 mm).

5.3.4.1 *Recovery of Silver*

The dissolution of silver using the CF-FBR depicted in *Figure 5.10* shows significant extraction over a period of about ~ 17 days of leaching compared to the shake flask (~4.5 days). The extraction curves of the CF-FBR in the leaching from large synthetic ore particle exhibited an initial slow dissolution rate that was followed by a gradual increase.

Leaching extraction of silver after ~ 17 days in the leachant liquor was highest for the smallest particles and decreased in the larger particle effluent solution. This is anticipated due to reason that a given mass of smaller particle has a higher exposure of metal grains to lixiviant solution compared to the same mass of larger particles. Furthermore, at a given penetration depth of smaller particles, more of the total particle volume is connected to the nearest surface rather than large ones making the region readily accessible to

penetrating lixiviant solution. This trend is in agreement with the dissolution of gold/silver ores in other studies (*Bouffard & Dixon, 2007; Bartlett, 2013*).

Curves of cumulative dissolution of silver in the leachant solution in *figure 5.10* indicate the extent of leaching in each particle fraction. The smaller size fractions show a continuous increase in a more or less linear fashion. This trend indicates that mineral conversion at the particle surface was readily dissolving over time. Although the dissolution rate was low, partial conversion of the metal into the bulk solution was achieved with an expected extraction trend, unlike the shake flask investigation. The cumulative curves for the larger particles are levelling off, indicating a slowing of extraction, whereas the smaller ones were observed to stay linear, indicating a quasi-steady-state extraction. The slowing down of the dissolution for larger particles demonstrates inner particle diffusion leaching effects. This was expected in the large particles.

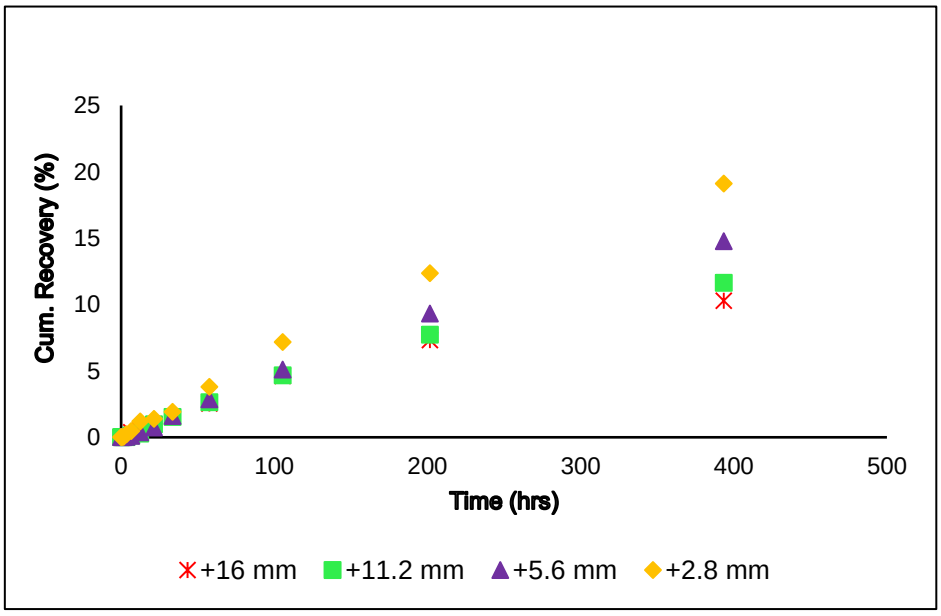

Figure 5.10 Cumulative extraction curves of selected coarse synthetic particles leached using the CF-FBR at 25 °C and 275 ppm NaCN

Over a longer period of leaching, extraction from the smaller particles is anticipated to reach complete conversion at which time the cumulative extraction should come to a stop. It must be noted that while all particles will eventually achieve complete dissolution, the smaller particles achieve faster conversion as all the silver present in shallow depths are dissloved from the particle surface, whereas in the large particles the lixiviant has to diffuse much deeper into the ore and hence leaching will appear much slower.

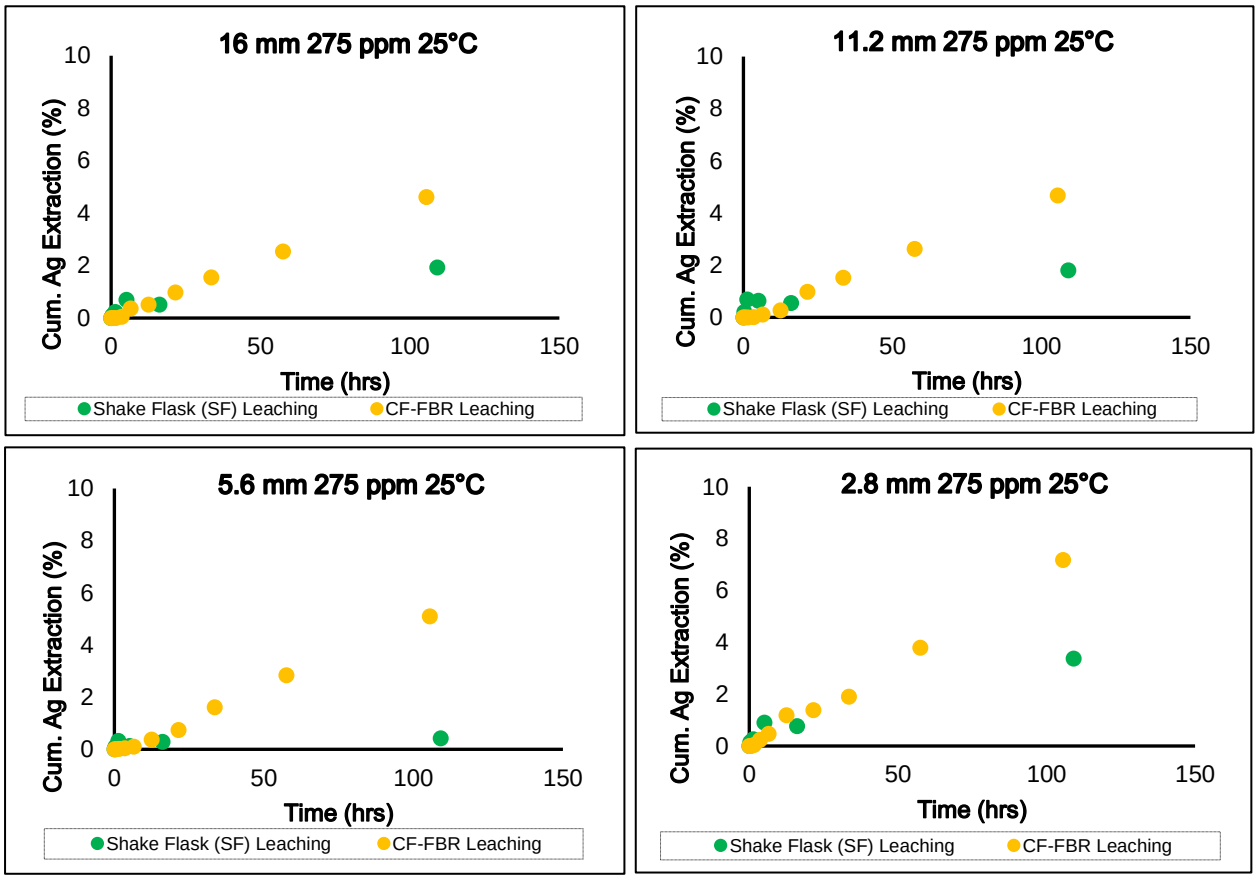

Figure 5.11 Comparison of coarse synthetic silver ore shake flask and CF-FBR extractions leaching for about ~4.5 days at 25 °C and 275 ppm NaCN on selected particle fractions of 300 g for each class.

In an effort to elucidate the effect of the influencing factors limiting extraction dissolution of silver from coarse ore particle, *figure 5.11* shows the comparative extraction of silver observed in both shake flask (SF) and circulating fluidized fixed-bed reactor (CF-FBR) leaching experiments. The leaching conditions were kept similar using selected particle fractions, feed weight, and head grade.

Coarse particle silver extraction in the shake flask experiment (performed for about ~4.5 days) was marginal compared to the dissolution of silver observed in the CF-FBR leaching. CFFBR data demonstrated a much better extraction and solution distribution.

The improved extraction observed in the CF-FBR leaching compare to the SF leaching is attributed to the mode of operation. Unlike the shaking flask technique, the CF-FBR operated in continuous mode where fresh feed solution containing free cyanide and oxygen was pumped with vigorous agitation by the use of compressed air to circulate the solution through the reactor at constant temperature (25 °C) and NaCN concentration (275 ppm). By comparison, the SF was kept at a constant volume (batch) closed in a shaking incubator; during the long periods of leaching corresponding to the sampling interval, it was perceived that solubility of oxygen decreased starving the solution of oxidant to aid dissolution.

5.3.5 ***Data-to-Models***

Several leaching models to predict mineral conversion in coarse particle heap leaching have been formulated (*Levenspiel, 1999; Bouffard 2003, Ghorbani et al., 2013*). These models developed have been able to predict mineral conversion for potential heap characterization. However, it is pivotal to note that particle size variability and inconsistent mineralogy from ore to ore in heap operations thus influence the models. While this study is not extended to model development, data obtained from experiments are applied to models have proven to be deterministic in providing the most probable conversion and extraction mechanism. The shrinking core model (*Levenspiel, 1999*) and extended mixed topology model (*Ghorbani et al., 2013*) are utilized in this study to establish the leaching and mineral conversion of silver from large particle synthetic silver ore.

5.3.5.1 *Shrinking Models*

Hydrometallurgy leaching process of gold /silver ores is a heterogeneous process involving solid-liquid-gas phases comprising physical, chemical, and biological phenomena depending on the type of ore amenable to the desire leaching approach; i.e. sodium cyanide leaching on low-grade gold/silver oxide ores and microbial attack on refractory low-grade gold/silver ores. The shrinking core model is one deterministic tool to describe the physical phenomena of the leaching process. This modelling tool is used to determine the dissolution mechanism of the kinetic dissolution reaction of metals from ores. The model predicts whether the reaction is entirely governed by diffusion through the product porous matrix or chemical reaction controlled. It describes the leaching reaction taking place from the surface of the particle into deeper regions as the reaction progresses from the external surface, leaving a surrounding inert ash layer; i.e, the reacting core shrinks while the particle size remains constant. Due to the presence of liquid and

solid interfaces in the leaching, the process is controlled by different steps of the interaction between the phases through an associated shrinking core with the overall rate of the process being determined by the slowest step (*Levenspiel, 1999*).

When a system experiences a fast chemical reaction at the surface of the mineral, the flow of the reagent solution diffuses normal to the surface of the solid particle. This process results in the dissolution of the metal to be dependent on the time of diffusion to occur; hence the slowest step. On the other hand, when the reaction at the surface of the particle is slow as compared to the time of diffusion into the solid particle, the process is limited by chemical kinetics of the reaction. The corresponding kinetic expression are listed in *Table 5.4,* where *kr, kd,* and *kf* represent rate constants and *X* represents the fractional conversion of the dissolved silver relative to the total silver content.

Table 5.4 Shrinking models

Controlling step	**Shrinking core model equation**
Diffusion through liquid film	$k_f t = X$
Diffusion through ash layer	$k_d t = 1 - 3(1 - X)^{2/3} + 2(1 - X)$
Chemical reaction	$k_r t = 1 - (1 - X)^{1/3}$

According to *Ghorbani (2012),* the model describes a system of leaching from large particles that is controlled by chemical kinetics at the surface of the particle when exposed to reagent solution, combined influence of reaction-diffusion governing mechanism (predominantly diffusion at high concentration gradient of the reagent) as lixiviant ingresses the particle subsurface, and a final stage in the inner particle core where both reaction and diffusion influence on the leaching of large particle is reduced. *Ghorbani, (2012)* further proposed that a scenario of the latter mechanism most likely results in a linear relationship between mineral dissolution and time.

It is worth noting that while the model has been widely used to predict the kinetics of mineral dissolution for comparative analyses of the governing dissolution mechanism, the technique has one drawback limiting the tool to single-particle size at an operating condition. However, using this tool will require narrowed particle class fractions for accurate measurement of parameters. Furthermore, assumptions that are made using the shrinking models that make it less efficient in predicting mineral conversion and controlling mechanism in naturally occurring mineral resources include the requirement for homogeneous porosity and uniform dispersion of mineral distribution in the particle. It can be pointed out that the production of the synthetic silver ore in this investigation sought to achieve similar ideal characteristics. These aspects were assessed in *Chapter 4*.

With the application of the shrinking core model to extraction data, it is assumed that the particles are spherical and the class fraction is homogeneously fixed at a single particle size. Due to the inconclusive and poor extraction performance in the shaking flask experiments, extraction curves predicting the dissolution of silver extraction from coarse particles were analysed using results from the circulating fluidized fixed-bed reactor experiments illustrated in *Figure 5.12*.

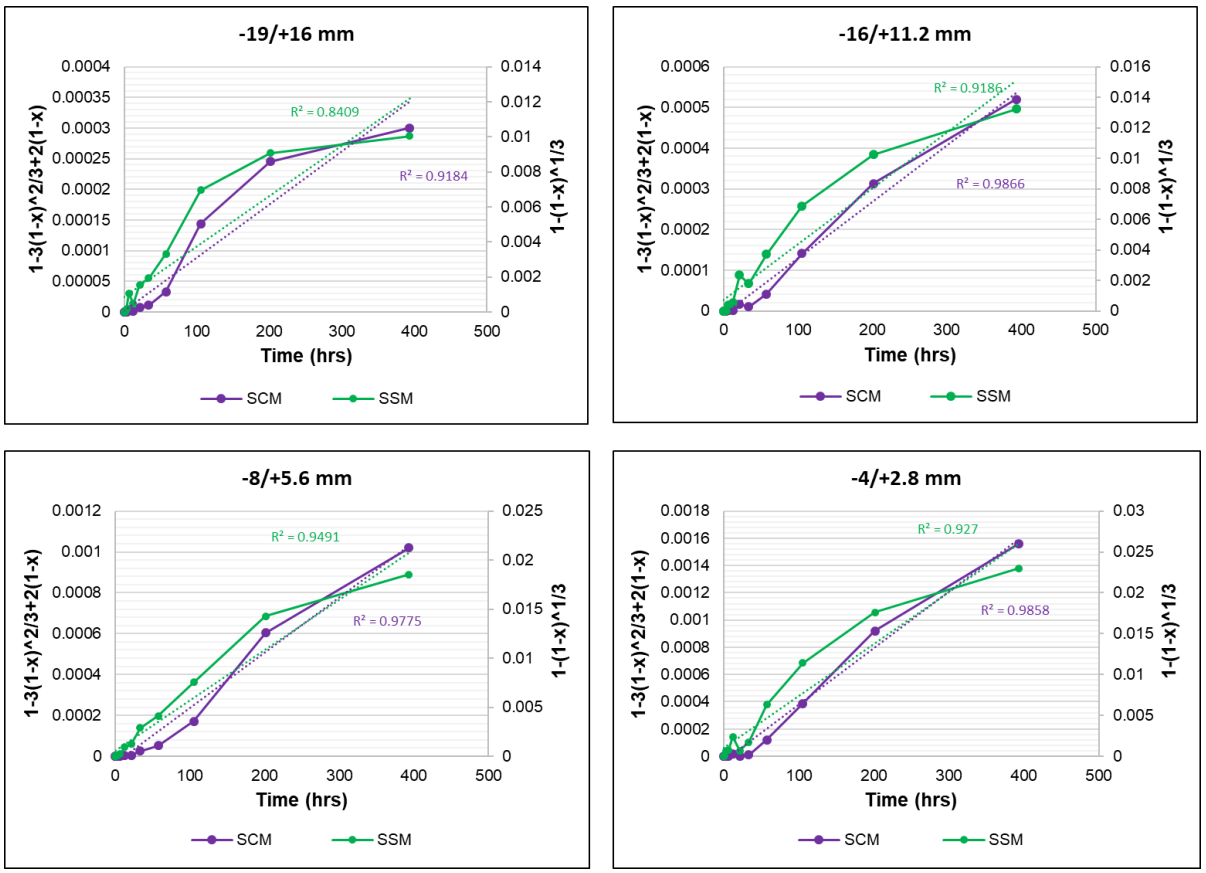

Figure 5.12 Illustration of the shrinking core model and shrinking sphere model of selected particle size fractions from the circulating fluidized fixed-bed reactor experiment at 25 °C and 275 ppm NaCN.

The deterministic tool revealed that the shrinking core model (SCM) in *figure 5.12* gives a better linear correlation of silver extraction. Thus suggesting that the mechanism was governed by diffusion of the NaCN lixiviant from the external surface of the reaction site into the shallow sub-surface of the large particles. Evident from the dissolution rate and overall extraction observed in previous sections of this chapter, extractions were low. Although the extraction of the metal was slow, the kinetic controlling shrinking sphere plot demonstrated more variability during the initial leaching stage than the diffusion governing curve. This suggests that the both drawn for the diffusion and reaction kinetics revealed that the limiting mechanism for the leaching of the selected coarse particle fractions was most likely governed by diffusion than the surface reaction controlled shrinking sphere model. It is noteworthy to acknowledge that

the shrinking models in *figure 5.12* do not completely follow the dissolution of the experimental data. This is possibly due to poor data resolution from the mineral conversion during the leaching.

As reported earlier in *section 5.2*, the reaction kinetics of pure silver was inhibited by mass transfer constraint at the grain-lixiviant interface; hence the corresponding diffusion controlling mechanism of the metal from large ore particles predicted by the SCM suggest that the extraction was impeded by mass transfer constraint at both the grain and particle levels.

5.3.5.2 *Extended Mixed Topology Model*

In heap leaching, lixiviant solution ingresses to the inner core of the particle through the available pores and crack network (usually in the scale of microns and smaller). These voids and sub-micron channels become narrower and less frequent with depth into the core of the particle. Solutions bearing high concentration of fresh feed (NaCN) in the flow experience significant contact time exposed to metal grains along these paths; thus, becoming depleted of available reagent (free CN) in solution. The subsequent flow of feed make-up solution containing fresh lixiviant from the bulk flow enhances extraction from the reagent depleted zones. At this point of metal extraction in the coarse particle, the dissolution mechanism becomes indeterminate, resulting in a mixed reaction-diffusion controlled process. This phenomenon was formulated by (*Ghorbani et al., 2013*) who observed and proposed the extended *K-phi* model enhancing the mixed topology model by *Bouffard (2003)* to predict extraction of leaching progression into large particles. Detail of the model formulation is provided in the literature (*Ghorbani, 2012, Ghorbani et al., 2013*).

With an initial assumption that spherical particle size, temperature and chemical conditions of the kinetic dissolution from the coarse particle are constant, the simplified extended mixed topology model describing the extent of leaching is as follows *Eq 5.6* (*Ghorbani, 2012*):

$$\frac{dx}{dt} = k(1 - \frac{X}{\alpha})^{\varphi} \qquad \textit{Eq. 5.6}$$

where X is the mineral conversion of silver relative to the total content of silver in the ore fraction, a is the readily leachable (non-occluded) fraction of silver in the ore, φ is the effective distribution of silver grain size throughout the particle, K is the corresponding initial rate of mineral dissolution at the particle surface, and t is the time observed for mineral conversion.

Hence, integrating the intrinsic rate of mineral conversion over the leaching duration, *equation 5.6* will take the form of *equation 5.7*.

$$X(t) = \alpha \left[1 - \left(1 + (\varphi - 1)\frac{Kt}{\alpha}\right)^{\frac{1}{1-\varphi}}\right] \qquad \textit{Eq. 5.7}$$

Where, $\varphi \neq 1$.

It is noteworthy to point out that the extended mixed topology and shrinking models have a common drawback of single-particle size utilization in determining the mineral conversion. In the practice of heap leaching technology, leaching at mono-size particle feed is not feasible. Extraction is improved with an effective distribution of particle size fractions in the bed. Therefore, in order to utilize the available models to predict leaching dissolution of minerals from large particles, the use of a narrow class fractions (taken at the average diameter of the upper and lower bounds of the fraction) is considered (*Bartlett, 2013).* Hence, while assuming spherical particle size, application of the extended *K-phi* model was achieved by considering selected individual class sizes as in the case of the shrinking models.

Experimental data from the leaching extraction of silver from selected artificial coarse ore particle fractions were fitted to the extended mixed topology model for large particle leaching using *equation 5.7* and curves predicting reaction-diffusion dissolution mechanism are illustrated in *Figure 5.13*. The values of *K, phi*, and *alpha* obtained from fitting the extraction data by minimization of the mean square error (MSE) are presented in *Table 5.5*; while model and silver extraction data are given in ***Appendix V.d.***

Table 5.5 Values obtained for α, φ, and K for each particle fraction utilized in the CF-FBR

Particle Size (mm)	Alpha (α)	Phi (ϕ)	Rate Constant, K (hr^{-1})
-19/+16	0.12	0.85	5.14E-04
-16/+11.2	0.15	0.87	5.30E-04
-8/+5.6	0.23	0.88	5.74E-04
-4/+2.8	0.30	0.87	7.33E-04

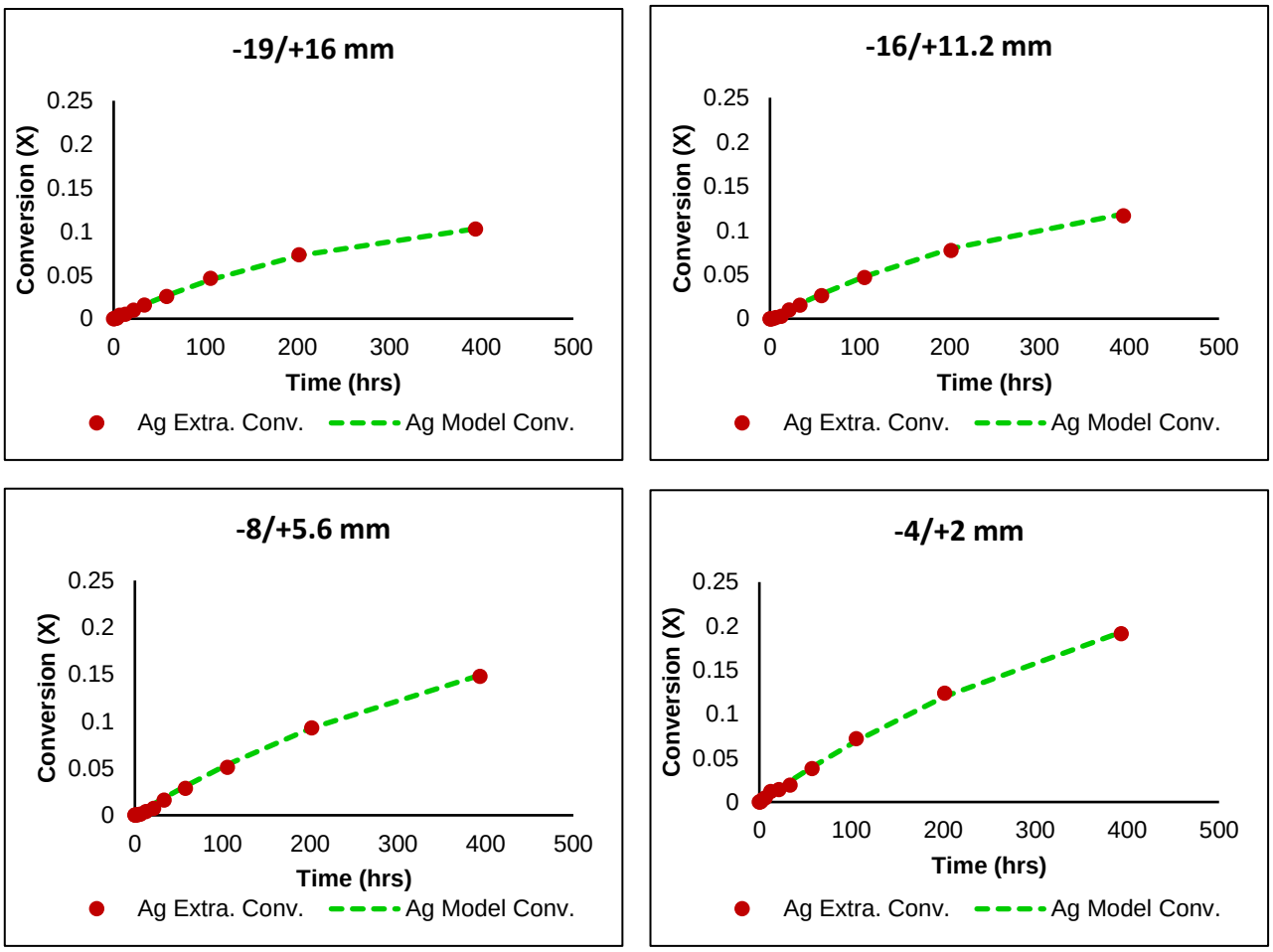

Figure 5.13 Coarse synthetic silver ore dissolution using the extended K-phi model on selected feed particles leaching at 25 °C and 275 ppm NaCN using the CF-FBR setup.

From the parameters obtained, alpha (*a*) varied with particle size. It exhibited a trend of increasing values with a decrease in the size class fraction of particles. This is evident due to the reason that larger particles have more silver grains that are occluded in the matrix whereas the smaller class fractions have more grains expose to the lixiviant. This is in agreement with *Ghorbani et al., (2013)* in the leaching of Zn. The leachable fraction (*a*) is dependent on the accessibility of the silver grains in the particle to NaCN through available pores and fractures. It was observed that the leachable fraction proportionally increased with the dissolution rate of the targeted metal with respect to decreasing the mean radius of each class fraction. It can be noted that the leachable fraction does not depend on the rate kinetics but describes the extent of extraction possible in a given particle radius.

The low quantity of *a* from the experimental data describes the leaching subjected to dissolution occurring most likely at the near-surface where the metal grains were exposed. This low value of the leachable fraction observed is probably owing to a large number of silver grains being occluded in the concrete. Alluding to the grains characterization (*Chapter 4*), only fewer grains were observed at the surface or near surface regions

of the particles (*see* ***Appendix III.c***). This was evidently corresponded by the recovery observed in the CF-FBR leachant solution (*see Figure 5.10*).

The mean value of Phi (φ) was ≈ 0.87 and did not significantly vary with particle size. It is worth noting that in the application of the extended *K* - *φ* model, the maximum attainable value of φ possible is always less than 1 (*Ghorbani et al., 2013*). This therefore drives the conclusion that the relatively high and similar result of the effective mineral distribution (φ) across the selected class fractions correspond to one of the ideal properties this study achieve; i.e. uniformly dispersed metal grains throughout the ore fractions - irrespective of the crushed size class – with a significant proportion located below the near surface extending into the particle core.

In relation to the global slow rate of silver dissolution of leaching from the synthetic coarse particles, *K* illustrates a low apparent rate of extraction in all size fractions. The value of *K* describes the corresponding initial apparent rate of dissolution and it was observed to increase with a decrease in the particle size. The trend is attributed to the fact that higher specific surface area of metal is exposed as the mean particle radius is reduced.

As described by *Ghorbani et al., (2013)*, the *K* value obtained from the extended model plotted against the mean radius produced a power relationship that was utilized in comparing the rate parameter to the dissolution of the metal with respect to cracks established on the selected size fractions by different modes

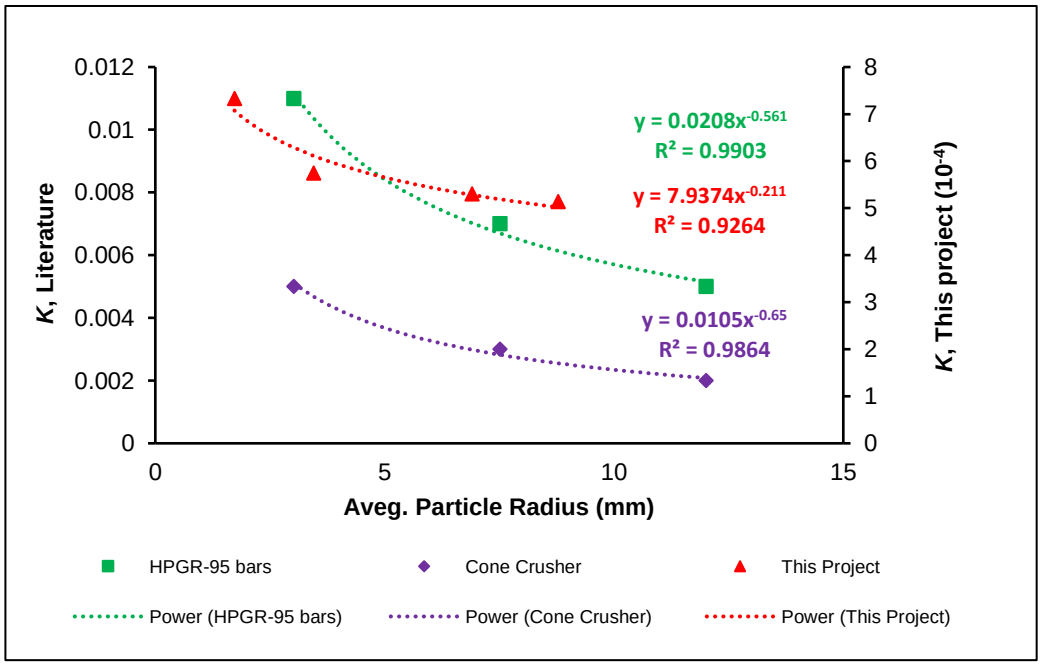

Figure 5.14 Relationship between the rate constant (K) and the average particle radius (R) comparing results from this project to results adorpted from Ghorbani et al., (2013).

of comminution. *Figure 5.14* demonstrates a power relationship (*Eq 5.8*) between the apparent rate constant (*K*) and the average particle radius (*R*) prevails also in the current study.

$$\boldsymbol{K = gR^{h}} \qquad \textit{Eq. 5.8}$$

Although the performance of comminution media and quantifying the extent of leaching ingress into the particle depth were not considered in this project, the very low value of $\boldsymbol{g}$ from *equation 5.8* in *figure 5.14* of this investigation compared to the results of literature suggesting that the low rate constant was the result of inhibition by the lack of a sufficient crack network to facilitate leaching into the inner sub-surface of particles. Thus, a reaction-diffusion controlling mechanism occurring at the near-surface region of the coarse synthetic silver ores instead of operating at the core of the particles.

It is noted that while a critical aspect for a meaningful use of the shrinking models to determine the leaching mechanism from large particles is that the mineral conversion should be > 50 %, the extended topology model revealed similar prediction in terms of the reaction-diffusion dissolution mechanism as did the shrinking models despite mineral conversion extraction data of < 50 %. The extended topology model further reveals that mineral conversion most likely only occurs at the near surfaces of the selected size fractions evident by the values obtained for the leachable fraction.

5.3.6 *Coarse Particle Leaching – Porosity Effect*

After the full leaching duration (~17 days) of the CF-FBR, XCT defects analysis revealed that a marginal increase of approximately 0.1 % total voidage was achieved.

Particle porosity has the likelihood to increase depending on the type of lixiviant utilized in the metal extraction process. Unlike acid leaching, where the rock matrix is disintegrated (with the extent of degradation depending on the acid concentrations) such that it allows the leaching solution to proceed into the inner core of large particles readily over long leaching periods (*Ram et al., 2020*), the alkaline leaching of gold/silver ore using sodium cyanide lixiviant is not sufficiently aggressive to induce additional pores. Although the literature suggests that leaching in acidic media typically lasts for about 200 days, it is worth mentioning that pores in the artificial particles would not significantly widen even if the cyanide leaching process lasted for longer periods. Thus, the marginal increase (~0.1 %) observed in the porosity of the artificial ore is perceived to be the maximum possible, which clearly is insignificant relative to the over all porosity.

In cases of material (metals) being locked in the inner core of the particles, longer leaching periods would be required to achieve metal dissolution through micro-porous fissures; but this would result in marginal inherent porosity change as the grains of the silver metal are microscopic.

Leaching of the coarse synthetic particle, and large particles in general, is limited by diffusion inside the particles, unlike exposed surfaces. Thus, it is postulated that diffusion was more restricted in the artificial silver ore. This may have contributed to the inefficiency of the metal extraction process, considering the leaching duration was only ~17 days.

5.3.7 *Effect of Leaching on Grain Dissolution*

In the determination of metal extraction with respect to the silver disappearance using XCT defects, a region of interest (ROI) was primarily targeted. Though the orientation of scans was maintained throughout, achieving an accuracy of the manual count of grains for every scan was not trivial. Quantification of silver grains was obtained from grey values distinguishing the higher values for the metal from the lower matrix values. Determining metal extraction using XCT was not possible. This challenge was ascribed to the lack of significant alteration observed on the visible grains, or disappearance of smaller grains on a particular tomography slice, as illustrated in *Figure 5.15*.

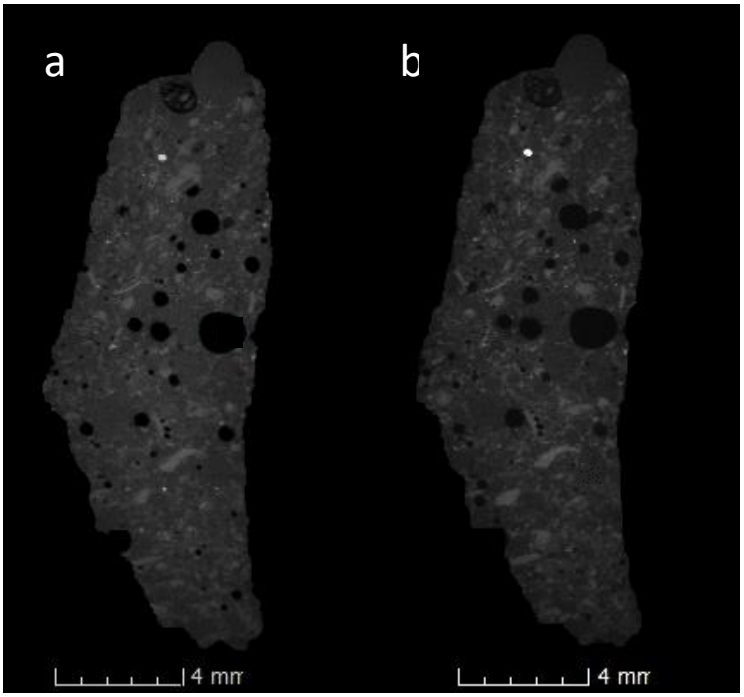

Figure 5.15 Reconstructed image comparison of 0 hr (a) scan and 192 hr (b) scan of 5.6 mm particles illustrating little or no significant change in terms of silver grains disappearance or size reduction scanned at 20 μm resolution

The 20-micron scanning resolution was seemingly too low to have detected the dissolution of very small grains in the assessment of solid extraction. Moreover, the leaching kinetics of silver was not rapid over the short experimental duration, resulting in marginal extractions that could not be reconciled using the XCT defect analysis across each sampling interval. Evident in *Figure 5.15* – indicating the initial (0 hour) scan before leaching and final (192 hours) scan after leaching – it is clearly obvious that these two slices do not reconcile judging by the slight orientation of some pores. The inconguence is larger than the average grain size, hence, it is impossible to trace the disappearance of particular grains at this scale.

The characterization of crack network distribution in large ore particles remains a crude approach despite serious attempts to categorize and visualize fractures created by crushing and leaching over time *(Ghorbani, 2012)*. Using the XCT characterization technique is promising; however, sub-level micro-fractures remain challenging to quantify. One reason could be attributed to the resolution of XCT; however, even with the high-resolution synchrotron X-rays, this remains elusive (*Yang et al., 2019*). Thus, XCT is ultimately not a reliable way of analyzing the extent of leaching over relatively short leaching duration. Even for a longer leaching period, the solid extraction is underestimated compared to the liquid PLS extraction (*Ghorbani et al., 2013*).

What has been distinguished to improve coarse particle metal extraction is the ability to determine optimum crushing parameters and selected crushers efficiency to induce maximum internal fracture that is a function of leaching from large particles *(Ghorbani et al., 2013; Nwaila, 2014)*, but XCT is not a critical tool in this assessment.

Although the solid metal extraction from XCT data in this investigation was not possible, PLS from scanned particles leached in the CF-FBR suggests that extraction was promoted by readily available surfaces of coarse particles (*see Figure 5.10*). The low PLS extraction concords with the postulation that very small grains and edges of large grains exposed to the solution were dissolved and extracted.

With the information obtained from the dissolution of pure silver metal and the artificial ore containing grains of silver, the reaction characterization studies have provided useful parameters for the assessment of the leaching behaviour of the metal in a heap/column leaching scenario.

6 RESIDENCE TIME DISTRIBUTION TO ASSESS THE FLOW TYPE PERFORMANCE OF PACKED BED COLUMN REACTORS

6.1 Introduction

An investigation of the residence time distribution of fluid permeating through packed bed column reactors using conventional inert tracer and reactive leaching techniques were carried out under similar conditions. The chapter seeks to advance the understanding of solution flow through packed bed systems with respect to extraction performance. This was done with a view to establishing flow types in the packed bed and to be able to compare the silver leaching extraction to nonreactive tracer response curves to determine what could possibly be responsible for a multi-channel plug flow system to produce a CSTR well-mixed flow performance.

The results and discussions in this chapter evaluate fluid residence time and reaction extraction. The influences of flow rate and particle size distribution on the residence time of inert (non-reactive) tracer and the reaction dissolution from the homogeneous ore at similar packed bed conditions are presented. Relevant simplified models are introduced to diagnose the flow phenomena in the column reactors.

6.2 Influence of PSD on Bed RTD

The influence of artificially blending a distribution of particles packed into a column bed was studied. Hydrodynamic behaviour of packed bed leaching performance of each column based on different particle size distributions is presented and discussed. As mentioned in *Chapter 3*, the particle size distribution used throughout this investigation were artificial blends described according to the *GGS-PSD* model, with the exception of the 0.721 blending distribution coefficient (BDC) which represented the true PSD of the as-crushed synthetic silver ore. Columns were irrigated at constant flow rate (6 L/m^2/h) while each column was characterized with specific BDC (0.25, 0.5, 0.721, & 1).

As mentioned (*chapter 3*), flooding or washing of the loaded columns was carried out to reduce the significant background potassium concentration (about 1~2 g/l) from the ore bed. Potassium easily dissociates and is very soluble in water; hence, the washing approach was successful in achieving initial effluent concentration of about 1.5 ~ 54 mg/l prior to introducing the inert tracer (KNO_3) at 1 g/l potassium concentration.

During the flooding, each bed experienced some degree of slumping and increase of bulk density (*see Table 6.1*). Initial paths in the multi-channel packed bed were potentially established during the flooding stage

prior to the RTD investigations. This may have resulted in wetted paths in the particle micro and macro clusters. Although the columns were left to dry for two days, the beds did not become completely dry but assumed to have retained moisture around 10 % water content, maintaining these created preferential paths (*Cherkaev, 2019*).

Table 6.1 Parameters of slumping and bulk densities for each PSD

BDC (*m*)	Slump (%)	Bulk Density (t/m³)	
		Initial	Final
0.25	3.57	1.55	1.58
0.5	3.09	1.34	1.36
0.721	2.97	1.30	1.31
1	2.92	1.27	1.29

6.2.1 *Conventional Non-Reactive RTD*

The step-change tracer approach was initiated by introducing the KNO_3 feed solution and irrigating the packed beds while monitoring the effluent solution for the build-up of the K^+ concentration until the initial inlet concentration was reached in the outlet solution. Both step-up and step-down inert tracer experiments were performed. Tracer data obtained from the effluent discharge concentration was normalized with respect to the feed concentration in the step-up tracer test; while in the step-down tracer experiment, the peak concentration attained in the column reactor during the step-up was utilized in normalizing the effluent concentration. Normalizing the tracer concentration bounds it in the dimensionless range of 0 to 1 for representation as a typical residence time *F-curve*.

The minimum concentration of the potassium obtained in the effluent after flooding was added to the maximum concentration utilized during the normalization of the *F*-curve. For example, a column with 0.721 BDC had an initial potassium background concentration of 42.5 mg/l prior to application of the feed solution; hence, 1042.5 mg/l K^+ was considered as the peak concentration for the step-change RTD analysis. Tracer experimental data are provided in ***Appendix VI.a***.

RTD studies of varying the PSD coefficient and incurring influences on the column packed bed were investigated. *F-* and *C-curves* of the nonreactive inert KNO_3 tracer are discussed and compared with the reactive solid extraction data for interpretation. Inert tracer *RTD* curves of all varied PSD are shown in *Figure 6.1*.

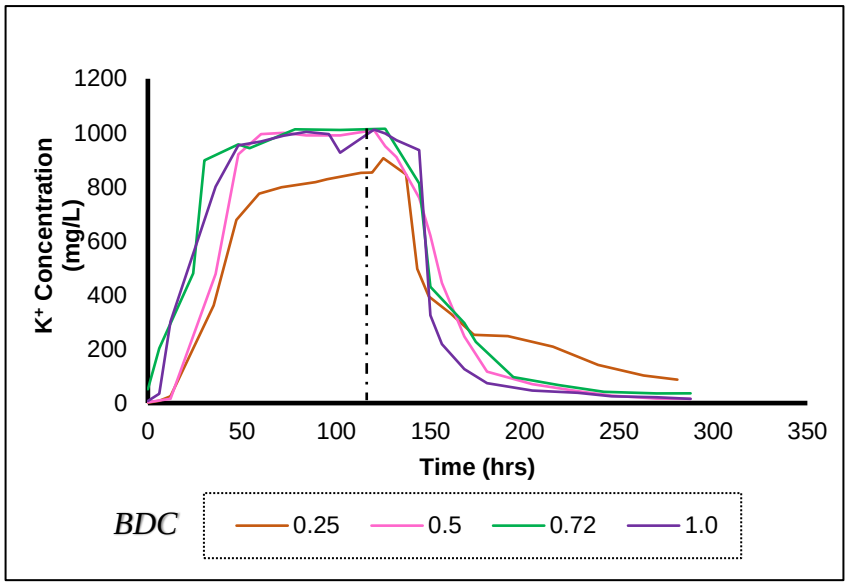

Figure 6.1 Concentration profile of the KNO_3 non-reactive tracer for columns with varying GGS particle size distribution coefficient (m) at 6L/m²/h. Dotted lines indicate the start of the step down.

It can be recalled from *Chapter 3*, that the lower BDC suggests a higher component of fines (<1 mm) in the reactor. The weight percentage of fines is presented in *Table 6.2* for the respective distributions coefficient depicted in *Figure 6.1*. Full column PSD weight distribution data is provided in ***Appendix II.***

Table 6.2 Weight distribution of fines (<1 mm) in each column artificial blend.

m	**wt %**
0.25	47.90
0.50	22.94
0.72	11.97
1.00	5.26

The measured concentration profiles of *Figure 6.1* illustrate a major distinction of different residence times between beds of 0.25 BDC and the next larger value of 0.5 BDC; while at distributions 0.5, 0.72 and 1.0 no significant differences were observed in terms of the tracer time spent in the column. All the BDCs, with the exception of 0.25, attained the maximum tracer concentration as the input feed concentration after the period of the step-change (step-up); however, this was not the case with the bed containing 0.25 BDC. A spike was observed after about a period of 125 hours when the change to step-down was initially performed.

It was assumed that at that point reagent solution emanating in the effluent stream was gradually reaching the maximum concentration level similar to the feed concentration as did the experiments at the other

BDCs. This ultimately suggests that bed permeability was lower, resulting in longer times for the tracer reagent to migrate through convoluted channels in the packed bed. The trend of a higher portion of fines resulting in longer residence time observed was expected; this is in agreement with (*Cherkaev, 2019*).

The initial flooding conducted prior to the RTD investigation eventually contributed to bed compaction in all the column investigations. The effect was most profound in the 0.25 BDC due to the fact that particle composition of the bed consisted of ~ 48 wt% fines. Compared to the 1.0 blend, where fines composition was only 5 wt%, residence time was anticipated to be longer in the 0.25 BDC.

Concentration profiles were transformed into a step-down tracer RTD *F-curve* (*figure 6.2*) to further understand and interpret the influences of varying BDCs on solution residence time in the packed bed. The step-up data points were not used in the RTD analysis due to the fact that the step-down stage shows better data resolution than the step-up stage.

The step-down was performed after 124 hours of irrigation. *Figure 6.2* shows that an initial lag was observed after the step change. This induction period of 40 hours indicates that there was a delay of tracer concentration drop in the effluent solution of all the columns. The trend is believed to elucidate the exchange of occurrence between flowing and immobile phases of the tracer paths. This performance was expected as there exists no mixing in the multi-channel plug flow system and diffusion is highly possible through stagnant pores.

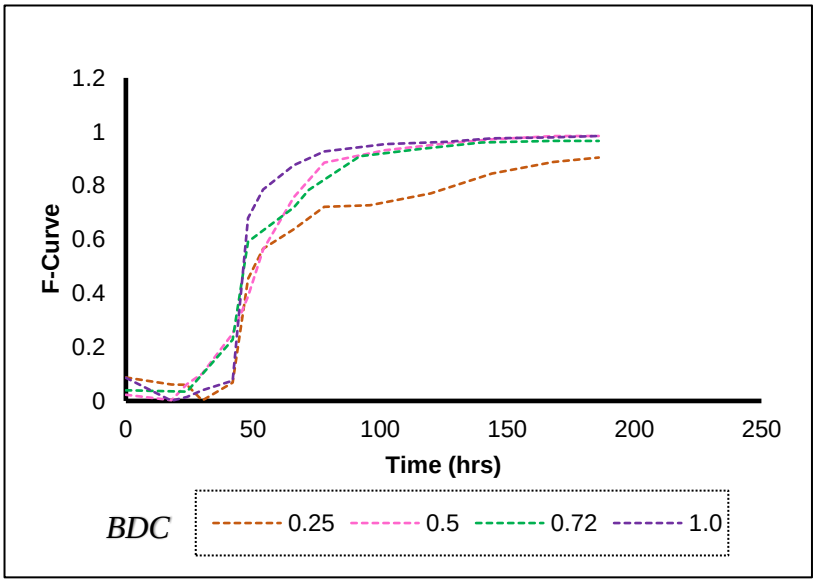

Figure 6.2 Inverted normalized step-down RTD profile of the non-reactive tracer for columns with varying GGS particle size distribution coefficients (BDC).

The *F-curve* of *figure 6.2* demonstrates that residence time depended on the amount of fines deportment in the packed bed. The characteristic long tail of the RTD curve was indicative of fluids emanating from stagnant zones in the bed. This is expected from column beds with such a high composition of fines as a result of more of the smaller particles filling the macro interstices between fewer larger ones, that possibly occurred during the flooding intervals. Pore radii between particles in the bed are assumed to be substantially narrower, consequently impeding rapid reagent solution percolation; hence, lower bed permeability results.

Both *Figure 6.1* and *Figure 6.2* reveal that the 0.5 and 0.721 blending distribution coefficients apparently had marginally different influence on the time the tracer spent in the reactor. The indistinguishable RTD performance between the two blends is fairly plausible due to fact that the weight distribution of particles across the crushed fractions in each bed was not significantly different except for the -1 mm class which was about 2 times more in the 0.5 blend (*see* ***Appendix II***). Thus a narrow PSD exhibits a marginal difference in the RTD response. This phenomenon is also alluded to in the work of *Cherkaev (2019)*.

It is perceived that subsequent compaction during flooding was only local rearrangement in the different column blends, not large-scale migration. It is revealed in this study that residence time is dependent on the particle size distribution of the packed bed.

6.2.2 *Column Extraction*

Homogenous synthetic silver ore was used in this study to ultimately explore the possibility of using metal extraction to elucidate the column RTD flow type performance.

The influence of varying the distribution of particle size with respect to the reactive leaching investigation was performed on the same packed beds following the nonreactive tracer studies. At this point, the feed solution was changed to the sodium cyanide reservoir containing 275 ppm concentration conditioned at pH 10.5~10.8 and flow rate was maintained at 6 L/m^2/h. The investigation was performed for a duration of 12 days (288 hours).

Figure 6.3 and *figure 6.4* shows the concentration profiles and cumulative recovery, respectively, of the varying PSD coefficients as it relates to the dissolution of silver from coarse particles in the heap leaching columns. It was observed that maximum extraction of metal from the surface reaction of the solid tracer (synthetic silver ore) was achieved within the period of 50 hours of leaching until a more or less steady continuous extraction was attained after 100 hours. The dramatic drop in the extraction concentration curves of *Figure 6.3* for all column investigations suggest that the dissolution of the metal from available grains directly exposed to the penetrating lixiviant solution at the surfaces of particles in the convoluted channels had been depleted. Dissolution extraction after the drop was perceived to be ultimately controlled

by particle diffusion of lixiviant in and out of the subsurface of the particle through small pores or submicron fissures. This corroborates evidence led in *chapter 4* where the synthetic ore was perceived to largely depend on the prevalent submicron pores that restricted diffusion.

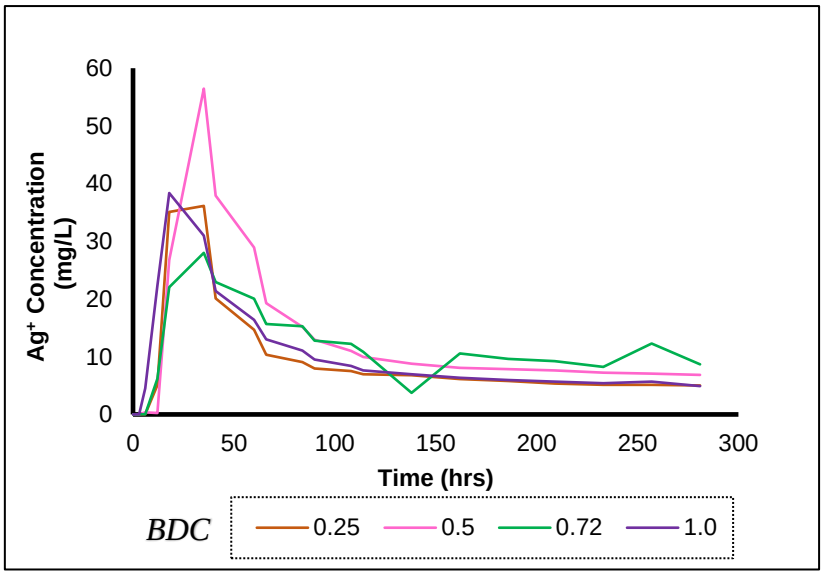

Figure 6.3 Effluent concentration of dissolved silver at different packed bed coefficient distribution with constant flow rate, 6 l/m²/h at 25 °C and 275 ppm NaCN.

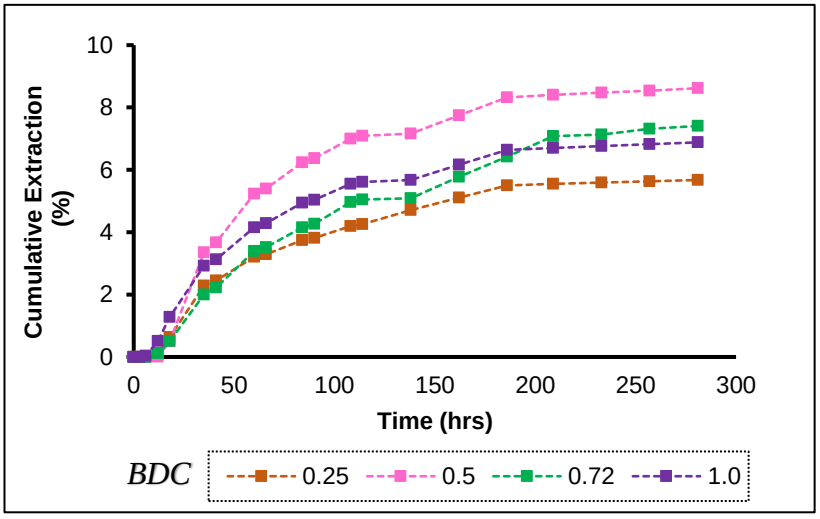

Figure 6.4 Cumulative extraction curves with respect to the varying PSD coefficients (BDC).

In principle, the smaller the size fraction of the crushed particles, the more likely rapid silver extraction is due to the larger exposed surface area of embedded mineral grains for surface interactions with the lixiviant. However, the leaching extraction in this column investigation was observed to be quite different. Metal extraction was seemingly independent of the PSD coefficient distribution of the packed bed evident in both *Figure 6.3* and *figure 6.4*.

The 0.25 BDC extraction was marginal and followed the same trend to the extraction of the material with 0.72 and 1.0 PSD coefficients. This was not expected. Low extraction could be attributed to a combination of two effects:

i. Surface leaching is more rapid, but solution migrates more slowly through the fines material, offsetting the higher dissolution and
ii. The flooding stage preceding the RTD consequently led to extreme local settling and compaction of the bed particles.

The fines ultimately stay saturated after flooding; hence acting like larger porous particles, thus reducing surfaces of available exposed grains in the bed to attain maximum solid-lixiviant interaction. The multitude of individual loose fine particles consequently forming larger porous clusters result in the prevalence of diffusion-controlling regime dominating the bed; thereby increasing the number of stagnant zones.

Interestingly, the initial reaction dissolution of the 0.721 BDC with respect to the surface extraction stage demonstrated lower extraction than 0.25 and 1.0 BDCs leaching performances. However, during the 0.721 BDC dissolution a rapid reaction regime was observed after the 50 hours to maintain a significantly higher extraction than the 0.25 and 1.0 BDC in *Figure 6.3*, while *Figure 6.4* demonstrates a gradual increase of cumulative extraction until the experiment was terminated. A change of mechanism is perceived to have been responsible for this leaching performance.

The cumulative extraction curves of *Figure 6.4* for all changing PSD columns further show similar initial extraction rates – attributed to dissolution from surface reaction - and ultimately follow a divergence toward the final rate of leaching by a factor of about 2. This trend suggests that extraction ultimately becomes independent of the packed bed blending coefficients simply after mineral conversion from surface reaction is complete. Extraction was perceived to be a function of available grains at the particle surface and diffusion-reaction mechanism operating at the subsurface of the material (*Chapter 5*).

It was reported in *Chapter 4* that the synthetic ore achieved its 'ideal' characteristics reasonably well; including homogeneity in grain size, relatively even grade distribution, uniform grain dispersion, and homogenous porosity. However, porosity was not continuous at the scale at which it could be detected (4-5 micron), indicating a lack of interconnection of cracks/fissures to aid leaching extraction of silver from the external surfaces into the inner subsurface of the coarser materials. Thus, the non-continuous nature of pores in the ore is postulated to inhibit reaction kinetics of lixiviant diffusion into the core of particles. This work has revealed that extraction of metal from coarse ore particles heavily relies on the interconnection of pores through fissures and cracks for metal dissolution; this is in agreement with reports by (*Ghorbani, 2012, Negron et al., 2016*). Additionally, metal extraction from coarse particle is also dependent on the reactivity of the gangues toward the lixiviant (i.e. acid) to induce cracks as in *Ram et al., (2020);* nonetheless, gangues in the investigation was non-reaction.

It can be recalled from the previous section that results of the non-reactive RTD showed that the influence of flooding on the residence time of the penetrating solution was marginal for the 0.5, 0.72, and 1.0 coefficient distributions. Furthermore, the rapid drop in the concentration gradient following the step change of the non-reactive RTD for the distribution coefficients (0.5, 0.72, and 1.0) suggest that solution hold-up was inconsequential. Therefore, extraction is not expected to be inhibited by the presence of stagnant regimes, as the distribution of the fines in the respective beds was perceived to be well dispersed in the reactor. Hence, this further validates the availability of grains at the particle surface. Accessibility of embedded grains through the internal porosity of the material determines the overall bed extraction patterns for the duration of leaching.

Extraction based on the varying PSD coefficient illustrated overall extraction to be ~ 5.7 %, ~ 8.6 %, ~ 7.4 %, and ~ 6.9 % correlating with 0.25, 0.50, 0.72, and 1.0 BDCs respectively. The different column PSDs show that extraction exhibited an inverse correlation: Increasing the blending distribution coefficient values resulted in a decrease in the extraction of dissolved silver reporting in the column effluent stream.

In this sense the extraction performance determined for the various PSD coefficients was expected, except for the 0.25 BDC. The 0.25 BDC was perceived to have been affected by a slow migration of lixiviant solution and the saturated consolidation of fines into larger, macro-porous particles resulting from the flooding stage. Although the duration of leaching in this work was not long, it is worth mentioning that settling and compaction are two apparent mechanisms most likely to result after a longer period of leaching in actual heap operation or longer experimental works. This could further inhibit dissolution extraction from compacted zones.

6.3 Effect of Changing Flow Rate

In order to ascertain the influence of the different application of flowrate on the packed bed, columns were stacked with material at particle distribution coefficient 0.721, and the flow rate was varied, increasing from 3, 6, to 12 L/m^2/h.

6.3.1 *Non-Reactive Tracer RTD*

Results from the inert KNO_3 tracer test work shown in *Figure 6.5* demonstrate that residence time was larger in the 3 L/m^2/h flow rate for both step-up and step-down investigations, compared to the 6 and 12 L/m^2/h. When irrigation of the packed beds was initiated, the step-up tracer showed a rapid response of the maximum input concentration, reporting to the effluent stream in less than 24 hours for both 6 and 12 L/m^2/h flowrates. By contrast, the experiment at 3 L/m^2/h reached its maximum concentration at about

80 hours, exhibiting varying maximum concentrations at its peak before and after the step-down change. This was attributed to the fact that the lowest irrigating flow took a longer time to meander through the interstices of the particle level micro- and bed-level macro-channels.

On the other hand, the step-down change showed a rapid drop with a marginal difference across the investigated flowrates. The step-down change was applied after 124 hours of operation. The results demonstrate a shift in the RTD to the right of the time scale as the irrigation rate decreased. Evident from the characteristic tail, although not as long as in the case of varying PSD discussed in the previous section, operating at the lowest flow rate did not fully attain the near-zero concentration level as at the highest flow rate (12 L/m²/h).

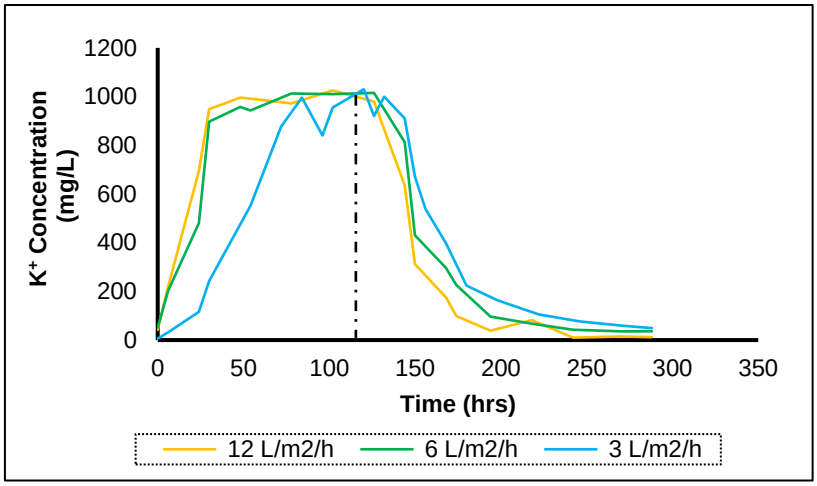

Figure 6.5 K+ concentration (1g/l) profile of full step tracer plotted against time varying flowrate conditions at constant PSD coefficient of 0.72. Step change was applied after 5 days of irrigation.

The maximum concentration in the profile of experiments at 6 & 12 L/m²/h flowrates experience marginal variations; however, the concentration at the peak of the 3 L/m²/h curve fluctuated more. These variations are due to different paths of the tracer permeating the bed, outward diffusion of the peak concentration from convoluted paths, as well as reagent release from slower-moving solution in long convoluted channels. This influence was initially observed during the column wash phase prior to the RTD run, where conductivity measurements suggested higher values than previous measurements when the application of flow was intermittently operated (*see* ***Appendix VI.b***).

Converting the concentration profiles to the RTD *F-curve* using the step-down tracer data (*Figure 6.6*), the difference in residence time was observed to be marginal over the varying flow rates, offset only by a few hours after the step change between the highest and lowest flow rates. The curves are more similar to the distribution of a characteristic plug flow type response, evident by the 30~40 hour time delay in the reactor

before the breakthrough in the effluent stream. The flowrate influence on RTD in the packed bed was alluded to by (*Cherkaev, 2019*) who also showed that flowrates typical to heap leaching were insensitive to the RTD solution hold-up under different application rates in packed beds.

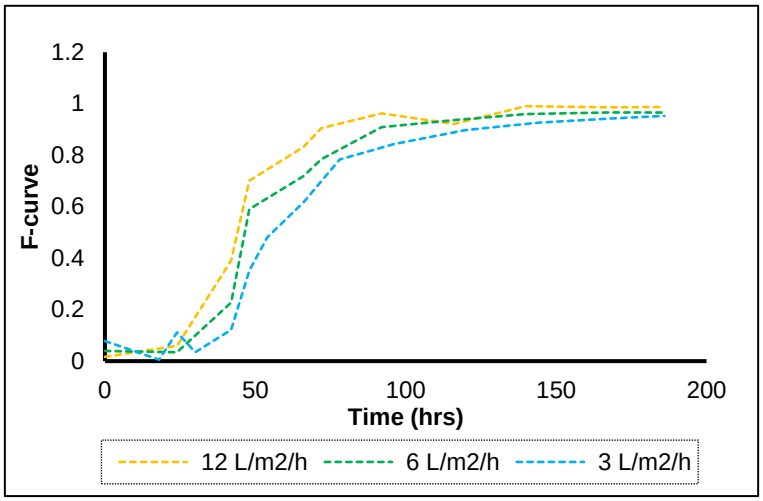

Figure 6.6 Inverted normalized Step-down RTD profile illustrating the effect of changing flow rate utilizing single PSD of 0.721.

6.3.2 *Column Extraction*

Figure 6.7 illustrates the influence of varying irrigation rates on the packed bed, based on extraction using a single selected blending distribution coefficient (0.721). It was observed that the extraction followed a similar pattern of surface reaction with initial peak and protracted tail but did not demonstrate any direct correlation with increasing flow rate.

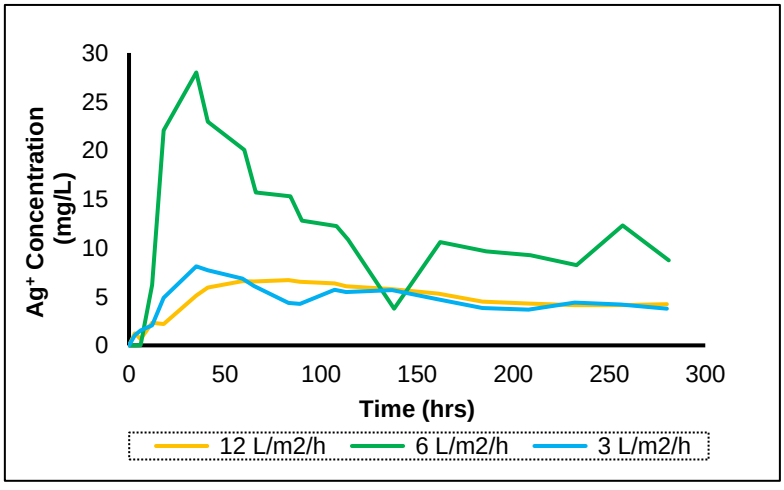

Figure 6.7 Silver concentration curve illustrating varying flowrates with respect to extraction performance at constant bed PSD distribution (0.72).

It could be postulated that at higher flow rates the solution percolating the bed would access a larger number of convoluted paths than at lower flow rate. However, when the velocity of the flow is higher than the reaction kinetics, extraction is expected to be marginal compared to irrigating the bed at a lower flow rate. On the other hand, when the bed is irrigated at a much lower flow rate, the postulation follows that penetration is more likely subjected to fewer paths from where the reagent solution is distributed to the bed. It is also perceived that tortuosity could be essentially operating in the column at the lower flow rate considering these fewer paths.

Furthermore, in stagnant zones or pockets, reagent solution has sufficient interaction with the particle surface for mineral dissolution, but remains trapped due to its limited access to the bulk flowing solution in the bed. Eventually, this results in metal extraction emerging from narrow channels through which slow-moving permeating fluids were subjected. This is related to the results of the nonreactive RTD that suggest that flow at a lower rate could have permeated through narrow channels evident from the time difference observed in the rates.

Cumulative extraction curves for each reactor investigated at the varying flowrates are presented in *Figure 6.8*. The curves demonstrate that the extraction of silver at different flow rates exhibited similar trends for the 6 and 12 L/m²/h experiments, but the lowest flow rate behave substantially differently.

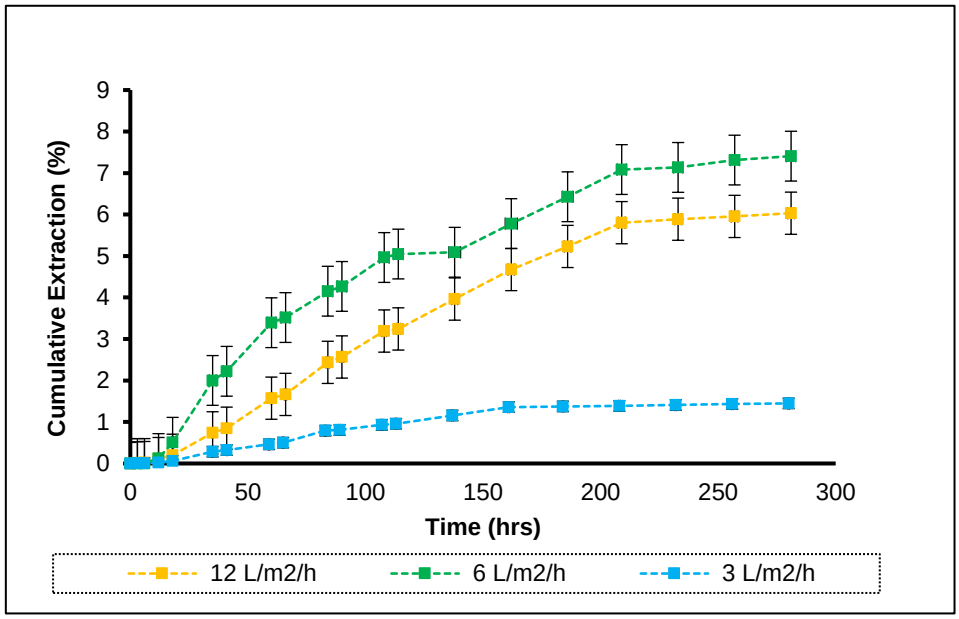

Figure 6.8 Cumulative extraction curves of columns leached at different flow rates. Feed distribution was constant at 0.72 PSD coefficient and NaCN concentration was 275 ppm at 25 °C.

Given the length of the experiment, concentration of silver extracted at the highest flow rate was expected, while extraction concentration with respect to the lowest flow rate was not. These experiments were repeated, which continued to show the same inconclusive correlation when the flowrates were changed. With the error bars in *Figure 6.8* for the beds under changing flow rates, statistically, the performance of extraction from the lowest flowrate cannot be concluded to be an underperformance, neither is it an outlier. This clearly suggests the curves represent the system's actual performance. Although the packing is all similar (0.721), the error analysis suggests there is a certain degree of deviation in the extraction that is not very significant in the context of the parameters studied.

Overall silver extraction with respect to varying flowrate was about ~ 6.1 %, ~ 7.4 % and ~ 1.5 % achieved at 12, 6, and 3 $L/m^2/h$ respectively. The overall results of extraction in terms flow rate are inconclusive as the dissolution trend exhibited the least extraction at 3 $L/m^2/h$. Such a low flow rate was expected to have accomplished maximum extraction due to sufficient time the lixiviant might have spent convoluting through the packed bed, considering that the ideal properties of the ore were relatively achieved.

One possible reason for the low extraction at 3 $L/m^2/h$ could be the coalescence of the slow flowrate through channels resulting in longer pore length through the packed bed. Additionally, such extraction performance is perceived to be limited by the sodium cyanide lixiviant in the reactor. The lixiviant limiting effect is discussed further in the next section.

6.4 Recovery Performance

The investigation of coarse synthetic silver ore extraction in the heap packed bed was considered in two contexts; i.e. extraction based on flow rate and ore bed artificial particle size distribution. The extraction of

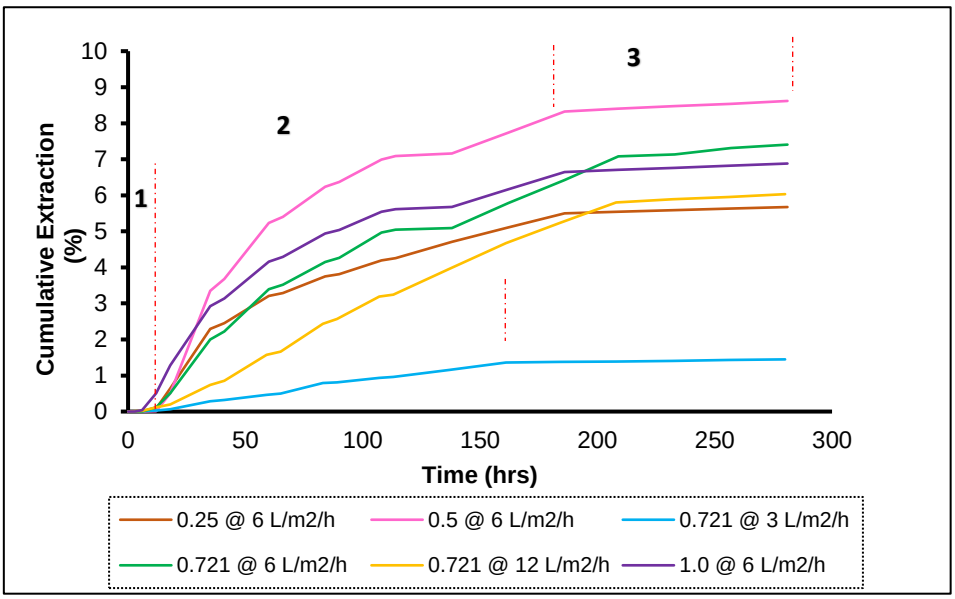

Figure 6.9 Combine extraction performance of packed bed column leaching of synthetic silver ore at constant PSD (0.72) at varying irrigation rates and leaching at constant irrigation rate of 6 l/m²/h at vary particle bed distribution coefficient (m).

silver shown in *Figure 6.4* and *Figure 6.8* is consolidated and presented in *Figure 6.9* for further analysis on the dissolution performance.

As the result of slow reaction kinetics of silver dissolution and the limiting effect governed by diffusion of lixiviant in and out of large particles in heap leaching, the extraction recovery observed over the 12 days of experimentation was not very high. The leaching characterization of the synthetic ore (*Chapter 5*) revealed slow kinetics and inner-particle diffusion to be responsible for the coarse particle leaching. Perhaps tortuosity apparently operating at the coarse particle level in the columns could also be responsible for constraining oxidant delivery to the reaction sites. The homogenous, non-continuous porosity of the ore ultimately inhibited extraction from the internal regions of the particles, thereby limiting rapid extraction from the core or subsurface of the particles. These findings are all perceived to be ultimately operating in the different column configurations at 0.5, 0.721, & 1.0 BDCs and 6, & 12 L/m²/h flowrates, since their dissolution performance was expected. However, for the column configurations in which a large proportion of fines existed (0.25 BDC) and lowest flow rate (3 L/m²/h) was investigated, it was anticipated that their respective extraction performance was going to be highest, but this was not the case. While particle

diffusion might also be responsible for influencing this performance, it is proposed that a different mechanism, namely a reagent-limiting effect, is dominating in these columns.

There are two possible scenarios occurring in both 0.25 BDC and 3 L/m²/h flowrate columns - where there is a switch of mechanism between a kinetic limit and a reagent supply limit. When there is a slow flowrate/bed with compacted fines, the reagent might not just reach the sites fast enough and it gets all consumed up, thus the supply of NaCN becomes rate-limiting. Whereas in the case with the higher flowrates/less fine BDC that is not a problem because sufficient NaCN is put through the system.

The second scenario is where the packed beds are kinetically limited; particularly once the surface leaching is completed and is followed by a slower rate where the silver comes through the particle pores from deeper within the particles.

Observations from the extraction curves of *Figure 6.9* further show three regimes of dissolution phases occurring in the RTD column.

1. An initial extraction delay period,
2. Rapid leaching phase, and
3. Linear leaching phase.

The extraction delay phase is attributed to rapid solution breakthrough in the effluent after the feed reservoir was switched to the NaCN lixiviant. This region suggests that during the initial application of reagent solution to the bed, the bulk mobile solution flow was more rapid than the reaction dissolution; i.e. shorter residence time with inherently very little or no initial reaction. Subsequently after a period of 3~6 hours (up to 10 hours for some columns), substantial increase in the dissolved metal effluent concentration gradient is observed. This is perceived to have resulted from the film of rivulet flow of the slower movement of the lixiviant solution at the contact zones of the particles; i.e. the surface leaching stage.

The rapid leaching of the initial set of 5~8 % of dissolution recovery suggests surface dissolution occurring; while in the linear phase the leaching levels off, suggesting a bulk dissolution from inside the particles which operates at a small but not zero rate. The leaching at this point does not completely stop but becomes very slow. Interestingly, the slope seems somewhat similar in all the experiments. Slopes from the linear leaching phase for all column extractions are presented in *Table 6.3*. It is worth emphasizing that this gradual dissolution from the particle is not entirely from the inner uncracked core, but ultimately from regions near the surface. This was evident from the XCT characterization and PLS effluent result (*Chapter 4 & 5 respectively*).

The curves with changing BDCs and flowrates in *figure 6.9* performed fairly similar in the same region (between 5~8 %). This indicates that they are all in closely related margins and it cannot be concluded that they are significantly different. The major difference is seen in the bed with the lowest flow rate where the performance was found to be systemic and not an outlier (see *Figure 6.8*).

The fairly similar performance of the other columns observed in *figure 6.9* corresponds to the linear phase leaching, the slopes of which are shown in *Table 6.3* where the slower dissolution rate occurred in a close range. It is further observed in *Table 6.3* that the rate/slope describing the slow dissolution linear leaching phase was substantially lower for the 0.25 BDC and 3 L/m²/h than the other columns.

Table 6.3 Illustration of slopes from the columns of figure 6.9 tending towards bulk dissolution from pores.

BDC	Flowrate	Slope	LP* Inception (hrs)	R^2
0.25	6 L/m²/h	0.0018	186	0.9987
0.5	6 L/m²/h	0.0030	186	0.9990
0.721	6 L/m²/h	0.0048	209	0.9616
0.721	3 L/m²/h	0.0008	161	0.9923
0.721	12 L/m²/h	0.0031	209	0.9981
1	6 L/m²/h	0.0025	186	0.9996

*LP – Linear Phase

Noteworthy is the fact that the inception of the linear leaching phase for all columns did not occur at the same time. Three periods were observed; i.e. at 161, 186, and 209 hours. The column with the earliest (161 hour) and lowest (0.0008) linear leaching rate reporting in the effluent leachant was the 3 L/m²/h column. This is elucidated by the kinetically constrained rate of leaching that was more prevalent, as indicated by its extremely low slope. Although the 0.25 BDC dissolution became slowest after 186 hours of leaching, its lowest rate compared to the other columns at similar linear leaching period suggest rate constraints that were analogous to the 3 L/m²/h column.

6.5 Influence of Particle Distribution and Flow Rate on Flow Type Performance

This section attempts to translate the nonreactive tracer and leaching experimental data to existing models in order to interpret the flow performance. The nonreactive RTD results are compared to simple plug flow and CSTR models while the leaching extraction result of silver from the effluent leachant is interpreted

with the simplified extended *K-phi* mixed topology model (*Extended Mixed Topology Model*) to determine the flow type behavior.

6.5.1 *Tracer RTD Performance*

The multi-channel column bed is perceived to be characterized by a distribution of parallel plug flow channels. The distribution performance of the nonreactive tracer response is first analysed using the simplest approach of translating the experimental RTD effluent data to conventional plug flow and single-CSTR models to qualify the flow performance.

The cumulative distribution function *F(t)* for an ideal plug flow response is given of the form by *equation 6.1,* for a step tracer input.

$$F(t) = \frac{C}{C_o} \qquad \textit{Eq. 6.1}$$

The so-called *F(t)* term was determined by the normalization of the tracer concentration either in the feed solution, for step-up, or maximum concentration in the packed bed, for step-down (*see section 6.2.1*).

For a single CSTR RTD, the *F(t)* is given of the form by *equation 6.2*,

$$F(t) = 1 - e^{-t/\tau} \qquad \textit{Eq. 6.2}$$

$$\tau = V/v_o \qquad \textit{Eq. 6.3}$$

Where V and v_o are variables for the reactor volume and volumetric flow rate, respectively. Arbitrary concentrations and dimensionless time corresponding to the experimental data were utilized to generate typical plug flow and single CSTR curves for *equation 6.1* and *equation 6.2* respectively.

The step-change nonreactive RTD cumulative distribution experimental data are compared to the single-CSTR and plug flow models in *figure 6.10* and *Figure 6.11*. It is apparent that the step-up data had fewer points, resulting in less resolution as compared to the step-down. Hence, *figure 6.10,* comparing the flow type models to the experimental data, shows the different reactor configurations (all changing BDCs and all changing flowrates) exhibiting inconclusive flow performance, but still tending towards CSTR behaviour.

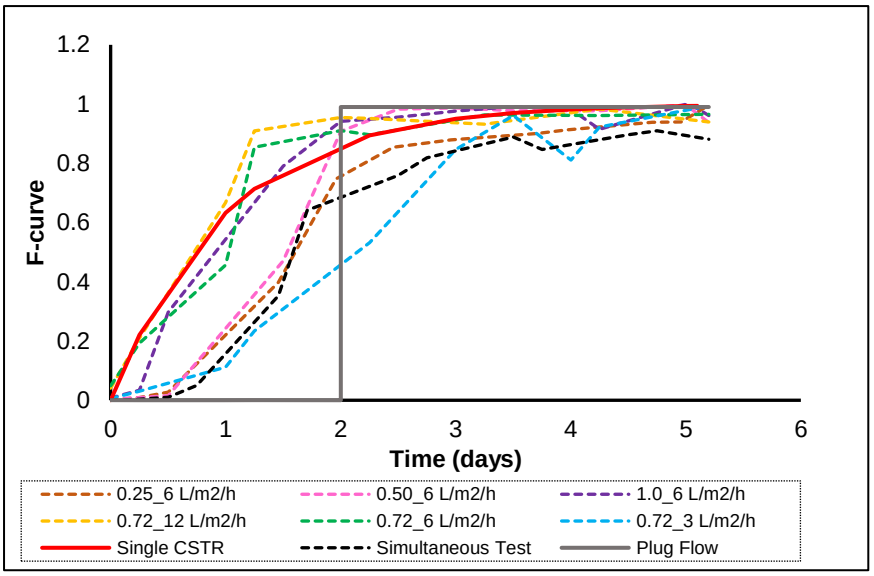

Figure 6.10 All step-up RTD comparison with single-CSTR and plug flow models.

This behaviour is attributed to the rapid increase in the gradient of the tracer appearance in the effluent stream. It was initially anticipated during the experiment that the step-down step change would have been made after 6 days of irrigation; however, all the beds with the exception of the 0.25 BDC and the 3 L/m²/h columns attained the maximum input concentration earlier than the expected time. Furthermore, the sampling for both step-up and step-down approaches was scheduled to be the same for simplicity during the data reconciliation; however, the maximum concentration of the tracer in the effluent was reached earlier than expected. Thus the step-down was consequently started earlier than the anticipated time. The step-down RTD data, on the other hand, had much better data resolution during and after the step change in order to compare the flow type performance to the step-up results. Hence, the step-down results were used throughout this study's RTD analyses.

While the breakthrough of the tracer concentration in the effluent stream for the step-up was rapid with low data resolution, the step-down tracer concentration emulated curves that indicate the exchange of phases between stagnant pore regimes and mobile flowing solutions, as discussed in previous sections in the chapter.

This suggests that the rapid increase of the tracer in the effluent stream is due to less interaction between phases in the packed bed, resulting in flow a distribution typical of a CSTR type, inferring that when higher proportion of coarser particles with insufficient fines are present, they will allow not enough contact of flowing solution with the bed particles. Although the influence of height on the RTD flow type behavior has not been investigated in this study, it is perceived that the height of the packed bed reactor also has an influence on the flow type performance of a packed bed i.e. where longer beds would exhibit delays in the

effluent and shorter beds attain a rapid breakthrough. This, however, would need to be validated in a separate study.

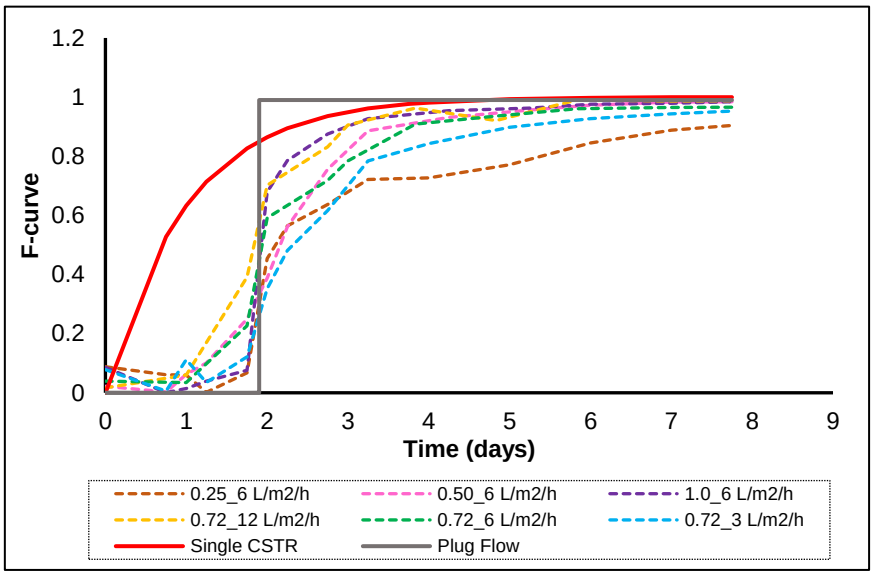

Figure 6.11 Inverted step-down RTD comparison with single CSTR and plug flow models.

Figure 6.11 shows that all the reactors for all sets of experiments exhibited flow type performance that deviated from a well-mixed-type reactor distribution and more closely resembled a characteristic plug-flow type behavior. Based on the nonreactive tracer investigation of this project, considering PSD and flowrate parameters, it can be concluded that for a column or packed bed reactor the ultimate flow type distribution would be analogous to an ideal plug flow type. However, the inherent flow type of a packed bed at irrigation rates typical of heap leaching largely depends on the PSD within the bed to produce the said plug flow or a well-mixed flow behavior.

6.5.2 *Modelling Extraction Performance Response*

It is postulated that different flows in the packed bed go through different distributions of plug flow reactors in parallel. These different distributions allude to different lengths, thus making particles that are exposed for a short time to the passing solution leach poorly, while those in contact with the lixiviant for a longer time will consequently have better extraction. The one critical aspect of the assumption, which serves a major limitation, is that there exists no certainty that the different channels have exposure to ore of the same particle size distribution; the chances are that the long paths are more exposed to a larger proportion of fines and shorter paths would suggest the prevalence of coarse particles along the path.

In order to determine the flow behavior of the packed bed columns based on the reactive leaching approach, extraction data obtained from the selected four particle fractions (-19/+16, -16/+11.2, -8/+5.6, and -4/+2.8 mm) from the CF-FBR leaching (*chapter 5*) was modelled utilizing the *K-phi* mixed topology model, first individually for each size class and then weighted for the distribtions used in the columns. This was compared to the column leaching extraction by translating the information obtained from the nonreactive RTDs of each experiment. Conceptually, the analysis of this work correlates the extraction from an ideal CSTR flow reactor with column leaching extraction that assumes multiple plug flow which has the residence time that roughly emulate flow behavior of a CSTR.

Overall conversion for each column was determined by integrating the selected individual size class conversion from the CF-FBR extraction with their respective relative weighted percentages as described by the simple blended particle model in *equation 6.4* used to simulate the column leach curves.

$$X(t)_{tot} = \sum_{i=1}^{n} g_i X(t)_i \qquad \textit{Eq. 6.4}$$

where, $X(t)_{tot}$ represents the total weighted average conversion of the blended particle distribution, n is the total number of size classes over the extraction period, g_i is the mass fraction of particles of size class in the distribution, and $X(t)_i$ is the mineral conversion corresponding to the individual particle size class after time t of leaching; which is represented through the the extended *k-phi* model (*Ghorbani, et al., 2013*), *also see Extended Mixed Topology Model*.

Each size was modelled using the parameters given in *Table 5.5* and the weights were determined to emulate the distribution with the GGS distribution coefficient of 0.721. These were then put together to determine the overall weighted average extraction ($X(t)_{tot}$), which were then compared with the column extraction curves.

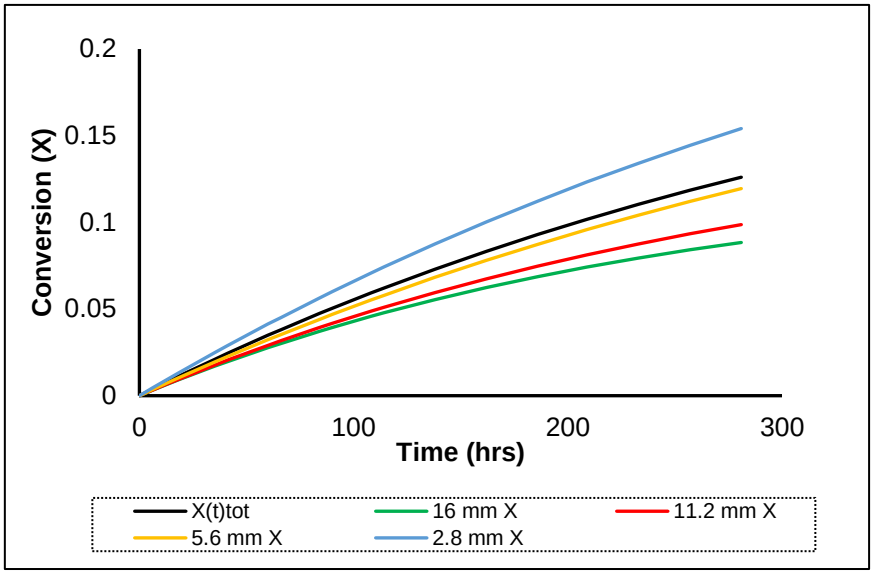

Figure 6.12 model leaching extraction of blended particles simulating average weighted extraction from the CF-FBR individual particle leaching curves.

Figure 6.12 shows the simulated model distribution of the four particle sizes used in the blends. The model was calibrated with the time distribution from the leaching columns and extraction parameters (*Table 5.5*) from the CF-FBR respective size extraction curves.

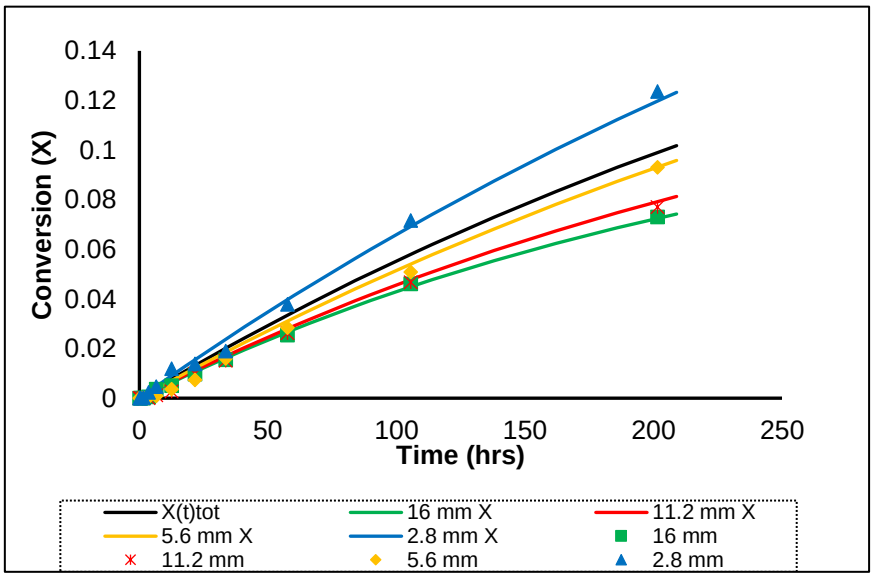

Figure 6.13 Cmparison of the model data of figure 6.12 with the actual extraction data at 200 hours leach time at 25°C and 275 ppm NaCN. Model predictions for each class are signified by X.

As depicted in *figure 6.13* with extraction extending over 200 hours, the fit for each size class- to the model prediction against which they were calibrated is excellent. Therefore, the weighted average conversion for the blend was assumed to offer a good prediction of the extraction from the column leach experiments at standard conditions (25°C, 275 ppm NaCN, and pH 10.5, 0.721 BDC).

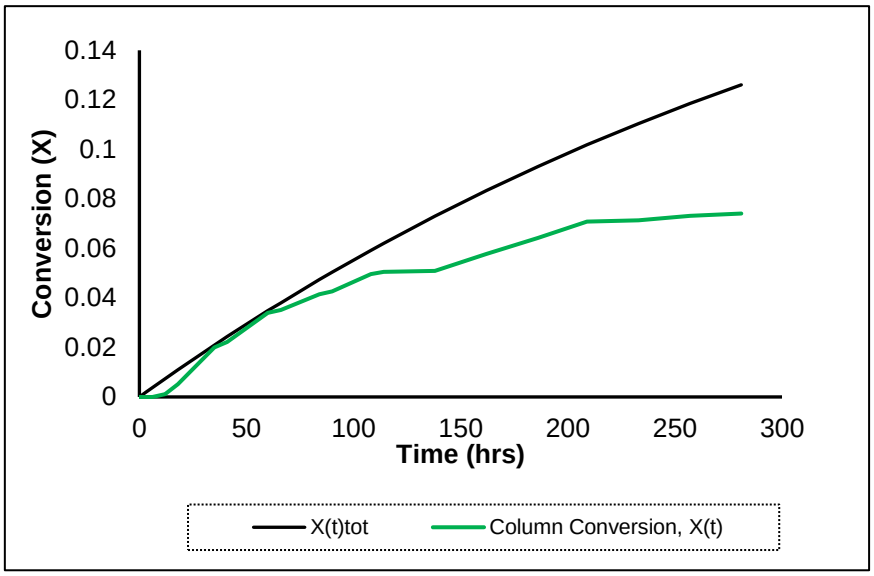

Figure 6.14 Particle blending model fit to actual column leaching data at standard conditions, i.e. 25 °C, 275 ppm NaCN, 0.721 BDC, & 6 L/m²/h.

Figure 6.14 illustrates the model prediction compared to an actual column leaching curve. It is worth re-iterating that the model was calibrated against the batch CF-FBR data using the 0.721 BDC for the relative weighted distribution of the selected fractions and compared to the column leaching extraction to elucidate the flow behaviour. Given the CF-FBR operated as a CSTR, the model would clearly not predict plug flow, but rather CSTR behaviour, which is compared here to the extraction data from a plug flow reactor.

Compared to the model prediction the column leaching data showed a short offset or initial induction prior to the rapid surface extraction, followed by a relatively slow dissolution phase; nonetheless, the overall curve behaves quite similar to that of a CSTR. The conversion in the column reactor largely deviated from the model prediction as the column leaching tended toward a slower pace after about 80 hours. For its part, the model prediction demonstrated a steady rate of extraction. Although the two curves do not match well, the leaching curve was confirmed to be of a CSTR-type.

As postulated, conceptually it is perceived that the performance of a plug flow column showing CSTR behaviour could be possible if the column is characterized by a number of parallel flow channels with different channel lengths, each containing ore with the same blended PSDs. Therefore, in an expansion the

model is interpreted by considering each pore length to be sectioned into compartments as rows of CSTRs operating in series (*see figure 6.15*). Thus, it is assumed that once all compartments in a pore length/stack have encountered the lixiviant at different time steps, the average conversion will then appear in the effluent; i.e. the model emulates plug flow as a series of CSTRs. The different lengths of columns are modelled accordingly; the shorter ones with fewer CSTRs, and the longer ones with more; taking into consideration that each CSTR has exactly the same size and therefore the same internal residence time in each step in order to normalize the time steps.

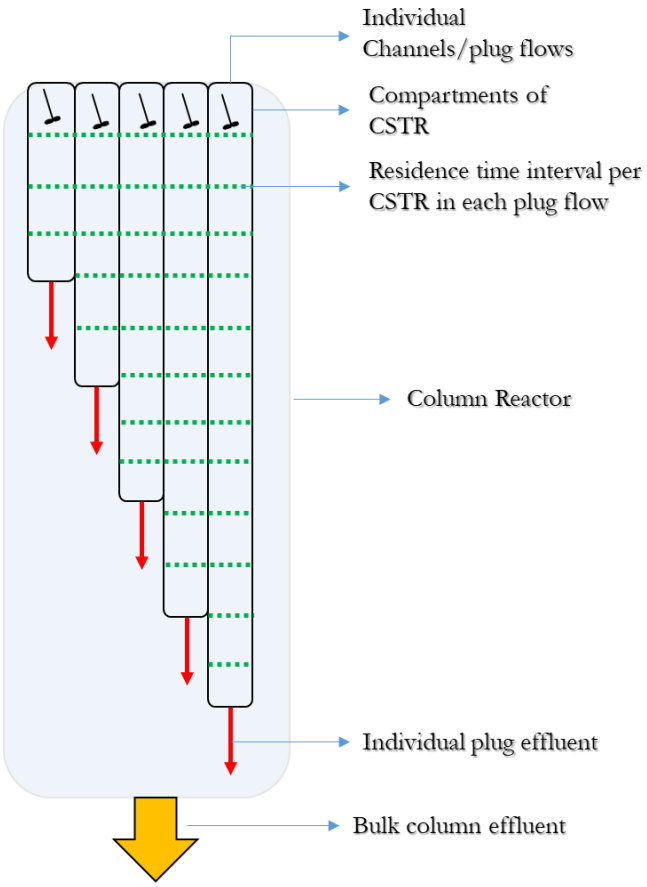

Figure 6.15 Column schematic illustrating the conceptual ideal of fluid flow RTD behaviour characterized by distribution of different pore lengths containing compartments of CSTR in series.

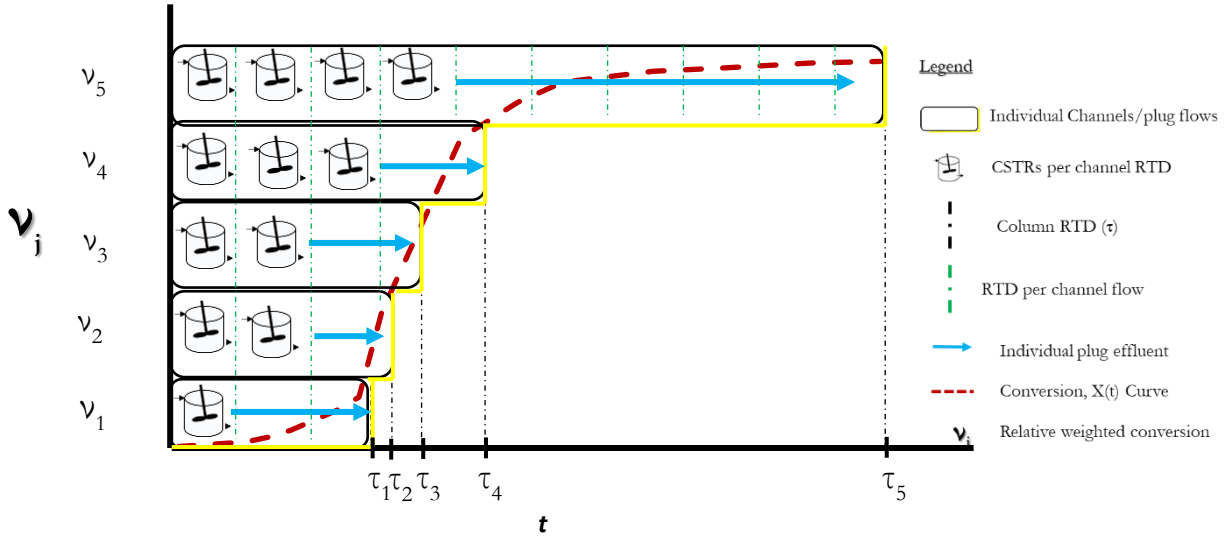

Figure 6.16 Conceptual schematic of the proposed behaviour of the column distribution with respect to the output flow type superimposing figure 6.15 onto column RTD curves.

The approach was analysed with the use of data measured from the column RTD (step-up/ step-down) curve to model the extraction flow type. The CSTR-like extraction curves were then sectioned arbitrarily into a number of channels representing individual CSTRs in series with residence times each alluding to the RTD curve (*figure 6.16*). Assuming the same size distribution in each compartment for a continuous time in specified hourly intervals, the sectioned plugs will exhibit exactly the same extraction curve but offset by different time intervals of the plugs. This shows that each of the leach curves basically contributes to the effluent by a certain relative weighted average – obtained by the length of each individual flow channels (as represented by the corresponding residence time). Noteworthy, the sections/ flow channels can be arbitrarily selected up to a number of plugs, depending on the RTD data resolution; nonetheless, the selected tau (time) values must be divisible by the specified hourly intervals.

This concept can be described in *equation 6.5* where v represents the weighted average percent parameter for each arbitrarily selected pore channel, j, sectioned across the RTD conversion curve; and b representing the total number of pore channels sectioned.

$$X(t)_{tot} = \sum_{j=1}^{b} \sum_{i=1}^{n} v_j g_i X_i \qquad \textit{Eq. 6.5}$$

Figure 6.17 shows the plot of the modelled overall column conversion for the multiple CSTRs in each plug channel versus the leaching extraction curves translated with the use of the RTD data. The column leching was fed with the reagent solutions in successive separate experiments; i.e. RTD tracer test followed by leaching extraction studies. The column was condition at 1 g/L and 275 mg/L K^+ and NaCN respectively with pH~ 10.5. The flow rate was set at 6 L/m²/h, blend distribution coefficient was 0.721, and the temperature was at room condition (~25 °C).

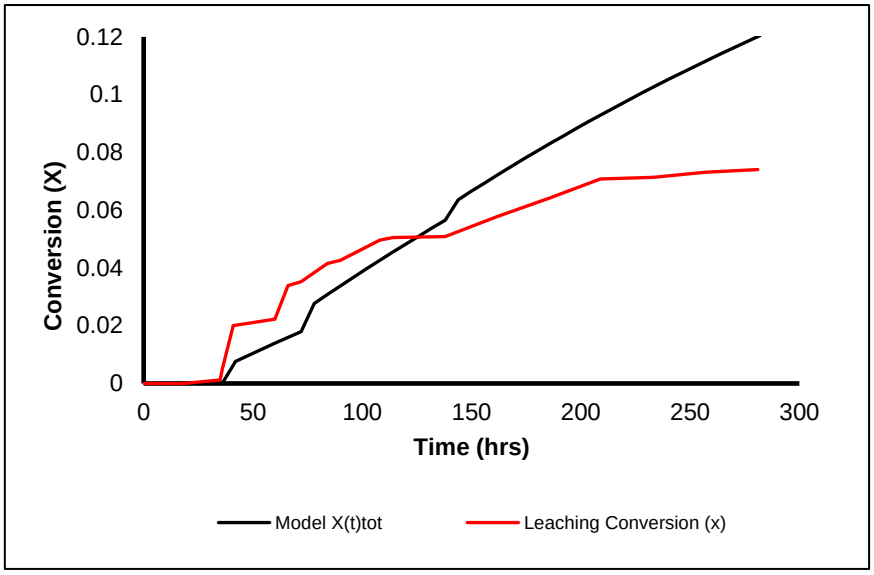

Figure 6.17model prediction against successive reactive leaching column after nonreactive tracer application. The column was configured at 1 g/L K+, 275 mg/L NaCN, pH~ 10.5, 6 L/m²/h, 0.721 BDC, and 25 °C.

Figure 6.17 shows that the modelled curve exhibited a reasonably good prediction, however, offset by 2~4 % conversion. While the curve still does not compare too well against the raw silver dissolution data, the poor model prediction with extraction results is largely attributed to the deviation of the leach curves to the model calibration and the complicated reaction-diffusion silver dissolution system.

The model prediction is observed to be fair until after about 120 hours when a slower rate of leaching in the column occurred. This suggest that more readily leached fraction were occluded from the leach solution, thereby resulting in them leaching more slowly than the model would assume. The model assumes the same particle size distribution associated with all flow paths, and that all particles are freely accessible, whereas the extraction data indicates that the slower flow paths may be associated with the coarser material and the initial leaching is associated with fines.

In an effort to expand the experimental approach to elucidate the column flow performance, a column was configured with similar conditions as the successive column experiments (in *figure 6.17*); but the mode of application of the lixiviant feed solutions were different; the KNO_3 tracer chemical and NaCN reagent were mixed together and fed to the column simultaneously from a single reservoir. The prediction curves of the modelled extraction data and the simultaneous column extraction data are shown in *figure 6.18*.

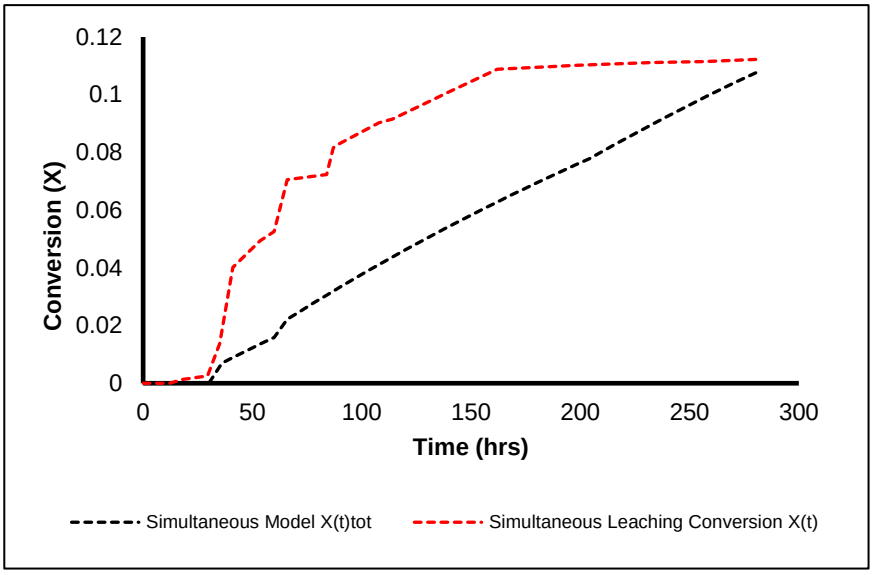

Figure 6.18 Model extraction curve plotted against simultaneous solution application column extraction data illustrating significant deviation from the actual column leaching. Column conditions were 1 g/L K+, 275 mg/L NaCN, pH~ 10.5, 6 L/m²/h, 0.721 BDC, and 25 °C..

Figure 6.18 clearly shows that the model prediction for the simultaneous column leaching experiments significantly deviated at the inception of the extraction after the effluent breakthrough. The column leach curve could not possibly be modelled with the CF-FBR kinetic model due to the maximum extraction over 150 hours being just about 7~8 % for the fastest leaching fraction (*see Figure 6.13*) and not as high as up to the 11 % observed for the simultaneous column – indicating a much faster extraction than any of the size classes investigated in the CF-FBR tests. This could possibly be related to much more rapid leaching of the fines for which there was data only from the inconclusive shake flask tests (*see section 5.3.1*) to determine whether the fines fraction leaches fast enough for such high extractions to even be possible. Thus, the model will not dramatically change the predictions for any other input, as it was not calibrated against any potentially faster leaching phase. This is quite evident in the two modelled scenarios – although they have different residence times, the model predictions look fairly similar (*see figure 6.17* & *figure 6.18*). Nevertheless, the experimental outputs look dramatically different from the model. It must be noted that the model curves can only emulate what it was calibrated against. Considering the column reactors contained all nine size class fractions in the 0.721 BDC, a substantial fraction (~33 %) of the material (-2.8 ~ -1 mm) -

containing more exposed surfaces for extraction - was not included in the model calibration data as the CF-FBR could not accommodate class sizes below -4/+2.8 mm.

On a side note interestingly, it was observed that the extraction curves of the successive (*Figure 6.17*) and simultaneous (*Figure 6.18*) column experiments look similar in trend but are offset by the extent of extraction, which raises the question why both column experiments with similar conditions have extractions that are not the same.

It is postulated that in the simultaneous test a high concentration of potassium nitrate inputted at the same time with the cyanide lixiviant possibly could have accelerated the extraction. This cannot be ruled out, recognising that no test was performed to check whether the higher ionic strength of the mixed tracer/lixiviant solution might be responsible for driving the reaction or perhaps the chemistry combined system shifted the whole dissolution reaction. For example it is possible that the potassium nitrate will better oxidize silver than the oxygen. However, these postulations cannot be made with any degree of certainty without further testing.

For its part, after the RTD step-up of the successive column experiment, the step-down approach - with the application of deionized water- rinsed the column before the leaching extraction studies. Thus if the kinetics of reaction dissolution in the columns were influenced by the initial assumption of the solution ionic strength or aided oxidation of excess nitrate, then that obviously would have affected this column to a lesser extent.

Finally, the modelled overall curves (*Figure 6.17* & *Figure 6.18*) are fairly linear; this is largely attributed to the homogeneous leaching across the size classes (*see Figure 6.13*), and the RTD distribution contribution where the model curves emulated the extraction curve offsets and captured the step-wise release observed in the leaching curves.

The rapid increase in the measured data followed by a flat tail almost suggests that the flow is not homogeneously distributed, favouring contact with the rapid leaching fines over the earlier periods, with slower-leaching phases being associated with the tail, perceivably from coarser particles. This would be a very interesting finding and very counter-intuitive, but one that would require much more systematic investigation to clarify cognizant of the complex silver dissolution system as revealed.

Alluding to the hypothesis of this study, it cannot be said with certainty that the combined RTD leach model approach was successful or unsuccessful; nonetheless, it is a promising approach to better characterize the behaviour of the packed bed using a combination of leaching extraction with the fluid flow. This concept can be further improved by obtaining measured kinetics of the smaller size fractions and

investigating the effect of mixing the tracer and leaching lixiviant for the leaching kinetics of the model. The data should be modelled using available batch-test extraction data and calculate it at the weighted order of reaction on the assumption of the size blend; i.e. any selected BDC. The RTD of the system would then be used to translate the leaching extraction and interpret the flow behaviour. However, this goes beyond the scope of the present project.

7 CONCLUSION

The extraction beneficiation of low-grade ore resources from coarse particle fraction has proven to be successful using heap leaching technology. As the literature review has indicated, the technique is challenged by low mineral conversion and long extraction periods. Through RTD investigations several factors have been proposed to be responsible. Using column reactors to mimic heap leaching on a laboratory scale, literature has indicated that flow distribution in packed bed does show both plug flow type and CSTR flow type behaviour; however, a closer investigation of such varying flow types remains outstanding. Thus, the aim of this research was to establish an understanding of packed bed reactor flow type behaviour with the use of conventional tracer studies and reactive column leaching using a fully characterized ore.

A synthetic silver ore was produced with the aim of possessing specific ideal properties for the leaching test work. Conventional tracer experiments were carried out to interpret the leaching distribution. Visualization and leaching characterization studies were precursors that provided information for validating the synthetic ore ideal properties and understanding the inherent dissolution performance of the ore for the RTD studies. Micro-XCT and QEMSCAN were techniques used for characterizing the ore ideal properties. Uniform grain size distribution, grain dispersion throughout the particle-matrix, homogeneous porosity, and even grade distribution in the different size fractions were the specific physical characteristics required of the synthetic ore. Particle size distribution (PSD) and flowrate were the two RTD parameters investigated in the packed beds investigated.

7.1 Characterization Studies

Micro-focus X-ray computed tomography was performed on four selected crushed size fractions (-19/+16, -16/+11.2, -8/+5.6, and -4/+2.8 mm) to characterize the synthetic ore; while bulk mineralogy, grain properties, and overall grade distribution were validated with QEMSCAN.

Key findings from the visualization studies indicated the following:

a. The synthetic ore was homogenously porous but the porosity was not continuous to facilitate the dissolution of mineral grains through cracks/ fissures. XCT showed no visible or quantifyable fractures, while water adsorption measurements (WAM) indicated the available cavities were sub-micron fissures not identifiable on XCT. This non-continuous micro-porosity is believed to have been one reason responsible for poor/slow extraction from the coarse particles in both the leaching characterization and reactive leaching investigations, suggesting that a crack network was not well established. Unlike in leaching systems where the gangues react with the lixiviant resulting

in growth of voids in the internal crack network of the particle, gangues of the synthetic silver material was inert to the cyanide leaching system to have developed pores via gangues dissolution.

b. Grains were observed to have been finely disseminated throughout each selected particle.
c. Mineral grade distribution in each investigated particle was uniform based on digestion assay, but XCT indicated that the grade of silver decreased with the increasing size class. This trend in the analysis was shown, by QEMSCAN analysis, to have been influenced by the presence of impure mineral phases that affected the quantification of silver grains during the XCT defects analysis of larger particles. Overall grade analysis was 0.058 wt%, 0.056 wt%, and 0.051 wt% for the theoretical grade, micro-XCT, and digestion head grade assay, respectively.
d. Quantitative analysis of XCT and QEMSCAN at 4.8 and 4 μm resolutions revealed that the grain size distribution throughout the particle-matrix was about ~21-microns. The ultimate quantity was based on the 3D technique due to the reason that the 2D might be biased through the insufficient number of grains analysed.

Pure silver metal leaching and coarse synthetic particle leaching were two approaches that the leaching characterization consisted of. The coarse particle leaching was further categorized into shake flask experiments and circulating fluidized fixed bed leaching experiments. All the crushed particle fractions were characterized in the shake flask test work with varying reagent concentrations and temperatures, while selected size fractions were leached with the circulating fixed bed test work at room temperature in 275 ppm NaCN, pH10.5~10.8 solution.

The pure silver leaching studies indicated a rate of dissolution 1~3 orders of magnitude lower than literature values, whereas the reaction order (which was near-zero order) and activation energies corresponded to values found in literature. The rate of silver leaching was accepted to be slow because of molecular diffusion but its exact mechanism remains unclear. It was postulated that surface effects influenced the rate of dissolving the ultrafine silver powder. In the literature where ultrafine grains of silver were investigated, the results were similar to this present study, whereas much faster rates were observed for silver plated surfaces

The coarse particle leaching from the shake flask experiments was very limited and inconclusive. The experiments were perceived to have been challenged largely by lower soluble oxygen ingress to aid the dissolution at reaction sites in the batch experiment. Furthermore, particle diffusion was also recognized to slow the dissolution of minerals from the coarse material. Both pure silver leaching and coarse particle shake flask experiments showed that the silver dissolution dropped when the temperature was increased. .

Coarse particle leaching performed with the circulating fluid bed reactor showed better extraction than the shake flask experiments but was still low (~20 % after ~17 days). The better leaching performance of these selected particles was attributed to the mode of reactor operation, continuous flow; where fresh NaCN

solution containing dissolved oxygen was continuously fed to the reactor. The shrinking core and extended topology models were utilized with the extraction data to predict the leaching mechanism. This revealed that the controlling mechanism of extraction was governed by a combined effect of diffusion-reaction at the surface and near-surface regions, but not in the core of the coarse particles. That is plausible, given the limited pore network throughout the particle found in the XCT study.

The study of tracking the dissolution progression of leaching into the coarse particle, by stopping the reactor from time to time for XCT scans, was not successful due to the low scanning resolution (20 μm), low rate of silver dissolution, and the insufficient leaching progress over the relatively short duration of the experiment to determine the disappearance or size reduction of silver grains.

7.2 RTD Studies

Determination of the flow behaviour of the packed bed using a laboratory column reactor was investigated, applying conventional tracer RTD and reaction leaching approaches to the same column beds in immediate succession. The parameters of particle size distribution, utilizing different artificial blends along with the true blending distribution coefficient of the crushed synthetic ore and varying reagent flowrate were carried out in different sets of experiments.

Conventional RTD studies indicated that residence time distribution of the lixiviant depended on the weight composition of fines present in the packed bed. It was revealed that the PSD along 0.5, 0.721, and 1.0 blending distribution coefficient (BDC) exhibited a narrow distribution with a marginal difference of time spent in the reactor. The residence time at 0.25 BDC column was slightly longer, evident by the fact that the column effluent did not attain the maximum concentration of the tracer. This suggests that the residence time of tracer meandering through the packed bed is largely dependent on the size distribution of the blend, especially the weight composition of fines in the packed bed. On the other hand, flowrate RTD studies were performed varying the rates at 12, 6, and 3 $L/m^2/h$. The studies revealed that the distribution of residence time showed no significant difference across the varying flowrates.

Reactive leaching studies on the silver extraction performance from the column were conducted and related to the performance observed from the nonreactive tracer. This work revealed that surface reaction dissolution appeared rapidly over two days of leaching, followed by a dramatic drop in the extraction. This trend was observed across all the PSDs, which suggested that dissolution extraction after the drop was controlled by particle diffusion of lixiviant and leached silver in and out of the subsurface of the particles. Unlike the conventional tracer studies, the leaching investigation revealed that silver extraction was

independent of the packed bed blending coefficients beyond the point of mineral leaching from the particle surface.
The 0.25 BDC extraction followed a similar trend to the 0.721 and 1.0 BDC, which was not anticipated. This trend was attributed to the fines in the 0.25 BDC bed attaining significant compaction during the bed preparation that rendered the multitude of individual small particles to behave like single larger particles with inherently longer pores.

The effect of varying the flow rate on column leaching extraction demonstrated no trend consistent with the increasing irrigation rate. The lowest flowrate resulted in the poorest extraction. Comparison of the recovery performance of all reactors (i.e. varying PSD and flow rate) revealed that leaching at 0.25 BDC and 3 $L/m^2/h$, respectively, were potentially the result of a switch to kinetic and reagent supply control, whereas the overall leaching in all the other experiments was limited by particle and molecular diffusion.

The flow type behaviour of the column experiments was assessed with both the nonreactive tracer result – the conventional approach – and the reactive column leaching approach. RTD tracer data of both step-up and step-down experiments were compared to simple CSTR and Plug flow models to evaluate the flow distribution.

The step-up stage showed curves that were similar to a CSTR, whereas the step-down tracer data exhibited flow that resembled a characteristic plug flow performance. The characteristic long tail of the step-down data was clearly indicative of the exchange of phases between the immobile and mobile flow regimes in the particle interstices, while the rapid increase of the concentration gradient in the effluent for the step-up stage suggest fast moving mobile flow with very little particle-reagent interaction as the solution permeated through the reactor.

In an attempt to use the RTD data to predict the column leaching, each column was assumed to have been characterized by a number of plug channels that each performed as a set of multiple CSTRs in series. Each of these was modelled using the extended *k-phi* extend topology model for each size class, weighting these relative to the particle blend and then coupling these with the RTD data to simulate the distributed flow extraction.

The comparison of the model result to the extraction data was relatively poor. The measured data demonstrated a rapid increase in the dissolution followed by a slower extraction phase, which suggests that the flow is not homogeneously distributed relative to particle size classes. The leach performance indicated favoured contact regimes with rapidly leaching fines, while the slower-leaching phases emanating from the coarser particles. On the other hand, the model curves predicted homogeneous extraction for all channel paths, suggesting almost linear leaching. The discrepancy between the model and the data was attributed to

both, the size blend associated with the different flow paths not being the same, as assumed, and the individual particle kinetics measured in the circulating fluid fixed bed reactor were not representative of the (faster) kinetics determined in the column leaching experiments, possibly relating to the fines.

The reactive column leaching experiments revealed that the successive RTD and leaching irrigation resulted in lower silver extraction compared to the simultaneous application of the tracer chemical (KNO_3) and the leaching reagent (NaCN). It was assumed that the tracer served as a better oxidizing agent in the simultaneous reagent column; however, the assumption remains unconfirmed. It is proposed that the independent reaction needs to be tested under the exact same conditions as likely experienced in the column.

This comprehensive study sought to advance the understanding of flow behaviour of packed bed reactors using both conventional RTD tracer and reactive leaching studies on a homogenised 'ore'. While the work provided supporting evidence to some extent that columns producing apparent CSTR flow behaviour may in actual fact be reflecting a distribution of different plug flow channels, this concept has not yet been fully proven through the complementary leaching study as postulated. But there are potential explanations through mechanisms that were not anticipated, which merit further investigation in future studies.

7.3 Future Work

The flow type distribution performance in heap packed bed is of growing interest. The conventional approach of determining a given reactor output performance, the non-reactive RTD tracer technique, is a valid standardized approach; but it becomes misleading in that a given distribution curve can correspond to two different reactor types. The concept proposed in this current project for elucidating the fixed column bed flow type distribution based on leaching extraction can be extended in a number ways to substantiate the concept in the following manner.

- The kinetic reaction of the smaller particle size below -4/+2.8 mm - in narrow class fractions for accuracy it will be very pertinent in providing details of possible extraction in the column blend for the model prediction, which could be extended to the source term of more complicated hydraulic models. The leaching characterization tests for all size fractions is recommended to be performed in well agitated reactors.

- It is recommended to utilize a different mineral dissolution system that should have inherently simpler chemistry selective to the targeted mineral with respect to the reagent attack and would be cheaper.

For instance, Ammonia (NH_3) leaching of copper particles embedded in concrete matrix analogous to this study might merit investigation.

- The continuous porous network structure of the ore matrix becomes cardinal to the dissolution of targeted minerals from the inner particle core and subsurface regions. It is recommended to investigate different crushing methods to enhance physical cracking of the artificial ore particles, or alternative preparation methods that will promote the development of internal cracks/fractures to the material.

- Prior to embarking on the column investigation utilizing a blended distribution of particles for RTD and leaching extraction, preliminary column tests with single particle sizes are recommended. Such column extraction results can be compared to the leaching kinetics results to predict the blended column PSD extraction performance to determine the flow behavior.

- Investigating the influence of bed height on the flow distribution is recommended. It is perceived that taller beds would exhibit delays, producing RTD curves resembling a plug flow and shorter beds attain a rapid breakthrough to produce curves more-like a characteristic CSTR flow type distribtution.

- Finally, it is recommended that both RTD and column leaching investigation to elucidate flow performance be extended to conducting column packed bed visualization studies using positron emission tomography (PET) scanning technique. This approach has the advantage of providing information on both the flow distribution and the path of the distribution.

REFERENCES

Bartlett, R. (2013). Solution Mining 2e. Routledge.

Bartlett, R. W. (1998). Solution mining: Leaching and fluid recovery of materials. Psychology Press.

Bam, L.C., Miller, J.A. and Becker, M., (2020). A Mineral X-ray Linear Attenuation Coefficient Tool (MXLAC) to Assess Mineralogical Differentiation for X-ray Computed Tomography Scanning. Minerals, 10(5), 441.

Becker, M., Wightman, E. M., & Evans, C. L., ed.(2016). Process Mineralogy. Brisbane, Australia: Julius Kruttschnitt Mineral Research Centre.

Bouffard, S. C., & Dixon, D. G. (2001). Investigative study into the hydrodynamics of heap leaching processes. Metallurgical and Materials Transactions B, 32(5), 763-776

Bouffard, S. C., & Dixon, D. G. (2002). On the rate-limiting steps of pyritic refractory gold ore heap leaching: results from small and large column tests. Minerals Engineering, 15(11), 859-870.

Bouffard, S. C., & Dixon, D. G. (2007). Evaluation of kinetic and diffusion phenomena in cyanide leaching of crushed and run-of-mine gold ores. Hydrometallurgy, 86(1-2), 63-71.

Bouffard, S. C., & West-Sells, P. G. (2009). Hydrodynamic behavior of heap leach piles: Influence of testing scale and material properties. Hydrometallurgy, 98(1-2), 136-142.

Bouffard, S., (2003). Understanding the heap biooxidation of sulfidic refractory gold ores. PhD Thesis, University of British Columbia.

Cariaga, E., Martínez, R. & Sepúlveda, M., (2015). Estimation of hydraulic parameters under unsaturated flow conditions in heap leaching. Mathematics and computers in simulation, 109, 20-31.

Cherkaev, A., (2019). The art of soaking rocks: systematic study of liquid and solute flow in packed rock beds in the context of heap leaching. Ph.D. Thesis, University of Cape Town.

de Andrade Lima, L. R. P. (2006). Liquid axial dispersion and holdup in column leaching. Minerals Engineering, 19(1), 37-47.

Deitz, G.A. and Halpern, J., 1953. Reaction of silver with aqueous solutions of cyanide and oxygen. JOM, 5(9), 1109-1116.

Dhawan, N., Safarzadeh, M. S., Miller, J. D., Moats, M. S., & Rajamani, R. K. (2013). Crushed ore agglomeration and its control for heap leach operations. Minerals Engineering, 41, 53-70.

Dixon, D. G., & Hendrix, J. L. (1993). A mathematical model for heap leaching of one or more solid reactants from porous ore pellets. Metallurgical Transactions B, 24(6), 1087-1102.

Esmkhani, R., Ghobadi, B., Amirkhani, A., & Rezadust, S. (2013). The effect of increasing capacity on gold recovery and optimization of cyanidation parameters in Aghdarreh gold ore plant. Australian Journal of Basic and Applied Sciences, 2(7), 702-708.

Ferrier, R. J., Cai, L., Lin, Q., Gorman, G. J., & Neethling, S. J. (2016). Models for apparent reaction kinetics in heap leaching: A new semi-empirical approach and its comparison to shrinking core and other particle-scale models. Hydrometallurgy, 166, 22-33.

Free, M. L. (2013). Hydrometallurgy: fundamentals and applications. John Wiley & Sons.

Gani, R. & Manzila, A., (2018). Characterisation of Silver Leaching from Artificial Ore. Honours Thesis, University of Cape Town.

Ghorbani, Y., Becker, M., Mainza, A., Franzidis, J. P., & Petersen, J. (2011). Large particle effects in chemical/biochemical heap leach processes–a review. Minerals Engineering, 24(11), 1172-1184.

Ghorbani, Y., Petersen, J., Becker, M., Mainza, A.N. & Franzidis, J.P., (2013). Investigation and modelling of the progression of zinc leaching from large sphalerite ore particles. Hydrometallurgy, 131, 8-23.

Ghorbani, Y., Franzidis, J. P., & Petersen, J. (2016). Heap leaching technology—current state, innovations, and future directions: a review. Mineral Processing and Extractive Metallurgy Review, 37(2), 73-119.

Ghorbani, Y. (2012). On the progression of leaching from large particles in heaps. Ph.D. Thesis, University of Cape Town.

Govender, E., Bryan, C.G., & Harrison, S.T.L., (2015b). A novel experimental system for the study of microbial ecology and mineral leaching within a simulated agglomerate scale heap bioleaching system. Biochem. Eng. J. 95, 86–97

Govender-Opitz, E., Kotsiopoulos, A., Fagan-Endres, M., & Harrison, S. T. (2017). Insight into solute and microbial transport in heap (bio) leaching systems using residence time distribution. Hydrometallurgy, 168, 1-6.

Habashi, F., (1967). Kinetics and mechanism of gold and silver dissolution in cyanide solution. Butte, MT: Montana College of Mineral Science and Technology.

Hlabangana, N., Bhebhe, S., Mguni, N.G., Danha, G. and Tshuma, J., (2018). Optimisation of the leaching Parameters of a gold ore in sodium cyanide solution. International Journal of Engineering Research and Reviews, ISSN 2348-697X (Online) 6(1), 1-10.

Ilankoon, I. M. S. K., Cole, K. E., & Neethling, S. J. (2013). Measuring hydrodynamic dispersion coefficients in unsaturated packed beds: Comparison of PEPT with conventional tracer tests. Chemical Engineering Science, 89, 152-157.

Julian, H.F., Smart, E. & Allen, A.W., 1921. Cyaniding gold and silver ores. London.: Griffin.

Kartha, S. A., & Srivastava, R. (2012). Slow and fast transport in heap leaching of precious metals. Transport in porous media, 94(3), 707-727.

Kasaini, H., Kasongo, K., Naude, N., & Katabua, J. (2008). Enhanced leachability of gold and silver in cyanide media: Effect of alkaline pre-treatment of jarosite minerals. Minerals Engineering, 21(15), 1075-1082.

Levenspiel, O., (1999). Chemical Reaction Engineering. 3rd ed. New York: John Wiley & Sons.

Li, J., Zhong, T.K. & Wadsworth, M.E., (1992). Application of mixed potential theory in hydrometallurgy. Hydrometallurgy, 29(1-3), 47-60.

Li, J. & Wadsworth, M.E., (1993). Electrochemical study of silver dissolution in cyanide solutions. Journal of the Electrochemical Society, 140(7), 1921-1927.

Manning , T. & Kappes, D., 2016. Heap Leaching of Gold and Silver Ores. In: Unit Operations, Part II. USA: Elsevier B.V, 413-428.

Marsden, J., & House, I. (2006). The chemistry of gold extraction. SME.

McBride, D., Croft, T. N., Cross, M., Bennett, C., & Gebhardt, J. E. (2014). Optimization of a CFD–Heap leach model and sensitivity analysis of process operation. Minerals Engineering, 63, 57-64.

McBride, D., Cross, M., & Gebhardt, J. E. (2012). Heap leach modeling employing CFD technology: A 'process' heap model. Minerals Engineering, 33, 72-79.

McBride, D., Gebhardt, J. E., & Cross, M. (2012). A comprehensive gold oxide heap leach model: Development and validation. Hydrometallurgy, 113, 98-108.

Morrison, R. D. & Gu, Y., (2016) "X-ray Computed Microtomography." in Becker, M., Wightman, E.M. and Evans, C.L., 2016. Process mineralogy. 133-147.

Negron, L., Pingitore, N., & Gorski, D. (2016). Porosity and Permeability of Round Top Mountain Rhyolite (Texas, USA) Favor Coarse Crush Size for Rare Earth Element Heap Leach. Minerals, 6(1), 16.

Nicol, B.S. & Mbatha, B.S., (1998). The kinetics of the dissolution of colloidal silver in cyanide medium and applicatioin to the control of the cyanidation process. Journal of the Southern African Institute of Mining and Metallurgy, 98(1), 19-22.

Nwaila, G. (2014). Application of HPGR and X-Ray CT to investigate the potential of Witwatersrand gold ore for heap leaching: A process mineralogy approach. MSc, University of Cape Town.

Peng, S. (2009). Characterization of solute transport parameters in leach ore: inverse modeling based on column experiments. Frontiers of Earth Science in China, 3(2), 208-213.

Petersen, J. & Petrie, J.G., (2000). Modellling and assessment of the long-term leachate generation potential in deposits of ferr-chromium slags. Journal of the Southern African Institute of Mining and Metallurgy, 100(6), 355-364.

Petersen, J., & Dixon, D. G. (2007). Modeling and optimization of heap bioleach processes. In Biomining (pp. 153-176). Springer, Berlin, Heidelberg.

Petersen, J. (2016). Heap leaching as a key technology for recovery of values from low-grade ores–A brief overview. Hydrometallurgy, 165, 206-212.

Ram, R., Beiza, L., Becker, M., Pownceby, M.I., Chen, M., Yang, Y., Yang, S. & Petersen, J., (2020). Study of the leaching and pore evolution in large particles of a sulfide ore. Hydrometallurgy, https://doi.org/10.1016/j.hydromet.2020.105261. p.105261.

Robertson, S. (2017). Development of an integrated heap leach solution flow and mineral leaching model. Hydrometallurgy, 169, 79-88.

Sanchez-Chacon, A. E., & Lapidus, G. T. (1997). Model for heap leaching of gold ores by cyanidation. Hydrometallurgy, 44(1-2), 1-20.

Science Lab, 2013. Material Safety Data Sheet for Sodium Cyanide , Texas : Science Lab.

Senanayake, G., (2006). The cyanidation of silver metal: Review of kinetics and reaction mechanism. Hydrometallurgy, 81(2), 75-85.

Teja Ruiz, A., Juárez Tapia, J., Reyes Domínguez, I., Hernández Cruz, L., Pérez, M., Patiño Cardona, F. & Flores Guerrero, M., 2017. Kinetic Study of Ag Leaching from Arsenic Sulfosalts in the S2O32−-O2-NaOH System. Metals, 7(10), .411.

Wang, X. and Forssberg, K.E., 1990. The chemistry of cyanide-metal complexes in relation to hydrometallurgical processes of precious metals. Mineral Procesing and Extractive Metallurgy Review, 6(1-4), 81-125.

Wilkomirsky, I., Rojas, N. & Balladares, E., (2010). Gold and Silver Cyanidation from a Residue Produced by Leaching Dead-Roasted Copper White Metal. Canadian Metallurgical Quarterly, 49(1), 29-37.

Yang, Y., Yang, Y., Gao, X., Petersen, J. & Chen, M., (2019). Microstructure evolution of low-grade chalcopyrite ores in chloride leaching-A synchrotron-based X-ray CT approach combined with a data-constrained modelling (DCM). Hydrometallurgy, 188, 1-13.

Yin, S. H., Wang, L. M., Chen, X., & Wu, A. X. (2016). Effect of ore size and heap porosity on capillary process inside leaching heap. Trans. Nonferr. Met. Soc. China, 26, 835-841.

APPENDICES

Appendix I

Safety, Health and Environmental

Safety requirements were the main concerns during the period of this study. One of the widely used forms of cyanide for leaching is sodium cyanide (NaCN). The use of cyanide as lixiviant pose potential hazards. The material safety data sheet (MSDS) of NaCN (*Science Lab, 2013*) reveals that it is a strong irritant when in contact by inhalation, ingestion, skin absorption and eye. In the case of eye contact, it causes corneal damage or blindness. On the skin, it causes inflammation and blistering. Irritation of the respiratory and gastrointestinal tract can occur as a result of dust inhalation or when hydrogen gas is formed at acidic pH range. Long exposure can cause permanent lung damage, unconsciousness or even death. Cyanide also causes death in seconds if ingested or inhaled at a higher dosage. A few hours to a day is a required space of time for treatment if come in contact at a lower dosage. Exposure limit of sodium cyanide is 5 mg/m^3.

Safe working measures associated with the handling of cyanide included the use of personal protective equipment (PPE) worn at all times. Required PPE includes; lab coat, safety goggles, gloves, dust respirator, long pants and closed shoes. Furthermore, as an engineering control, an exhaust ventilation system was incorporated to maintain airborne concentrations below the exposure limit of 5 mg/m^3. Such engineering controls are available in the dedicated cyanide lab in the chemical engineering department, UCT and was also provided at Necsa where the CF-FBR leaching experiments were carried out. As well as standard management of poisonous solid/liquid waste. Moreover, clear labelling of solutions/samples and signage were mandatory and followed.

First aid measures related to contact with the cyanide include:

- flushing the eyes or washing up with water for 15 minutes if contacted, removing contaminated clothes in the event of skin contact or accidental spills
- washing with disinfectant, applying antibacterial cream and seeking medical attention
- moving to an area with fresh air or using artificial respiration with regards to inhalation and inducing vomiting with regard to indigestion.

Furthermore, the knowledge on the use and administration of the laboratory cyanide antidote kit was conducted prior to experiments. An up to date cyanide antidote kit was kept in the laboratory at all times.

Storage of the reagent is of importance when handling. Cyanide is stored in a dry, tightly closed container in a ventilated area away from any source of heat or ignition. The container containing cyanide is stored in

an exclusively lockable poison cupboard away from other reagents. Mixing with acids can result in the formation of hydrogen cyanide that is flammable and highly toxic when ingested.

Handling and Disposal of Cyanide Contaminated Waste

Cyanides must be detoxified before being disposed of to ensure that it is harmless. All glassware that was in contact with cyanides were rinsed with an alkali solution of pH 10, this is done to oxidize cyanide to the non-toxic form cyanate. Following the initial rinse, all glassware were rinsed with ferrous sulphate to precipitate the cyanide. It is important to ensure the pH does not drop to below 10 as this can result in the formation of cyanogen chloride and hydrogen cyanide gas. The rinse solution was disposed of as hazardous waste along with all other liquid cyanide waste into containers safe kept isolated from all other waste streams and clearly labelled as "Cyanide waste – no acids" in the fume. All confiscated waste were collected for finally disposal by the analytical lab, UCT.

Liquid Waste

Liquid waste was treated with 3 g/l ferrous sulphate. The ferrous sulphate treatment precipitated the cyanide from the solution and the precipitation is indicated by a blueish colour change. The precipitation formed a ferrocyanide complex in solution, via the equation (Adams, 1992):

$$\boldsymbol{Fe^{2+} + 6CN^{-} \rightarrow Fe(CN)_6^{4-}}$$

According to the university's hazardous waste procedures, liquid cyanide waste is placed into 25 litre drums, collected by the analytical lab, and sent to Averda Waste Management Solutions.

Solid Waste

Solid waste was collected and sealed in clearly marked disposal bags, which are sent to the university's hazardous waste incineration. Hazardous waste incineration facilities generally operate above 1100 °C and have highly specialised flue gas cleaning systems.

Appendix II

Table A.1: Measured weight PSD for the blending distribution coefficient according to the GGS model for the 3 kg column capacity.

BDC	**0.25**	**0.5**	**0.721**	**1.0**
Size Fraction (mm)	wt (g)	wt (g)	wt (g)	wt (g)
+19	0	0	0	0
-19/+16	126.16	247.01	349.61	473.68
-16/+11.2	245.16	449.67	601.00	757.89
-11.2/+8	212.07	356.66	441.46	505.26
-8/+5.6	206.16	317.97	364.61	378.95
-5.6/+4	178.33	252.20	267.83	252.63
-4/+2.8	173.36	224.84	221.20	189.47
-2.8/+2	149.96	178.33	162.48	126.32
-2/+1	271.88	285.08	232.77	157.89
-1	1436.92	688.25	359.04	157.89

BDC	0.25	0.50	0.721	1.0
d_{80} (mm)	7.81	12.23	13.76	15.20

Appendix III

A.

Pore volume void sphericity of the synthetic silver ore characterized on selected class fractions.

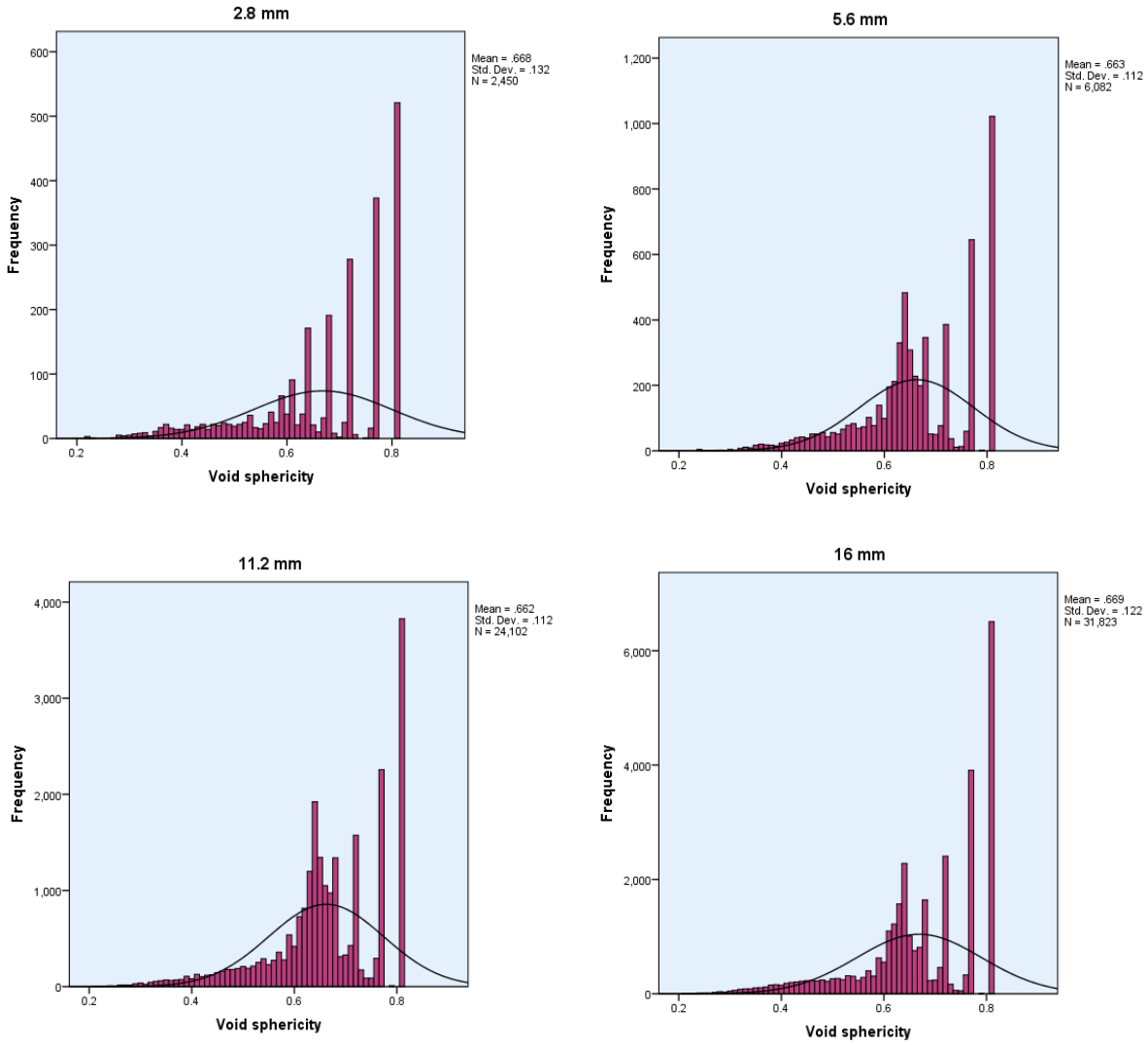

B. 3D Pore volume map progression illustrating non-continuous porosity

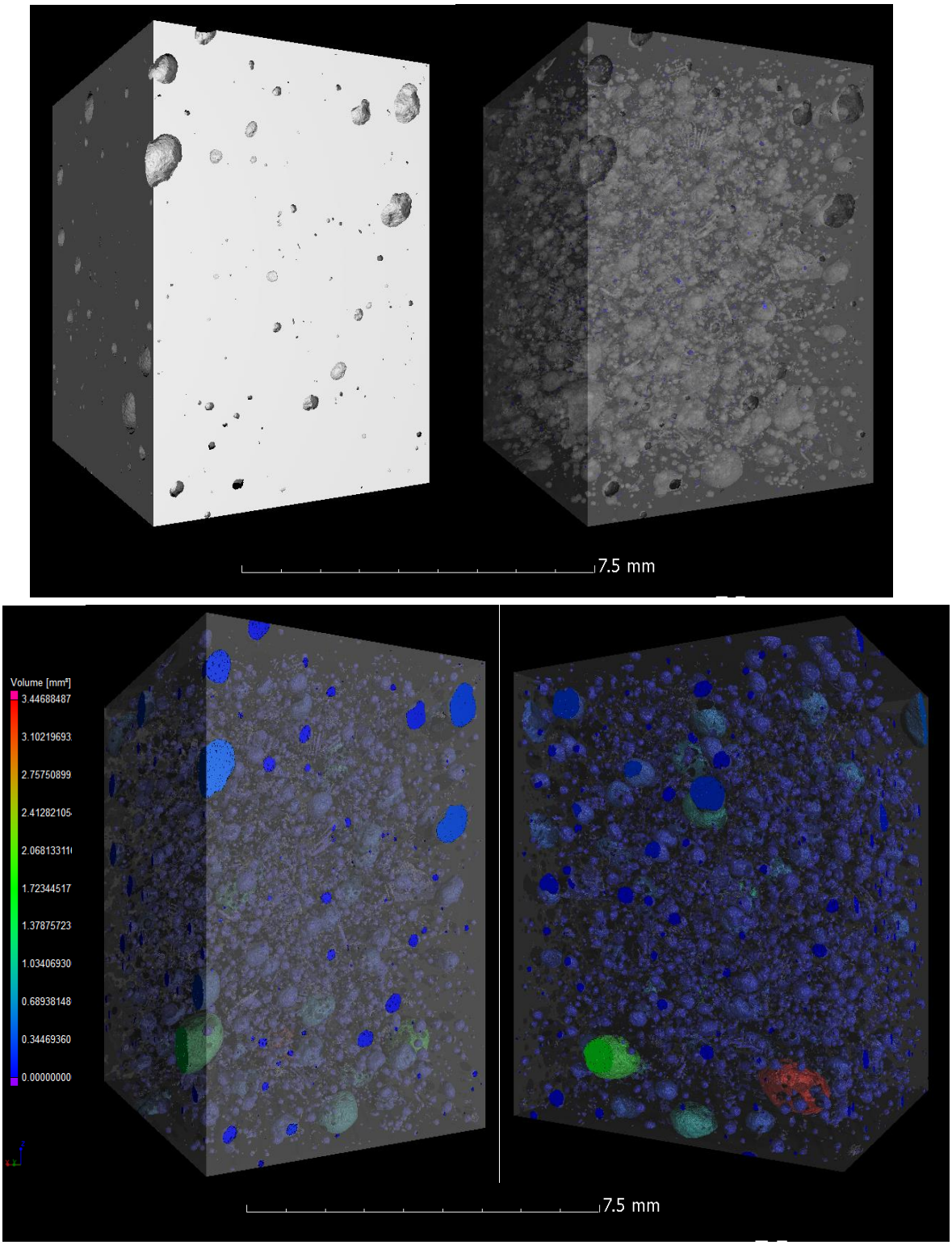

C. 3D Grain dispersion diagram visualizing fewer grains from the particle surface to many grains in the internal particle matrix.

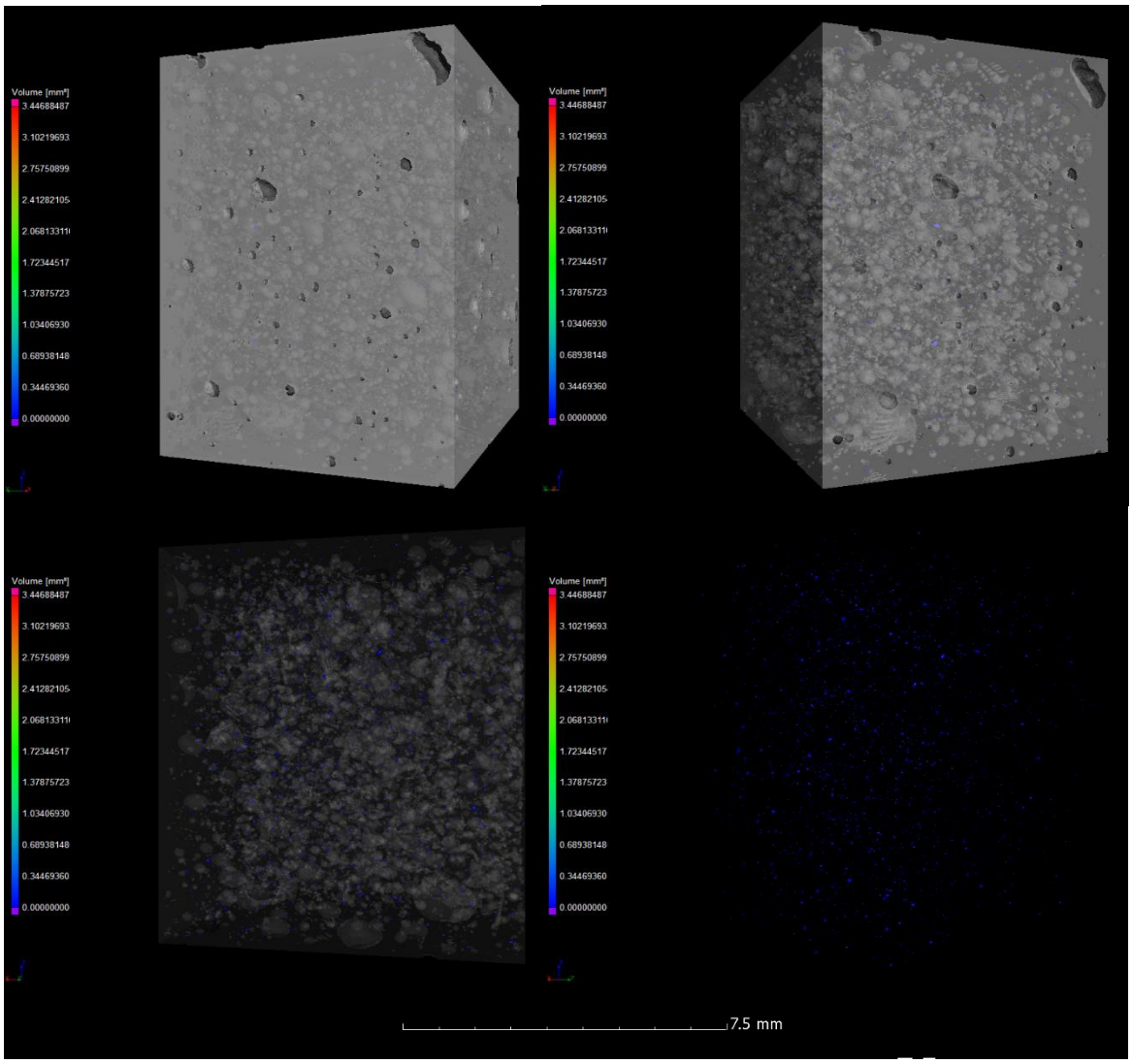

Appendix IV

QEMSCAN image of the synthetic silver ore showing the bulk mineralogy.

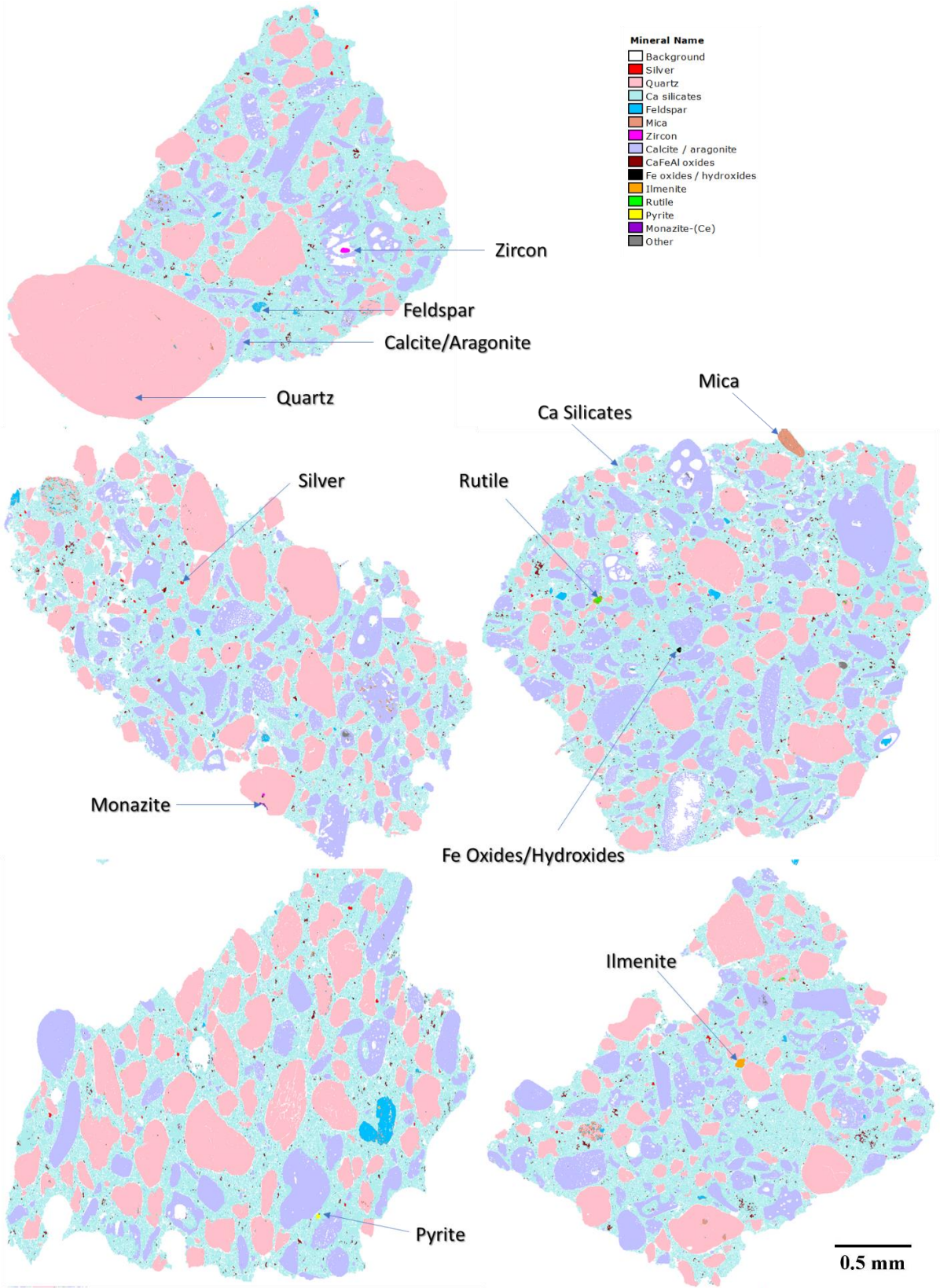

Appendix V

A. Pure leaching extraction data.

Pure Silver Leaching Extraction Data
Pure Silver 200 mg ; Lixiviant Solution 200 ml

Extraction (%)				
NaCN Conc (ppm)	Time (hrs)	25°C	48°C	60°C
50 ppm	0	0	0	0
	0.083	0.980	1.520	0.340
	0.333	1.284	3.021	0.758
	0.833	3.516	5.181	1.901
	1.333	3.567	5.266	2.513
	2.083	4.479	6.226	3.121
	3.083	4.899	6.526	3.586
	5.083	5.193	6.666	4.706
	8.083	5.427	6.536	4.856
	14.083	5.463	11.516	4.802
	23.083	5.837	11.681	4.912
	35.083	6.297	13.931	4.907
	59.083	7.620	14.226	5.307
275 ppm	0	0	0	0
	0.083	0.840	2.000	1.970
	0.333	1.325	3.710	1.790
	0.833	2.990	8.480	2.285
	1.333	4.690	15.025	3.398
	2.083	8.930	21.985	4.270
	3.083	12.980	25.360	6.288
	5.083	22.010	27.110	9.277
	8.083	22.270	31.010	14.561
	14.083	25.930	38.690	19.751
	23.083	23.235	43.255	24.041
	35.083	26.535	43.255	24.736
	59.083	32.385	50.365	26.559
500 ppm	0	0	0	0
	0.083	0.480	1.690	4.600
	0.333	1.297	3.695	2.339
	0.833	2.431	8.015	3.932
	1.333	5.151	11.925	5.573
	2.083	9.471	20.725	7.461
	3.083	15.246	28.975	9.291
	5.083	29.176	35.905	13.575

	8.083	38.341	42.795	21.167
	14.083	39.541	50.715	31.313
	23.083	41.246	54.290	34.937
	35.083	42.346	57.590	40.567
	59.083	52.201	60.065	39.217

Pure Silver Leaching Follow-up Investigation Extraction Data
Pure Silver 200 mg ; Lixiviant Solution 200 ml

Extraction (%)				
NaCN Conc (ppm)	Time (hrs)	25°C	48°C	60°C
50 ppm	0	0	0	0
	0.333	3.746	5.125	5.161
	0.833	5.230	5.696	5.626
	2.083	5.373	5.823	5.517
	5.083	5.441	5.846	5.463
	8.083	5.320	5.851	5.610
275 ppm	0	0	0	0
	0.333	4.434	6.992	7.968
	0.833	8.336	11.785	11.968
	2.083	29.219	23.263	20.961
	5.083	27.056	28.320	27.550
	8.083	28.318	31.426	28.842
500 ppm	0	0	0	0
	0.333	3.407	5.122	6.355
	0.833	6.214	8.988	10.111
	2.083	12.449	16.968	20.075
	5.083	26.600	33.815	35.748
	8.083	41.296	46.707	46.689

B. Leaching extraction of vary NaCN and temperature conditions (1 mm class was not leached at 60 °C)

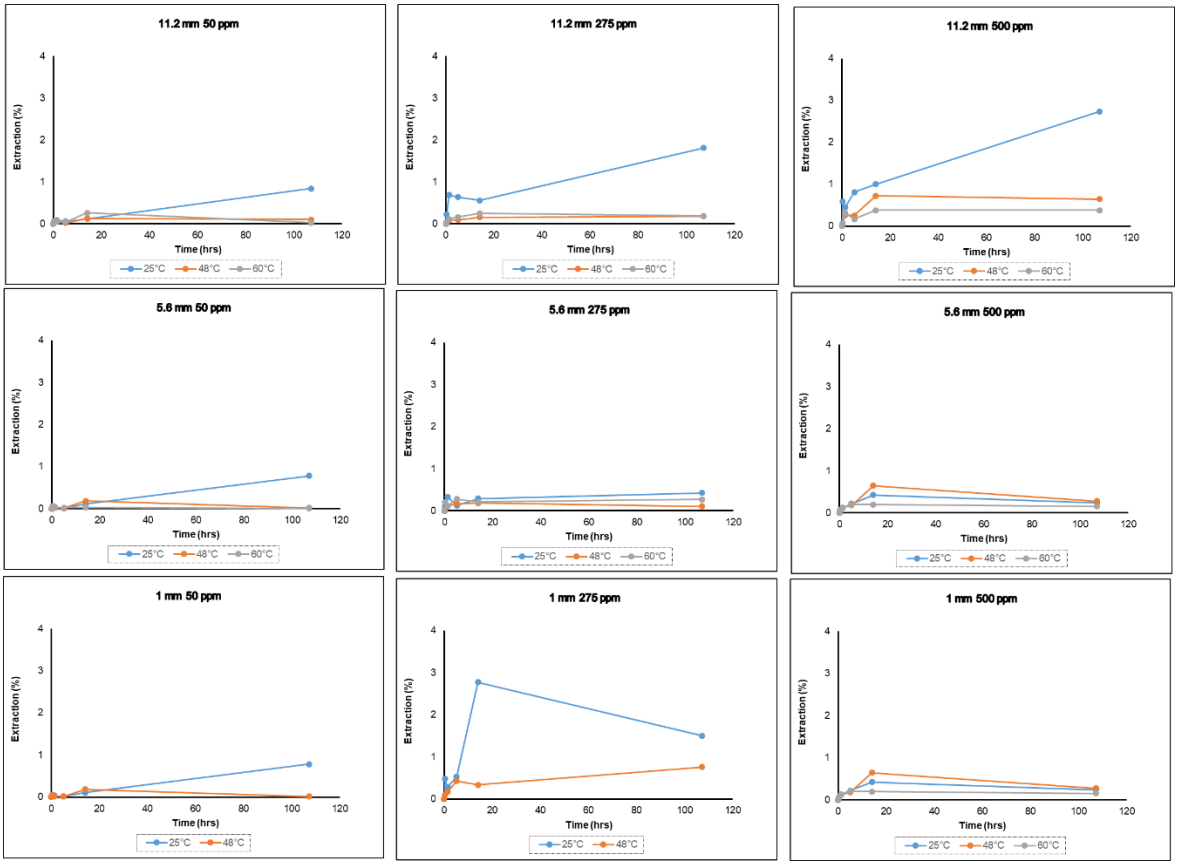

C. Data for shake flask leaching experiments

Shake Flask Extraction Data
25°C & 275 ppm NaCN

Particle Size (mm)	-19/+16	-16/+11.2	-11.2/+8	-8/+5.6	-5.6/+4	-4/+2.8	-2.8/+2	-2/+1	-1
Time (hrs)	Extraction (%)								
0	0	0	0	0	0	0	0	0	0
0.333	0.096	0.216	0.306	0.104	0.190	0.148	0.209	0.211	0.237
1.333	0.238	0.686	0.294	0.325	0.207	0.262	0.159	0.087	0.300
5.083	0.697	0.639	0.345	0.126	0.346	0.901	0.701	0.271	0.232
14.083	0.512	0.554	0.591	0.291	0.863	0.765	1.064	0.895	0.253
107.083	1.935	1.807	2.373	0.425	1.014	3.371	0.746	0.436	0.251

48 °C				
NaCN Conc (ppm)	Time (hrs)	-16/+11.2	-8/+5.6	-2/+1
50 ppm	0	0	0	0
	0.333	0.047	0.053	0.026
	1.333	0.041	0.021	0.019
	5.083	0.019	0.014	0.009
	14.083	0.126	0.185	0.002
	107.083	0.101	0.016	0.001
275 ppm	0	0	0	0
	0.333	0.028	0.044	0.085
	1.333	0.086	0.110	0.089
	5.083	0.090	0.167	0.084
	14.083	0.157	0.185	0.051
	107.083	0.182	0.109	0.072
500 ppm	0	0	0	0
	0.333	0.053	0.041	0.099
	1.333	0.262	0.126	0.167
	5.083	0.252	0.178	0.426
	14.083	0.724	0.646	0.337
	107.083	0.640	0.276	0.756

60 °C			
NaCN Conc (ppm)	Time (hrs)	-16/+11.2	-8/+5.6
50 ppm	0	0	0
	0.333	0.064	0.054
	1.333	0.062	0.032
	5.083	0.043	0.026
	14.083	0.262	0.030
	107.083	0.025	0.004
275 ppm	0	0	0
	0.333	0.044	0.136
	1.333	0.110	0.080
	5.083	0.160	0.187
	14.083	0.248	0.147
	107.083	0.186	0.191
500 ppm	0	0	0
	0.333	0.066	0.073
	1.333	0.308	0.124
	5.083	0.166	0.199
	14.083	0.374	0.198
	107.083	0.374	0.154

D. CF-FBR extraction and model conversion data

Time (hrs)	-19/+16	-16/+11.2	-8/+5.6	-4/+2.8	-19/+16	-16/+11.2	-8/+5.6	-4/+2.8	-19/+16	-16/+11.2	-8/+5.6	-4/+2.8
	Cumulative Extracted (mg)				Conversion (X)				Extended Model Conversion (X)			
0	0	0	0	0	0	0	0	0	0	0	0	0
0.5	0.0005	4.48E-05	4.77E-05	0.002138	3.49E-06	3.12E-07	3.32E-07	1.49E-05	0.000257	0.000265	0.000287	0.000366
1.5	0.0055	0.000111	0.020362	0.052844	3.84E-05	7.74E-07	0.000142	0.000369	0.000769	0.000793	0.00086	0.001098
3.5	0.078358	0.014635	0.055091	0.339638	0.000546	0.000102	0.000384	0.002368	0.001788	0.001845	0.002003	0.002556
6.5	0.532498	0.168463	0.143115	0.677888	0.003713	0.001175	0.000998	0.004727	0.003303	0.003411	0.003707	0.004731
12.5	0.731064	0.394743	0.533351	1.702505	0.005098	0.002753	0.003719	0.011872	0.006282	0.006501	0.007082	0.009041
21.5	1.399839	1.405858	1.061728	1.991022	0.009762	0.009804	0.007404	0.013884	0.010631	0.011031	0.012061	0.015403
33.5	2.223467	2.178016	2.309542	2.728512	0.015505	0.015188	0.016106	0.019027	0.01621	0.016879	0.018548	0.0237
57.5	3.644974	3.767247	4.079509	5.42997	0.025418	0.026271	0.028448	0.037866	0.026647	0.027946	0.031014	0.039667
105.5	6.612603	6.703492	7.30344	10.28197	0.046113	0.046747	0.050931	0.071701	0.044882	0.047737	0.054022	0.069229
201.5	10.47938	11.0639	13.35303	17.72653	0.073078	0.077154	0.093117	0.123616	0.072497	0.079247	0.093128	0.119779
393.5	14.75281	16.6759	21.18618	27.39233	0.102879	0.116289	0.147742	0.19102	0.103168	0.118466	0.149161	0.193054

Appendix VI

A. Conventional Inert Tracer RTD Data

Inert Tracer RTD Data												
Time (hrs)	0.721_2 L/day	0.721_1 L/day		Time (hrs)	0.721_0.5 L/day	1.0_1 L/day	0.5_1 L/day		Time (hrs)	0.25_1 L/day		Time (hrs)	Consolidated Test
0	42.5	51.25		0	6	7.75	2.85		0	1.5		0	0
6	219.3	202.3		6	32	34	9.6		6	8.6		3	2.42
24	695	480		24	116	301	15.2		12	25.2		6	4.33
30	947.5	897.5		30	242	801	477		35	361.5		12	12.26
48	995	957.5		54	551	954	920		47	678		18	62.91
54	992	942.5		72	877	968	995		59	775		35	441
78	972	1012.5		84	996	989	1000		71	798		41	803
102	1025	1010		96	840	1004	990		95	817		60	950
126	980	1015		102	955	995	990		101	828		66	1025
144	635	812.5		120	1030	926	990		119	852		84	1113
150	311.3	430		126	920	1012	1010		125	853		90	1060
168	175.3	296.3		132	1000	998	950		131	906		108	1122
174	98.3	226.8		144	910	973	910		143	846		114	1139
194	38.8	96.3		150	671	936	760		149	496		138	1103
218	82.3	67		156	538	325	620		155	395		162	1203
242	10	41.8		168	397	218	444		167	329		186	1095
270	14.3	36.3		180	224	126	247		179	253		209	1160
288	12.8	36		192	183	74	116		197	248		233	1251
				198	163	46	70		221	208.1		257	1133
				222	106	38	44		245	141.1		281	1081
				246	76	25	28		269	101.9			
				270	59	21	17		287	87			
				288	49	16	16						

B. Column wash conductivity performance

F-curve obtained from conductivity measurements of column flooding/washing stage over a period of 10 days. The data illustrated in the figure shows the fluid emanating from long pore or stagnant zones; a diffusion related influence as the result of intermittent irrigation during the flooding.

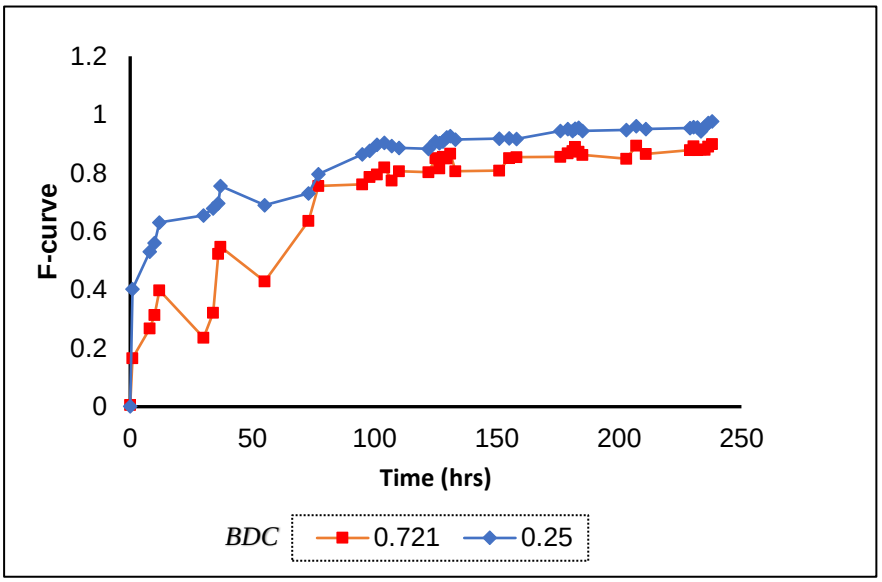

C. Reactive RTD Extraction Data

Reactive Tracer RTD Extraction Data (mg)										
Time (hrs)	0.721_2 L/day	0.721_2 L/day (repeat)	0.721_1 L/day	0.721_1 L/day (repeat)	0.721_0.5 L/day	0.721_0.5 L/day (Repeat)	0.25_1 L/day	0.5_1 L/day	1.0_1 L/day	Consolidated Test
0	0	0	0	0	0	0	0	0	0	0
3	0.186464	0.000580	0.009475	0.000388	0.00012	0.00002	0.00065158	0.0007021	0.0007914	0.000836
6	0.323194	0.002655	0.089234	0.001588	0.011088	0.000284	0.00185188	0.0458269	0.5604414	0.001461
12	1.703904	0.636630	0.329737	1.709338	0.236304	0.013566	1.20412588	0.1075819	7.2737109	3.652514
18	2.840933	1.676130	1.154023	7.337188	0.782913	0.147566	9.14183478	7.2329794	18.401011	19.78012
35	10.585598	5.769240	4.310643	28.70119	3.941109	0.2599364	32.85618	48.053559	41.953411	70.84441
41	12.204175	6.270940	4.817511	31.86829	4.528842	0.3129364	35.2128356	52.699984	44.926621	75.44927
59	22.579533	8.752490	8.198355	48.65179	6.493889	0.4806064	46.0470296	74.991484	59.646605	101.2139
65	23.874669	9.162250	8.666376	50.44045	7.075622	0.5355314	47.1956428	77.435499	61.495692	103.6845
83	34.954165	13.197050	11.52935	59.55329	11.2106	1.3139804	53.7226869	89.496359	70.894122	117.0792
89	36.805709	14.003600	12.00904	61.19809	11.45476	1.4549796	54.693672	91.331614	72.203412	119.0832
107	45.775288	18.211320	14.56537	71.18796	13.22939	2.0317796	60.112293	100.32114	79.552641	129.469
113	46.505321	18.567000	14.99161	72.38366	13.6065	2.2473046	60.9805209	101.66574	80.524191	131.2665
137	56.830723	23.102920	18.30941	73.00406	16.47835	3.9307546	67.4726849	102.7411	81.422031	143.7794
161	67.026351	30.300130	21.45244	82.90571	19.35145	5.8924346	73.2672149	111.02455	88.44263	156.0995
184	75.008832	37.128930	24.28126	92.1794	19.59909	8.2503896	78.8752931	119.38983	95.2544	157.371
208	83.229755	44.735100	27.23956	101.5829	19.77779	8.8983896	79.5639929	120.51056	96.14773	158.4375
232	84.436842	45.796440	27.56143	102.3227	20.0656	9.5909696	80.1745529	121.51553	96.96886	159.4145
256	85.384160	48.331440	27.94951	104.8627	20.41992	10.21917	80.7603989	122.48686	97.850148	159.9376
280	86.501726	49.489160	28.35155	106.2214	20.63963	10.91317	81.3816039	123.59293	98.685437	160.989

Appendix VII

gbsbor001:BorborAKKGibson_Final_Thesis_turnitin.pdf

ORIGINALITY REPORT

20%	5%	4%	19%
SIMILARITY INDEX	INTERNET SOURCES	PUBLICATIONS	STUDENT PAPERS

PRIMARY SOURCES

1	Submitted to University of Cape Town Student Paper	16%
2	open.uct.ac.za Internet Source	<1%
3	hdl.handle.net Internet Source	<1%
4	open.library.ubc.ca Internet Source	<1%
5	Submitted to University of Warwick Student Paper	<1%
6	mine.metu.edu.tr Internet Source	<1%
7	mdpi.com Internet Source	<1%
8	Submitted to University of Ulster Student Paper	<1%
9	espace.library.uq.edu.au Internet Source	<1%

Plagiarism check acknowledged. 16% similarity is from the candidate's own proposed submission - see overleaf
J. Peters 28/1/2020


https://ev.turnitin.com/app/carta/en_us/?lang=en_us&s=1&o=1117481178&u=1032346529
feedback studio
Borbor Gibson
gbsbor001:Proposal_GBSBOR001.docx
-- /0
16 of 60
Match Overview
7%
1 Submitted to University... Student Paper 4%
2 open.uct.ac.za Internet Source <1%
3 mine.metu.edu.tr Internet Source <1%
4 Ghorbani, Yousef, Jean... Publication <1%
5 core.ac.uk Internet Source <1%
6 "Extraction 2018", Sprin... Publication <1%
7 Elaine Govender-Opitz, ... Publication <1%
Residence Time Investigation of Artificial Silver Ores in Heap Leaching Using Cyanide Lixiviant
University of Cape Town • Yunivesithi yaseKapa • Universiteit van Kaapstad
By
Borbor A.K.K. Gibson
Supervisor
Professor Jochen Petersen
Page: 1 of 32
Word Count: 11020
Text-only Report
High Resolution
On
ENG
16:16
2020/01/28